e-ISSN: 2757-9077

Open Access

ENGINEERING PERSPECTIVE

CONTENTS

Research Articles — **Page Number**

Wenguang LI
A Mathematical Model for Experimental Head-Flow Rate Curve of Partial Emission Pumps 1-6

Fatima HAIDAR, Abderaouf LAIB, Syed Ali AJWAD, Guillaume GUILBERT
Integrated Vehicle Dynamics Modeling, Path Tracking, and Simulation: A MATLAB Implementation Approach 7-16

Aniekan IKPE, Imoh EKANEM
Stress-strain Deformation Analysis of Conventional Vehicle Shock Absorber Materials under In-service Multi-translated Non-proportional Loading Conditions 17-31

Mohand Ouyahia BOUSSEKSOU, Yucai LIN
Thermal Modeling of Solid Hydrogen Storage in a LaNi5 Metal Hydrid Tank 32-39

Musa SHITTU, Aniefiok LIVINUS
Techno-Economic Analysis of a Natural Gas Dehydration System: A Case Study of an "X" Processing Plant in Niger Delta 40-46

ENGINEERING PERSPECTIVE Volume: 4 Issue: 1 31 March 2024

ENGINEERING PERSPECTIVE

An International Journal

Volume: 4 Issue: 1 31 March 2024

https://sciperspective.com

e-ISSN: 2757-9077 Open Access

ENGINEERING PERSPECTIVE

An International Journal

Publishing Manager **Prof. Dr. Hamit SOLMAZ**	
Editor **Assoc. Prof. Dr. Alper CALAM**	
Subject Editors	**Dr. Lina Montuori**, Universitat Politècnica de València (UPV), Spain **Dr. Gang Li**, Mississippi State University, USA **Dr. Xing Zheng Wu**, Hebei University in Baoding, China **Dr. Mamdouh El Haj Assad**, University of Sharjah, United Arab Emirates **Dr. Anle Mu**, Xi'an University of Technology, China **Dr. Gulsen Taskin**, Gazi University, Türkiye **Dr. Anderson Chu**, Columbia University, USA **Dr. Diego Fettermann**, Federal University of Santa Catarina (UFSC), Brazil **Dr. Sivasankaran Sivanandam**, King Abdulaziz University, Kingdom of Saudi Arabia **Dr. Aniefiok Livinus**, University of Uyo, Nigeria **Dr. Murat Akin**, Gazi University, Türkiye **Dr. Seyed Mohammad Safieddin Ardebili**, Shahid Chamran University of Ahvaz, Iran **Dr. Gultekin Uzun**, Gazi University, Türkiye **Dr. Babak Keykhosro Kiani**, International Institute of Earthquake Engineering and Seismology, Iran **Dr. Mingjun Xu**, Nanyang Technological University, Singapore **Dr. Malek Hassanpour**, Osmania University, India **Dr. Seyfettin Vadi**, Gazi University, Türkiye
Editorial Board	**Dr. J. Sadhik Basha**, National University of Science & Technology (IMCO), Oman **Dr. Farzad Jaliliantabar**, Universiti Malaysia Pahang, Malaysia **Dr. Bakenaz A. Zeidan**, Tanta University, Egypt **Dr. Roohollah Zanganeh**, Iran University of Science and Technology (IUST). Iran **Dr. Praveen Kumar Dadheech**, Rajasthan Technical University Kota, India **Dr. Behrouz Khoshbakht Irdmousa**, Michigan Technological University, USA **Dr. N. Shivakumar**, Aarupadai Veedu Institute of Technology, India **Dr. Tamilselvan Pachiannan**, Jiangsu University, China **Dr. Andrei Alexandru Boroiu**, University of Pitesti, Romania **Dr. Tugba Tabanligil Calam**, Gazi University, Türkiye **Dr. Kamran Poorghasemi**, Islamic Azad University, Iran **Dr. Omar Bait**, University of Batna, Algeria **Dr. Anilkumar Shere**, Indian Institute of Technology Delhi, India **Dr. Sujit Kumar Verma**, GLA University, India **Dr. Seyfi Polat**, Hitit University, Türkiye **Dr. Freddie Inambao**, University of KwaZulu-Natal, South Africa **Dr. Ridha Ennetta**, Gabes University, Tunis **Dr. Mohammad Amini**, University of Saskatchewan, Canada
Language Editor	**Neslihan Turan**, Kocaeli University, Türkiye

Volume: 4	Issue: 1	31 March 2024
Engineering Perspective publishes **four issues** per year.		

REVIEWERS WHO CONTRIBUTED TO THIS ISSUE (VOLUME: 4 ISSUE: 1)	
Dr. Youcef Brahmi	Dr. Kamal Nouri
Dr. Faruk Emre Aysal	Dr. Imtiaz Ur Rehman
Dr. Reza Aghazadeh	Dr. Ikechukwu Bismarck Owunna
Dr. Edet Ita Okon	Dr. Noel Nyang Kibanya
Dr. Mustafa Ağgül	Dr. Alexander E. Labovsky

Correspondence Address :
Gazi University, Faculty of Technology, Department of Automotive Engineering, Teknikokullar - Ankara, TURKIYE

e-mail: engineering@sciperspective.com

Technical Editor:
Regaip Menküç
Gazi University

Layout Editors:
İrem Tanış, Gazi University
Zehra Ebrar Ağca, Gazi University

e-ISSN:2757-9077

ENGINEERING PERSPECTIVE

https://sciperspective.com/ Research Paper

A Mathematical Model for Experimental Head-Flow Rate Curve of Partial Emission Pumps

Wenguang Li*

School of Mathematics and Statistics, University of Glasgow, Glasgow, G12 8QQ, UK

ABSTRACT

The head-flow rate curve of the partial emission pump is flat and with a sudden drop-off near the maximum flow rate. Thus, it is difficult to fit the experimental head-flow rate curve of the pump by using a polynomial, which is suitable for centrifugal pumps. To tackle this problem, a new mathematical model was put forward in the inspiration of the mathematical model of the equivalent electric circuit of photovoltaic cells/modules. The physics behind the model was described by using flow rate saturation effect in partial emission pumps. The model was implemented in Excel and applied to the experimental head-flow rate data of seven partial emission pumps with different specific speeds in a range of 17-80. The model can produce high-quality curve fitting (coefficient of determination of greater than 0.9), The model is adaptive to the variable experimental head-flow rate data of partial emission pumps due to changes in impeller structure, rotational speed, number of blades and impeller diameter. Further, the model can fit the experimental head-flow rate data with drooping effect at low flow rate in partial emission pumps satisfactorily (coefficient of determination of greater than 0.94). The model potentially can be used in experimental data processing in the pump industry and pump-system modelling for partial emission pumps in future.

Keywords: Curve fitting; Flow rate; Head; Mathematical model; Partial emission pump

History
Received: 03.11.2023
Accepted: 25.02.2024

Author Contacts
**Corresponding Author*
e-mail addresses : wenguang.li@glasgow.ac.uk

How to cite this paper: Li, W., (2024). A Mathematical Model for Experimental Head-Flow Rate Curve of Partial Emission Pumps. Engineering Perspective, 4(1), 1-6. http://dx.doi.org/10.29228/eng.pers.74533

1. Introduction

Partial emission pumps, as shown in Figure 1, are special centrifugal pumps developed in the 1960s, and have found extensive applications in aerospace, chemical, petroleum-chemical industries [1, 2], offshore technology [3] and so on. The pumps have an open impeller with straight radial blades in 90° blade discharge angle (measured from the reverse direction of the impeller rotation) [4].

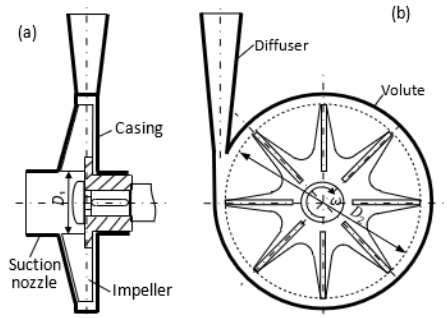

Figure 1. Impeller and volute configuration of a partial emission pump, (a) axial-cross-sectional view, (b) cross-sectional view in volute mid-span

As a result, the pumps often have a flat head-flow rate curve with dramatic sharp cut-off at the maximum flow rate in the experiment, as shown in Figure 2. Usually, a 2nd- or 3rd-order polynomial, which is mostly applicable to best fit the head-flow rate curve of centrifugal pump, is invalid for a partial emission pump. How to fit this kind of head-flow rate curve is concerned in the article.

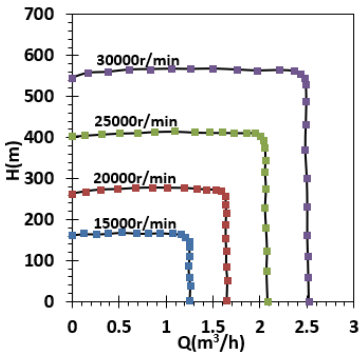

Figure 2. Experimental head-flow rate curves at the rotational speeds of 15000, 20000, 25000 and 30000r/min, the data are after [1]

2. Model and method

2.1 Current-voltage model for photovoltaic cells or modules

The author had conducted a few modelling studies on the electric circuit of flat photovoltaic (PV) cells or modules [5-8]. A flat monocrystalline PV cell or module can be presented by using a single diode equivalent circuit with five combined parameters such as photocurrent, I_{ph}, diode reversal saturation current, I_d, diode quality factor, M, combined series resistance, R_s, and shunt resistance, R_{sh} [5], as shown in Figure 3a. The performance curve, i.e. I-V curve for the PV cell can be expressed mathematically by [5]:

$$I = I_{ph} - I_d\left[exp\left\{\frac{q(V+R_sI)}{MkT}\right\} - 1\right] - \frac{V+R_sI}{R_{sh}} \quad (1)$$

where V and I are the output voltage and current of the PV cell/module, respectively; T is cell temperature, q is the electron charge, q=1.60217646×10^{-19}C, and k is the Boltzmann constant, k =1.38065031×10^{-23}J/K. I_{ph} depends on both solar radiation intensity and cell temperature in the silicon layer, while I_d is only cell-temperature dependent. A set of I-V data of a PV module was fitted by using Eq. (1), and good agreement between the data and the model is achieved, as shown in Figure 3b. This fact suggests that the exponential term in Eq. (1) can properly describe the rapid drop in the current when the voltage is beyond a certain value.

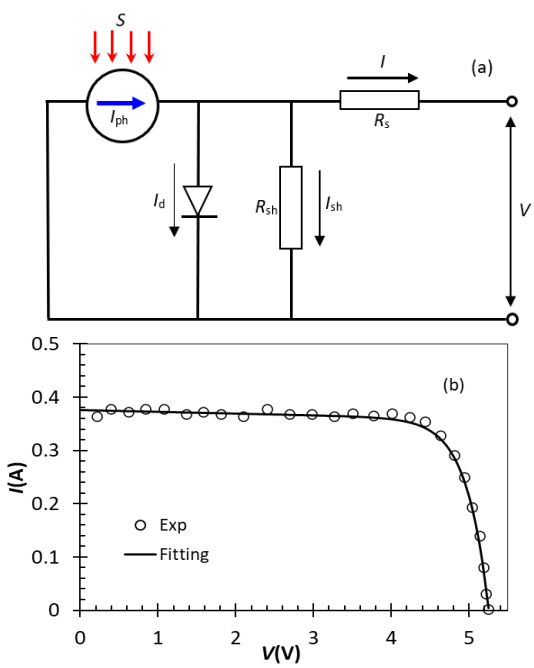

Figure 3. Single diode equivalent circuit of a flat monocrystalline PV module (a), and the experimental current-voltage (I-V) curve of the module at the standard solar radiation intensity S=1000W/m^2 (b), the plots are adopted from [5]

Physically, active electrons can be activated in a PV cell of semiconductor materials at a solar radiation intensity and cell temperature. The active electrons can travel to the p-side from the n-side in the cell to form a current inside the cell. If the cell is connected to a circuit, the active electrons will go back to the n-side to combine with the holes left by the electrons through the circuit outside the cell, thus a current can be established in the circuit. The number of active electrons in the n-side generated per unit time is fixed at a given solar radiation intensity and cell temperature [9]. Therefore, the current curve exhibits a saturation property after the voltage is lower than a critical value as shown in Figure 3b. This saturation or choke behaviour is represented properly by the exponential function in Eq. (1).

2.2 Head-flow rate model for the pumps

The head-flow rate curves in Figure 2 are very similar to the current-voltage curve of the PV module in Figure 3b. Thus, an exponential function term should be involved in the mathematical model for head-flow rate curves of a partial emission pump. Inspired by the mathematical model of PV cells/modules, the following mathematical formula is proposed to fit the experimental data in Figure 2:

$$H = H_0 + aQ + bQ^2 - ce^{dQ^m} \quad (2)$$

where H and Q are pump head and flow rate, the coefficients H_0(>0), a, b, c(>0), d(>0), and m(>0) are determined based on a set of experimental H and Q data by using the least-squares method in Excel, and the number of scattered points of experimental data should be more than six. H_0 is the head at shut-off point. If c=0, then the 2nd-order polynomial for fitting head-flow rate curves of ordinary centrifugal pumps is recovered. The 2nd-order polynomial in Eq. (2) plays a role in fitting the flat part of a head-flow rate, but the exponential term takes the dramatic drop in the head-flow rate curve into account.

2.3 Method

The regression of Eq. (2) was performed against experimental data available by employing **Solver** in Excel. **Solver** is an add-in toolbox. It can be added into **Data** menu in Excel by clicking **File->Options->Add-ins->Solver**. The following steps are recommended to perform a sightly complicated curve fitting with a user mathematical model in Excel:

1) Experimental data of head and flow rate of a partial emission pump are read into Excel by occupying two columns;
2) Assign three columns to accommodate the initial and fitted coefficients, statistics results, head predicted with Eq. (2) and squared errors between the experimental head and the head predicted, respectively;
3) Calculate the sum of the squared errors and define it as the objective function by launching **Formula->Sum**;
4) Launch **Solver** to display the interface for the least-squares method by clicking **Data->Solver**, define the cell for reading and showing the objective function, optimization option, optimization algorithm;
5) Run **Solver**, if a converged solution has been resulted, check the coefficient of determination, R^2, compare the experimental and predicted heads; if not, alter the initial values of the fitted coefficients until a satisfactory solution is achieved.

An example of setup for experimental head-flow rate data, predicted head, coefficients, statistical results, and the interface of **Solver** for coefficient optimization is illustrated in Figure 4. In the figure, cells H73-H78 are used to store the initial and optimized five

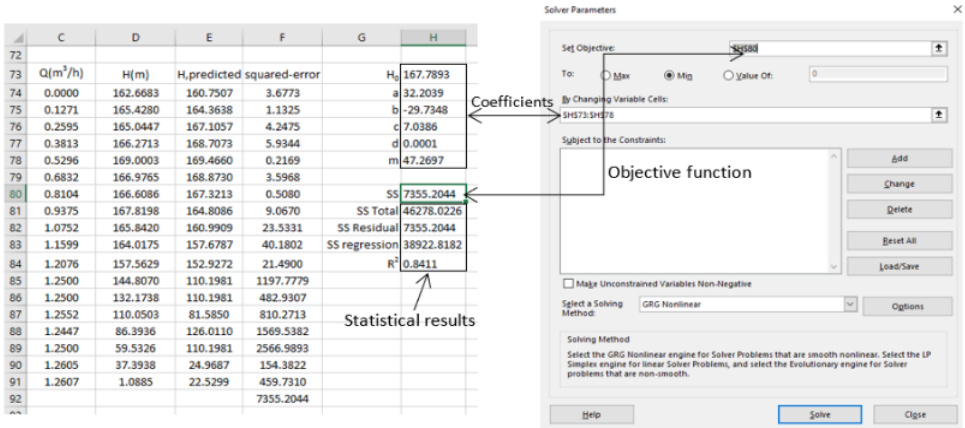

	C	D	E	F	G	H
72						
73	Q(m³/h)	H(m)	H,predicted	squared-error	H_0	167.7893
74	0.0000	162.6683	160.7507	3.6773	a	32.2039
75	0.1271	165.4280	164.3638	1.1325	b	-29.7348
76	0.2595	165.0447	167.1057	4.2475	c	7.0386
77	0.3813	166.2713	168.7073	5.9344	d	0.0001
78	0.5296	169.0003	169.4660	0.2169	m	47.2697
79	0.6832	166.9765	168.8730	3.5968		
80	0.8104	166.6086	167.3213	0.5080	SS	7355.2044
81	0.9375	167.8198	164.8086	9.0670	SS Total	46278.0226
82	1.0752	165.8420	160.9909	23.5331	SS Residual	7355.2044
83	1.1599	164.0175	157.6787	40.1802	SS regression	38922.8182
84	1.2076	157.5629	152.9272	21.4900	R^2	0.8411
85	1.2500	144.8070	110.1981	1197.7779		
86	1.2500	132.1738	110.1981	482.9307		
87	1.2552	110.0503	81.5850	810.2713		
88	1.2447	86.3936	126.0110	1569.5382		
89	1.2500	59.5326	110.1981	2566.9893		
90	1.2605	37.3938	24.9687	154.3822		
91	1.2607	1.0885	22.5299	459.7310		
92				7355.2044		

Figure 4. Experimental head-flow rate curve fitting set-up by using Solver in Excel, the right-experimental data, coefficients, model prediction, objective function, and statistical results, the left-interface of Solver for coefficient optimization, SS-sum of squares; in Excel cells, SS Total: H81=COUNT(D74:D91)*VARP(D74:D91), SS Residual: H82=SUMXMY2(D74:D91,E74:E91), SS Regression: H83=H81-H82, R^2: H84=H83/H81, In Excel, COUNT is the function counts the number of cells that contain numbers; VARP is the function that calculates variance based on the entire population, SUMXMY2 is the function that returns the sum of squares of differences of corresponding values in two arrays, R^2 is the coefficient of determination, a statistical measure that uses the variance of one variable to explain the variance of another, R^2=(SS Total-SS Residual)/SS Total

coefficients, cell H80 is for the sum of errors squared in head, cells H81-H84 accommodate the statistical results, cells E74-E91 are utilized to predict a head with six coefficients and a known flow rate, say cell E74 should be assigned with a formula such as H73+H74*C74+1*H75*C74^2-H76*EXP(H77*C74^H78) and so on, where cell C74 represents the flow rate. If the 2nd-oder term is expected to exclude from Eq. (2), the '1' in the formula is altered to '0', i.e. 1*H75*C74^2->0*H75*C74^2.

In the curve fitting process for **Solver,** a set of initial values of the coefficients H_0, a, b, c, d, and m is needed. A few sets of initial values should be tried until **Solver** is convergent with a better coefficient of determination. Once the Solver is convergent with a satisfactory coefficient of determination, the coefficients H_0, a, b, c, d, and m will be unique.

3. Results

Because the experimental data relating to partial emission pumps were very limited in the literature, firstly, the head-flow rate curve fitting model and method above were applied to five experimental partial emission pumps with very low specific speeds such as n_s=23 [1], n_s=20 [10], n_s=19 [11], n_s=17 [12], and n_s=31 [13]. The predicted heads are compared with the measurements in Figure 5. The determined corresponding coefficients in Eq. (2) are listed in Table 1 and 2. The specific speed of partial emission pumps is defined at best efficiency point or duty point by:

$$n_s = \frac{3.65n\sqrt{Q}}{H^{3/4}} \tag{3}$$

where n is pump rotative speed, r/min, H is pump head, m, Q is pump flow rate, m^3/s. The experimental data in Figure 5a, 5d and 5e demonstrate the heat-flow rate curves as the impeller rotational speed, number of blades and impeller diameter vary.

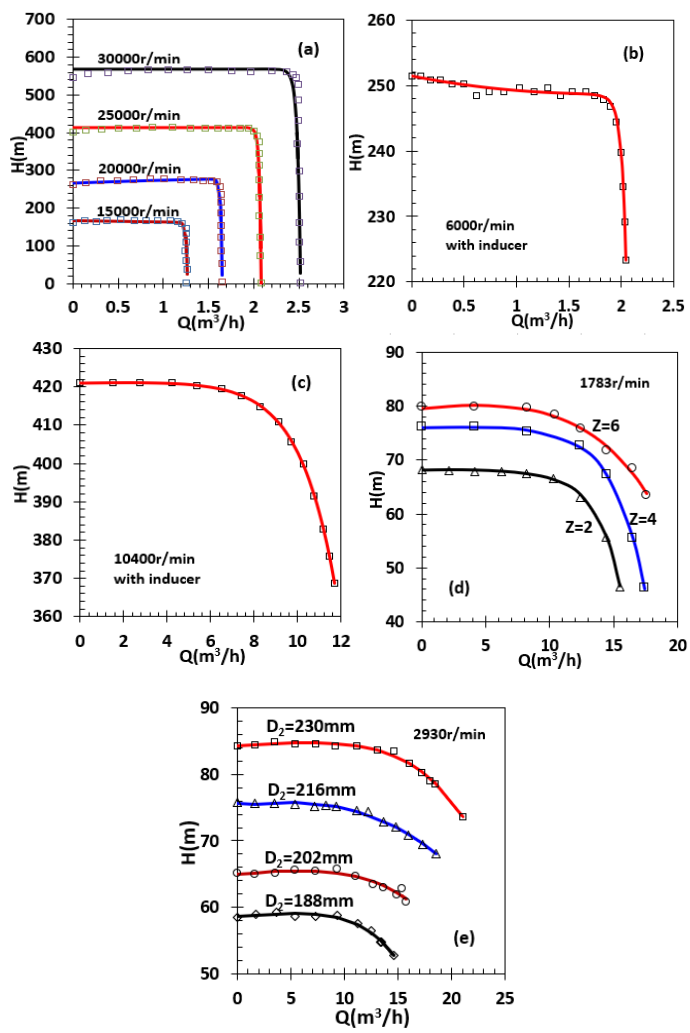

Figure 5. Experimental and fitted head-flow rate curves of existing four partial emission pumps found in the literature, (a) n_s=23 [1], (b) n_s=20 [10], (c) n_s=19 [11], (d) n_s=17 [12], (e) n_s=31 [13], the lines for fitted curves with Eq. (2), Z-number of blades, D_2-impeller diameter, the symbols represent the experimental data in [1], [10]-[13], respectively

Table 1 Coefficients in Eq. (2) for the cases shown in Figure 5a-5c

Coefficient	n(r/min)					
	Figure 5a				Figure 5b	Figure 5c
	15000	20000	25000	30000	6000	10400
H_0(m)	178.2723	267.2406	413.2755	567.5908	251.4171	421.0318
a	-3.5770	9.2860	1.8542e-13	1.8542e-13	-3.1045	1.1534e-1
b	-29.7348	-1.5236	1.9029e-2	1.9231e-2	9.0563e-1	-3.0905e-3
c	11.2971	1.5490e-4	3.1838e-5	8.2953e-5	1.7311e-2	4.3175e-1
d	5.9866e-5	2.4978e-1	1.0476e-1	1.3744e-1	6.0485e-2	6.0946e-1
m	46.0748	8.0596	6.8938	5.1233	6.7033	1.0000
R^2	0.8380	0.8882	0.9091	0.8978	0.9954	0.9999

Table 2 Coefficients in Eq. (2) for the cases in Figure 5d and 5e

Coefficient	Z in Figure 5d			D_2(mm) in Figure 5e			
	2	4	6	230	216	202	188
H_0(m)	76.0433	79.6560	68.0717	84.4175	78.4502	64.9253	58.5929
a	0.0593	0.3438	0.0682	0.2026	0.8971	0.2248	0.1569
b	-0.0029	-0.0201	-0.0123	0	0	0	0
c	0.0418	0.0939	0.0246	0.1888	2.7750	0.0232	0.0174
d	0.3062	0.6112	0.1736	0.3128	0.3269	1.4085	0.9521
m	1.0734	0.7420	1.3341	0.8666	0.6648	0.5094	0.6960
R^2	0.9995	0.9926	0.9990	0.9934	0.9930	0.9171	0.9857

In Figure 5a, the curve fitting is sightly poor because the coefficients of determination are R^2=0.84, 0.89, 0.91, 0.90 at 15000, 20000, 25000, 30000r/min, respectively, in Table 1. R^2 is the coefficient of determination reflecting the proportion of the variation in head that is predictable from flow rate. In the other cases, as shown in Figure 5b-e, the curve fittings are quite good since the coefficients of determination are as great as R^2=0.92-0.99 shown in Table 2. These facts suggest that the mathematical model expressed by Eq. (2) is applicable to the cases with fixed impeller rotational speed and geometry but also is adaptive to the change in either impeller speed or geometry.

Secondly, the experimental data of additional two partial emission pumps with a bit high specific speeds at n_s=69, 80 in [2] were fitted by using Eq. (2) and are compared with the fitting curves in Figure 6, meanwhile the corresponding fitting coefficients are listed in Table 3. The variation of the experimental head against the flow rate is more complicated than that in Figure 5, the fitting is not perfect near the region where the head starts to drop off sharply. In other words, the fitting curves near that region are smoother than those in the experimental data. Consequently, the R^2 values are in the range of 0.94-0.98. Overall, the fitting results are satisfactory.

4. Discussion

As shown in Figure 5, the head curve of three partial emission pumps is flat in a wide range of flow rate and then drops off with increasing flow rate. One may think that the flat part in the head curve would be the most suitable for the operation of partial emission pumps and it is sufficient to fit the flat part in the curve rather than the whole curve. Unfortunately, the pump efficiency in the flat part of the curve is lower than in the elbow of the curve, see Figure 7. To achieve a better efficiency, a partial emission pump can operate in the elbow of the curve. In this case, fitting the whole head curve of the pump is necessary.

The rapid drop in the head with increasing flow rate shown in Figure 2 is due to the saturation or choke effect of flow through the diffuser throat of the volute at a high flow rate. Also, this effect results in a large amount of hydraulic loss in the volute or even cavitation at the volute tongue [13] and leads to a remarked head drop. Obviously, this effect resembles the current saturation or choke behaviour in a PV cell. The exponential function of the last term in Eq. (2) is employed to handle this effect mathematically.

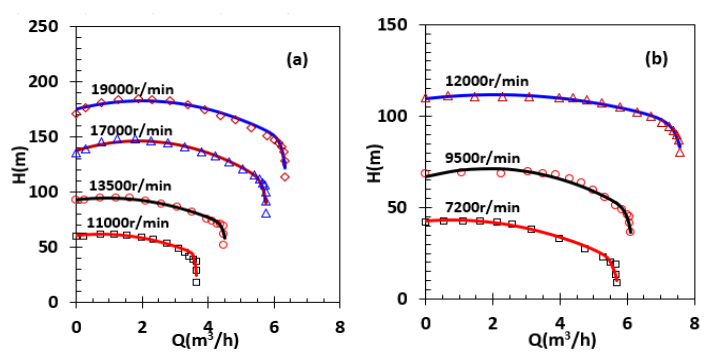

Figure 6. Experimental and fitted head-flow rate curves of existing two partial emission pumps found in [2], (a) n_s=69, (b) n_s=80, the lines for fitted curves with Eq. (2), the symbols represent the experimental data in [2]

Table 3 Coefficients in Eq. (2) for the cases shown in Figure 6

Coefficient	n(r/min)						
	Figure 6a				Figure 6b		
	11000	13000	17000	19000	7200	9500	12000
H_0(m)	60.5195	92.9577	137.9416	175.0071	42.4756	67.0659	109.5380
a	3.1587	3.4674	9.2794	7.4943	1.3438	4.7721	2.1250
b	-2.1351	-1.8603	-2.4424	-1.8765	-8.8415e-1	-1.2698	-5.1330e-1
c	1.9932e-5	1.5943e-3	4.5343e-4	2.1998e-5	1.6318e-5	2.9735e-4	1.4335e-3
d	4.2687e-3	7.3030e-4	1.0976e-3	3.2434e-3	4.5655e-2	1.4251e-3	2.1222e-3
m	6.2347	6.2700	5.2426	4.5320	3.2659	4.9244	4.1350
R^2	0.9459	0.9536	0.9467	0.9623	0.9779	0.9768	0.9866

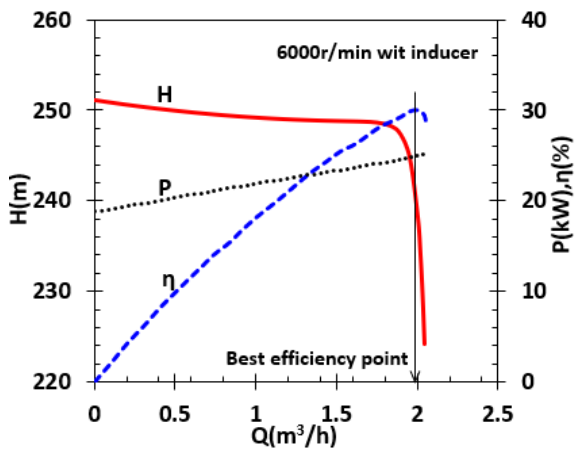

Figure 7. Head H, shaft-power P and efficiency η curves of the partial emission pumps tested in [10].

In pump industry and its application sectors, the head-flow rate curve of centrifugal pumps is usually expressed by using a 2nd or even higher order polynomial, for example, in the work presented in [14-18]. Furthermore, orthogonal polynomials are employed to fit experimental data of centrifugal or axial-flow pumps [19]. Interestingly, the following mathematical model was proposed to fit the experimental data of head of centrifugal pumps [20]:

$$H = H_0 - ce^{dQ} \tag{4}$$

where H_0, c and d are fitting coefficients. Obviously, Eq. (4) is a simplified version of Eq. (2) when the conditions: a=b=0 and m=1 are held. Therefore, the work presented in the paper is innovative to partial emission pumps.

In Figure 5c-5e, the head reduces more gently with increasing flow rate than in Figure 5a and 5b, and the head-flow rates resemble to the curves of centrifugal pumps, thus the m values are close to 1, as shown in Table 1 and 2. Hence, the mathematical model Eq. (2) are suitable for centrifugal pumps as well.

5. Conclusions

A mathematical model was proposed for the experimental head-flow rate curve fitting of partial emission pumps and implemented in Excel. The physics behind the model was explained based on the flow rate saturation effect in the pumps. The model can produce high-quality curve fitting based on the experimental head-flow rate data of seven partial emission pumps collected in the literature and is more general than the existing mathematical models. It is hopeful that the model can find applications to experimental data processing in the pump industry soon. The author can provide the supplementary data in Excel file on request.

Acknowledgment

This study was not supported by a project, thus no funding source was appreciated.

Nomenclature

a	coefficient in Eq. (2)
b	coefficient in Eq. (2)
c	coefficient in Eq. (2)
d	coefficient in Eq. (2)
D_1	inlet diameter of impeller (mm)
D_2	outlet diameter of impeller (mm)
H	pump head (m)
H_0	coefficient in eq. (2) (m)
I	output current of flat photovoltaic cell/module (A)
I_d	diode reversal saturation current shown in Figure 3a (A)
I_{ph}	photocurrent shown in Figure 3a (A)
k	Boltzmann constant, k=1.38065031×10^{-23}J/K
n	rotational speed of impeller (r/min)
m	power in Eq. (2)
M	diode quality factor
n_s	pump specific speed defined by Eq. (3)
q	electron charge, q=1.60217646×10^{-19}C
P	pump shaft-power (kW)
Q	pump flow rate, (m^3/h) or (m^3/s)
R_s	combined series resistance shown in Figure 3a (Ω)
R_{sh}	shunt resistance shown in Figure 3a (Ω)
R^2	coefficient of determination defined in caption of Figure 4
S	solar radiation intensity (W/m^2)
T	cell temperature (K)
V	Output voltage of flat photovoltaic cell/module (V)
Z	number of blades
η	pump efficiency (%)

ω	rotational angular speed of impeller (rad/s)
PV	photovoltaic
SS	sum of squares

Conflict of Interest Statement

The author declares that there is no conflict of interest in the study.

CRediT Author Statement

Wenguang Li: Conceptualization, Methodology, Software, Writing-original draft, review, and editing.

References

1. Barske, U. M. (1960). Development of some unconventional centrifugal pumps. Proceedings of Institute of Mechanical Engineers, 174, 437-461.
2. Lock, T. (1966). A forced vortex pump for high speed, high pressure, low flow applications. SAE Transactions, 74, 729-737.
3. Finder, P. (2022). Partial Emissions Pump Series' Dual PEP. Accessed December 24, 2022. Available at https://www.offshore-technology.com/contractors/pumps/finder-pompe/pressreleases/dual-pep-series/
4. Li, W. (2021). Affinity laws for impellers trimmed in two partial emission pumps with very low specific speed. Proc IMechE Part C: Journal Mechanical Engineering Science, 235, 859-877.
5. Li, W., Paul, M. C., Sellami, N. et al. (2016). Six-parameter electrical model for photovoltaic cell/module with compound parabolic concentrator. Solar Energy, 137, 551-563.
6. Li, W., Paul, M. C., Rolley, M. et al. (2017). A coupled optical-thermal-electrical model to predict the performance of hybrid PV/T-CCPC rooftop systems. Renewable Energy, 112, 166-186.
7. Li, W., Paul, M. C., Rolley, M, et al. (2017). A scaling law for monocrystalline PV/T modules with CCPC and comparison with triple junction PV cells. Applied Energy, 202, 755-771.
8. Li, W., Paul, M. C., Baig, H. et al. (2019). A three-point-based electrical model and its application in a photovoltaic thermal hybrid roof-top system with crossed compound parabolic concentrator. Renewable Energy, 130, 400-415.
9. Hersch, P. & Zweibel, K. (1982). Basic Photovoltaic Principles and Methods, SERI/SP-290-1448, Oak Ridge: Technical Information Office.
10. Wilk, A. (2008). Pressure distribution around pump impeller with radial blades: Proceedings of 6th IASME/WSEAS International Conference on Fluid Mechanics and Aerodynamics, Rhodes, Greece, August 20-22.
11. Shui, Q., Jiang, T., Pan, B. et al. (2021). Numerical research on performance of high-speed partial emission pump. Shock and Vibration, Article ID 6697063.
12. Turton, R. K. (1973). The open impeller pump, Process Pumps. Institution of Mechanical Engineers: London, UK.
13. Fan, Z. L, & Wang, G. T. (2002). Experiment on partial emission pumps. Pump Technology, 2, 3-8.
14. Yang, Z. & Børsting, H. (2010). Energy efficient control of a boosting system with multiple variable-speed pumps in parallel: Proceedings of the 49th IEEE Conference on Decision and Control Hilton Atlanta Hotel, Atlanta, USA, December 15-17.
15. Chang, W., Chang, J. W., Yin, H. et al. (2012). Energy-saving algorithm for pumping systems based on fuzzy decision making: Proceedings of the IEEE International Conference on Systems, Man, and Cybernetics, COEX, Seoul, Korea, October 14-17.
16. Luo, Y., Yuan, S., Sun, H. et al. (2015). Energy-saving control model of inverter for centrifugal pump systems. Advances in Mechanical Engineering, 7, 1-12.
17. Cheng, Q., Ma, Y., Yang, J, et al. (2019). Fitting and correction of H-Q performance curve of centrifugal pump. Journal of Petrochemical Universities, 32, 78-84.
18. Müller, T. M., Leise, P., Lorenz, I. et al. (2021). Optimization and validation of pumping system design and operation for water supply in high-rise buildings. Optimization and Engineering, 22, 643-686.
19. Zhou, L. C. & Qiu, C, X. (2001). Orthogonal polynomial fitting for pump characteristic curves. Drainage and Irrigation Machinery, 19, 8-11.
20. Liao, L., Lin, J., Zhang, C. (2002). Efficiency optimization of variable frequency variable speed water-supply pumping stations based on genetic algorithm. Engineering Science, 4, 54-58.

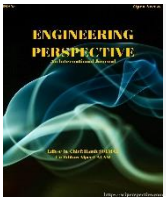

e-ISSN:2757-9077

ENGINEERING PERSPECTIVE

https://sciperspective.com/ Research Paper

Integrated Vehicle Dynamics Modeling, Path tracking, and Simulation: A MATLAB Implementation Approach

Fatima Haidar[1*], Abderaouf Laib[1], Syed Ali Ajwad[1], Guillaume Guilbert[1]

[1] *Capgemini Engineering, Research & Innovation Direction, 12 rue de la Verrerie, 92190, Meudon, France*

ABSTRACT

This paper presents a thorough exploration of vehicle dynamics modeling and simulation, focusing on lateral, longitudinal, and vertical motion. A comprehensive mathematical representation of a car-like vehicle is developed, incorporating both kinematic and dynamic models to accurately capture its behavior. Initially, a kinematic model is established to describe fundamental motion in a 2D plane, while a subsequent dynamic model considers various forces influencing the vehicle's motion in a 3D space. The vertical motion of the vehicle is primarily influenced by its suspension systems. In this paper, we initially introduced a fundamental 2 Degree of Freedom (DOF) quarter car suspension model and subsequently presented a more comprehensive half car suspension model which accounts for both the front and rear body parts of the vehicle. The developed models are implemented using MATLAB/Simulink, enabling rigorous testing and validation of their accuracy. Simulation results demonstrate the precision of the developed models, consistently aligning with expected vehicle behavior under different input conditions. Specifically, the models accurately replicate vehicle motion in straight lines and circular patterns, corresponding to longitudinal speed and steering angle inputs. Additionally, a path tracking controller is integrated to showcase the model's efficiency and validate its derived parameters. The reliability and accuracy of the thoroughly developed models underscore their suitability for algorithm development and validation, essential for advancing autonomous vehicle technology and enhancing vehicle safety and performance.

Keywords: Autonomous vehicle; Mathematical modelling; Trajectory tracking; Vehicle dynamics.

History
Received: 14.12.2023
Accepted: 27.01.2024

Author Contacts
**Corresponding Author*
e-mail addresses : Fatima.haidar@capgemini.com, abderaouf.laib@capgemini.com, syed-ali.ajwad@capgemini.com, guillaume.guilbert@capgemini.com

How to cite this paper: Haidar, F., Laib, A., Ajwad, S.A., Guilbert, G., (2024). Integrated Vehicle Dynamics Modeling, Path tracking, and Simulation: A MATLAB Implementation Approach. Engineering Perspective, 4 (1), 7-16. http://dx.doi.org/10.29228/eng.pers.75106

1. Introduction

Since the last few decades, the automotive industry and the market structure has changed in an unprecedented way. There were simultaneous growing needs for vehicle safety, environmental protection, and intelligent control. As a result, the use of advanced technologies such as computer technologies, virtual reality technologies and intelligent algorithms became widespread in the industry. Thanks to these advanced technologies, the automotive industry focused on the design and testing of new Advanced Driving Assistance System (ADAS) functionalities to enhance not only the safety but also the performance and comfort of the vehicle and its passengers. The ADAS functionalities include lane keeping [1] but also adaptive cruise control [2], lane assistance [3], emergency braking [4], and parking assistance [5] among others. In recent times, fully Autonomous Driving (AD) is also becoming an increasingly interesting topic of research in the automotive industry [6] in which more advanced algorithms are required for trajectory planning and controlling.

Vehicle dynamics plays an important role in the automotive industry development [7]. The mathematical models not only allow to understand the behavior of the vehicle, but one can also use these models to verify and validate the developed algorithms in simulation before implementing them on the real hardware [8]. This allows a significant cost reduction. Moreover, by studying the complex interactions between a vehicle's components, such as its tires, suspension, and steering system, researchers can identify potential safety hazards

and develop innovative solutions to improve vehicle safety [9].

Initially, research on vehicle dynamics focused on analyzing the vehicle's performance under various external conditions and service requirements. During the 1930s, there was a notable shift in research focus towards the steering, suspension mechanics, and driving stability of the vehicles [10]. Researchers like Lanchester Maurice and Segel began to examine how external environmental factors, such as road surface roughness, air flow, tire conditions, and driver behavior, impacted the vehicle dynamics. Additionally, they studied the interrelated effects of these various conditions [11]. In 1993, they provided a detailed overview of the progress made in vehicle dynamics research prior to 1990 in the Proceedings of Institution of Mechanical Engineers [12].

Over the subsequent decades, significant research has been devoted to investigating vehicle ride comfort and handling stability. The study of handling dynamics concerns primarily the lateral or transverse dynamics of the vehicle, including its handling, stability, vehicle sideslip resulting from tire lateral force, yawing, and roll motion. The research on vehicle handling stability in vehicle dynamics has evolved from experimental studies to theoretical analysis and from open-loop to closed-loop systems. The representative monographs of vehicle handling dynamics include "Vehicle Handling Dynamics Theory and Application" by Abe [13] and "Overview on Vehicle Dynamics" by Yang [7].

Vehicle driving dynamics is divided into two categories: longitudinal and lateral dynamics. Longitudinal dynamics concerns the motion of a vehicle along its longitudinal axis, which includes acceleration, braking, and the resulting changes in velocity. It also considers various resistive forces which influence the longitudinal movement of the vehicle [14]. Lateral dynamics on the other hand concerns the motion of a vehicle perpendicular to its longitudinal axis, which includes turning, cornering, and the resulting changes in direction. Both longitudinal and lateral dynamics are critical for vehicle handling, safety, and overall performance. Relevant monographs in this area can be found in "Vehicle Dynamics and Control" by Rajamani [15]. Another pivotal aspect of vehicle dynamics is the vertical motion regulated by the vehicle suspension system. Therefore, a comprehensive vehicle suspension mathematical model is of utmost importance to analyse and optimize the vehicle's behaviour. This model not only profoundly influences the overall dynamics of the vehicle but also serves as a key component of vehicle stability, ride comfort, handling, and safety [16]. In recent times, researchers have also developed mathematical models not only for electric and hybrid powertrains and propulsion systems[17,18] but also for braking [14]and speed transmission systems [19]. However, it's crucial to highlight that vehicle motion dynamics models serve as pivotal components for testing and verifying these intricate models.

The main objective of this work is to create precise and efficient simulations by delving into key aspects of vehicle behavior. These aspects encompass lateral vehicle dynamics, longitudinal vehicle dynamics and vehicle suspension dynamics. The lateral vehicle dynamics pertains to the vehicle's turning behavior, providing insights that enable the effective design of control systems. Longitudinal vehicle dynamics have been modeled to investigate acceleration, deceleration, and speed control responses to driver inputs and external factors. Furthermore, a vehicle suspension systems model has been developed to simulate the vehicle's reaction to uneven road surfaces, therefore, enhancing ride comfort and stability, that are integral to

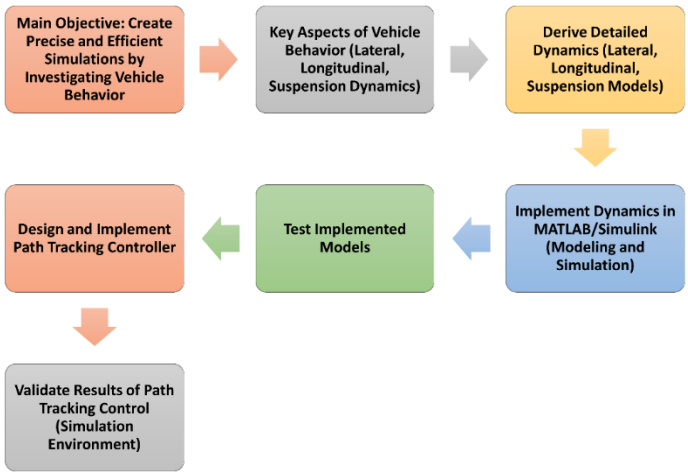

Figure 1. Flowchart summarizing the entire study.

passenger safety. Compared to the previous literature, this paper not only advances the understanding of the vehicle's motion but also combines all three dynamics models to obtain a better analysis of the vehicle's behavior in real driving scenarios, emphasizing safety considerations. A detailed derivation of these dynamics is provided in the paper. In the next step, these dynamics are implemented in MATLAB/Simulink. The implemented models are tested with various input signals. Finally, a path tracking controller is designed and implemented. The results of path tracking control show that the developed mathematical models mimic the real motion of a vehicle and can be used to design and validate algorithms for ADAS and AD in a simulation environment.

The flowchart as shown in Figure 1 begins with the main objective of the study, which is to create precise and efficient simulations by investigating key aspects of vehicle behavior (section 1). It outlines the key aspects, including lateral, longitudinal, and suspension dynamics (section 2). The detailed dynamics are derived, implemented in MATLAB/Simulink, and tested with various input signals. A path tracking controller is designed and implemented (section 3), followed by the validation of results in a simulation environment (section 4).

2. Vehicle model description

This section discusses the derivation of vehicle mathematical modeling. First, the basic coordinate representation is described. Then both kinematic and dynamic models are discussed in detail.

2.1 Coordinate system

In vehicle dynamics, understanding coordinate systems is crucial for accurately analyzing the vehicle's behavior. In order to develop the model, two coordinate frames are required i.e. the inertial frame and the body-fixed frame. The inertial frame is a reference frame that is fixed relative to the Earth's surface and does not move, while the vehicle frame is a reference frame that is fixed relative to the vehicle and moves with the vehicle's motion. Figure 2 depicts the reference coordinates. The parameters, which are the variable components essential in deriving the characteristics of the vehicle, are described

beneath each corresponding equation.

Figure 2. Reference coordination.

2.2 Kinematic model

The kinematics of a 4-wheel vehicle can be simplified as 2-wheel bicycle model by merging the front and rear wheels. This reduces the complexity of dealing with 4 wheels and 2 steering angles to only 2 wheels and 1 steering angle. Let us consider that the body reference frame is at the center of gravity of the vehicle as shown in Figure 2. ψ describes the orientation of the vehicle, V is the velocity at the center of gravity and β is the slip angle.

The motion of the vehicle can then be described as in the Eq. (1) below:

$$\begin{cases} \dot{X} = V \ \cos(\psi + \beta) \\ \dot{Y} = V \ sine(\psi + \beta) \end{cases} \tag{1}$$

While the angular speed $\dot{\psi}$ can be given as:

$$\dot{\psi} = \frac{V}{R} \tag{2}$$

Where R is the perpendicular distance from the reference point to the Instantaneous Center of Rotation (ICR) represented in Figure 3 as O.
Using basic angle geometry, it can be found that the intersecting angle between the front and rear perpendicular lines is equal to δ, thus leading to the following Eq. (3):

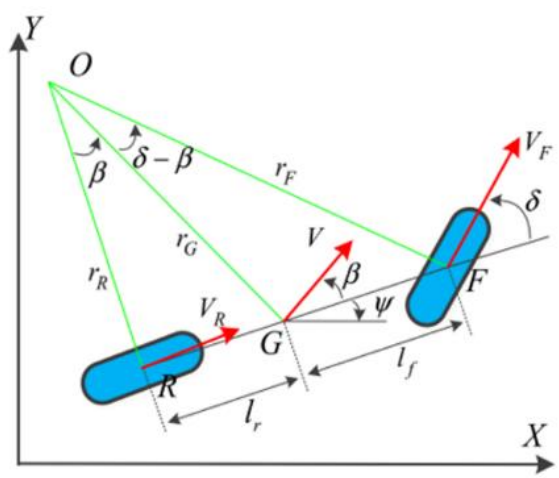

Figure 3. Two-wheel bicycle model [20].

$$\tan(\delta) = \frac{l_f + l_r}{r_R}, \tan(\beta) = \frac{l_r}{r_R} \tag{3}$$

Where l_r and l_f are the distances between the center of gravity and the rear and front axles respectively, r_R represent the distance between O to center of rear axle. From the above equations, the following Eq. (4) is obtained:

$$\begin{cases} \dot{\psi} = \dfrac{V}{l_r + l_f} cos(\beta)\, tan(\delta) \\ \beta = arctg\left(\dfrac{l_r}{l_r + l_f} \ \ tan(\delta)\right) \end{cases} \tag{4}$$

Eq. (1) and Eq. (4) combined describe the kinematics of the vehicle.

2.3 Dynamic model

In order to keep the model simple, some key assumptions were made. First, the vehicle is considered as a rigid body, whose dynamics is determined by the fundamental laws of motion. Second, the steering angle is small, which allows us to make the small-angle approximations such as $\cos(\delta) \approx 1$ and $\sin(\delta) \approx 0$.

- ***Lateral Dynamics***

Let us consider the free body diagram shown in Figure 4. According to Newton's second law:

$$\sum F = ma \quad \text{and} \quad \sum M = Iz \ \ddot{\Psi} \tag{5}$$

Where $\sum F$ represent the sum of forces, m represents the vehicle mass and a represent the vehicle acceleration. As well as $\sum M$ represent the sum of all moments, Iz represents the moment of inertia and $\ddot{\Psi}$ represents the angular acceleration of the vehicle.

Considering the lateral forces on front and rear tires in the small-angle approximation. The lateral acceleration is a combination of $\dot{V}_y$, which is due to the motion along the y axis, and $\ddot{\Psi} V_x$, referred to as centripetal acceleration. Therefore, the following Eq. (6) is obtained:

$$F_{yf} + F_{yr} = m(\dot{V}_y + \ddot{\Psi} V_x) \tag{6}$$

Now taking the moment around the center of gravity G:

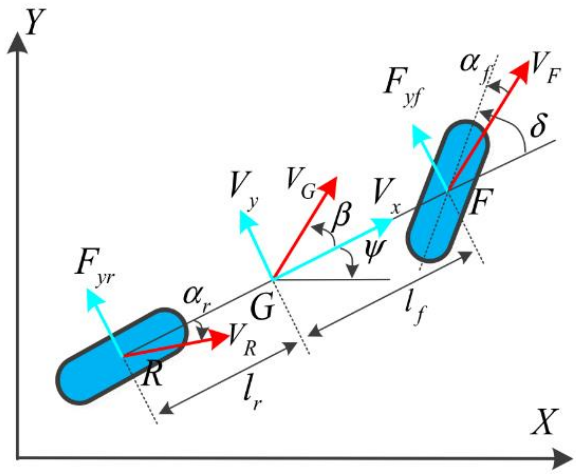

Figure 4. Free body diagram [20].

$$F_{yf} l_f - F_{yr} l_r = I_z \ddot{\Psi} \tag{7}$$

The slip angle of front and rear tire can be expressed as:

$$\alpha_f = \delta - \frac{V_y + l_f \dot{\varphi}}{V_x} \text{ and } \alpha_r = \frac{V_y - l_r \dot{\varphi}}{V_x} \tag{8}$$

Using the cornering stiffness of the tire, F_{yf} and F_{yr} are expressed as in the following Eq. (9):

$$F_{yf} = C_f \alpha_f \text{ and } F_{yr} = -C_r \alpha_r \tag{9}$$

Combining all above equations, the lateral model in the state-space can be represented as in Eq. (10):

$$\frac{\mathrm{d}}{\mathrm{d}t}\begin{bmatrix} Y \\ \dot{Y} \\ \psi \\ \dot{\psi} \end{bmatrix} = \begin{bmatrix} 0 & 1 & 0 & 0 \\ 0 & -\frac{c_f + c_r}{m V_x} & 0 & -(V_x + \frac{c_f l_f - c_r l_r}{m V_x}) \\ 0 & 0 & 0 & 1 \\ 0 & -\frac{c_f l_f - c_r l_r}{I_z V_x} & 0 & -\frac{l_f^2 c_f + l_r^2 c_r}{I_z V_x} \end{bmatrix} \times \begin{bmatrix} Y \\ \dot{Y} \\ \psi \\ \dot{\psi} \end{bmatrix} + \begin{bmatrix} 0 \\ \frac{c_f}{m} \\ 0 \\ \frac{c_f l_f}{I_z} \end{bmatrix} \delta \tag{10}$$

- ***Longitudinal Dynamics***

The longitudinal dynamics describes the motion and behavior of vehicles along their longitudinal axis, which involves acceleration, deceleration, braking, and the associated forces and interactions affecting the vehicle's motion. It directly influences the overall performance and handling characteristics of a vehicle. The ability to accelerate smoothly, maintain stability during braking, and ensure precise control over the vehicle's longitudinal motion are essential for a comfortable and safe driving experience. Consider a vehicle moving on an inclined road, the longitudinal forces acting on the body are shown in Figure 5.

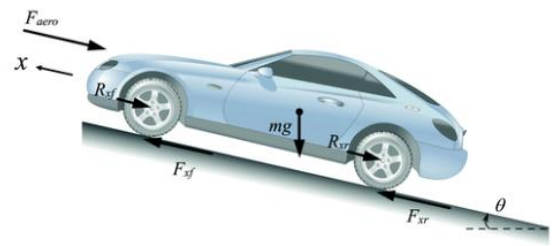

Figure 5. Longitudinal forces acting on the vehicle [15].

While in motion, a vehicle encounters multiple resistive forces due to various factors acting in the opposite direction to the movement. These resistance forces include rolling resistance, aerodynamic resistance, and weight resistance [14] . The force balance along the longitudinal axis leads to the following Eq. (11):

$$m\ddot{x} = F_{xf} + F_{xr} - F_{aero} - R_{xf} - R_{xr} - mg\sin\theta \tag{11}$$

Where Fxf represent the longitudinal tire force at the front tires, Fxr represent is the longitudinal tire force at the rear tires, $Faero$ represent the longitudinal aerodynamic drag force, Rxf represent the the force due to rolling resistance at the front tires, Rxr represent the force due to rolling resistance at the rear tires, m represent the mass of the vehicle, g represent the is the acceleration due to gravity and θ represent the angle of inclination of the road on which the vehicle is traveling.

The equivalent aerodynamic drag force on a vehicle can be represented as [21]:

$$F_{aero} = \frac{1}{2}\rho C_d A_F (V_x + V_{wind})^2 \tag{12}$$

Where, ρ is the mass density of air, C_d is the aerodynamic drag coefficient, A_F is the frontal area of the vehicle, V_x is the longitudinal vehicle velocity and V_{wind} is the wind velocity.

Similarly, the tire force can be expressed as in the following Eq. (13):

$$F_{xf} = C_{\alpha f} \alpha_{xf} \text{ and } F_{xr} = C_{\alpha r} \alpha_{xr} \tag{13}$$

Where $C_{\alpha f}$ and $C_{\alpha r}$ represents the longitudinal tire stiffness parameters of the front
and rear tires respectively, and α_x represents the slip or tire skidding and given as:

$$\alpha_x = \frac{r_{ref}\omega_w - V_x}{V_x} \tag{14}$$

Where R_x is the tire rolling resistance which refers to the force that opposes the motion of the tires as they roll on the road surface. If the road is inclined at an angle α, the rolling resistance R_x can be expressed as:

$$R_x = C_{rr} mg cos(\alpha) \tag{15}$$

Where C_{rr} is the rolling resistance coefficient. It depends on the tire construction, the materials, the air pressure, the vehicle speed, and the road conditions. In addition, m is the vehicle mas and g represent the gravitational acceleration.

- ***Suspension Dynamics***

The suspension system plays an important role in the stability of a vehicle operation [22]. It stands as a pivotal element that profoundly influences the vehicle dynamics and passenger comfort. Suspension systems can be categorized in three main classes: passive, semi-active and active. Passive suspension systems are traditional and common suspension systems that mainly rely on mechanical components like coil spring, shock absorber and connecting elements [16]. On the other hand, active suspension systems use electronic sensors and actuators to actively control vehicles height and damping characteristics. Semi-active suspension systems bridge between passive and active type by using just electronically control dampers.

In this paper, the work is focused on passive suspension systems. Figure 6 shows a schematic of a 2 Degree of Freedom (DOF) quarter car suspension.

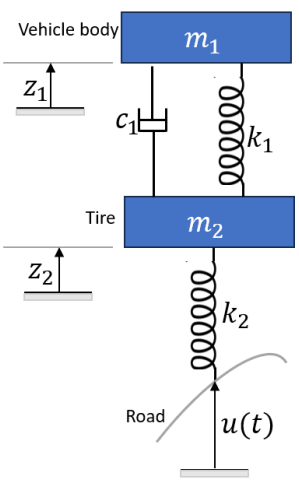

Figure 6. Two-degree of Freedom (DOF) quarter car suspension.

The equations of motion related to mass m_1 and m_2 are given in Eq. (16) and Eq. (17) by:

$$m_1\ddot{z}_1 = -k_1(z_1 - z_2) - c_1(\dot{z}_1 - \dot{z}_2) - F_a \tag{16}$$

$$m_2\ddot{z}_2 = k_1(z_1 - z_2) + c_1(\dot{z}_1 - \dot{z}_2) - k_2\big(z_2 - u(t)\big) - F_a \tag{17}$$

Where m_1 is the body mass, m_2 is the wheel mass, k_1& $k_2$are the stiffness coefficients, $c_1$is the damping coefficient, z_1 is the displacement of the body mass, $z_2$is the displacement of the wheel mass, F_a is the applied external force and $u(t)$ is the road input displacement. The state-space can be obtained from Eq. (16) and Eq. (17) such as:

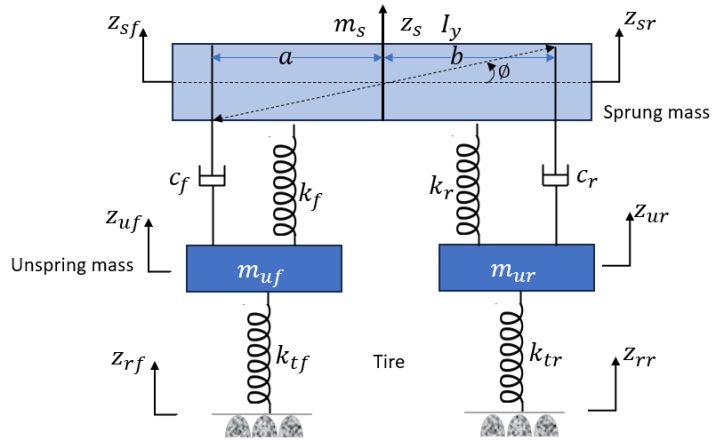

Figure 7. Two DOF half car suspension.

$$\begin{bmatrix}\dot{z}_1\\ \ddot{z}_1\\ \dot{z}_2\\ \ddot{z}_2\end{bmatrix} = \begin{bmatrix}0 & 1 & 0 & 0\\ -\frac{k_1}{m_1} & -\frac{c_1}{m_1} & \frac{k_1}{m_1} & \frac{c_1}{m_1}\\ 0 & 0 & 0 & 0\\ \frac{k_1}{m_2} & \frac{c_1}{m_2} & -\frac{(k_1+k_2)}{m_2} & -\frac{c_1}{m_2}\end{bmatrix} \times \begin{bmatrix}z_1\\ \dot{z}_1\\ z_2\\ \dot{z}_2\end{bmatrix} + \tag{18}$$

$$\begin{bmatrix}0 & 0\\ \frac{1}{m_1} & 0\\ 0 & 0\\ -\frac{1}{m_2} & \frac{k_2}{m_2}\end{bmatrix} \times \begin{bmatrix}F_a\\ u(t)\end{bmatrix} \quad and \quad y(t)= \begin{bmatrix}1 & 0 & 1 & 0\end{bmatrix}\begin{bmatrix}z_1\\ \dot{z}_1\\ z_2\\ \dot{z}_2\end{bmatrix}$$

A more comprehensive model can be represented through a half car suspension model. It considers a half car, including front and rear body parts. The free body diagram represented in Figure 7 is considered.

With the small angle approximation, the equation of motion related to half body mass m_s is given from Eq. (19) by:

$$m_s\ddot{z}_s = -k_f\big(z_s - z_{uf} - a\emptyset\big) - k_r(z_s - z_{ur} + b\emptyset) - c_f\big(\dot{z}_s - \dot{z}_{uf} - a\dot{\emptyset}\big) - c_r\big(\dot{z}_s - \dot{z}_{ur} + b\dot{\emptyset}\big) \tag{19}$$

Where: m_s is the body mass, $\emptyset$ represents pitch angle, k_f, k_r, k_{tf}, k_{tr} are the stiffness coefficients, a and b are the distances from the front and rear axle to the center of gravity respectively, z_s is the displacement of the body mass, z_{sf} and z_{sr} are the displacements of the front and rear body masses respectively, z_{uf} and z_{ur} are the displacements of the front and rear wheel masses respectively.

While the equations of motion related to front and rear wheels, $m_{\mu f}$ and $m_{\mu r}$ respectively, are given from Eq. (20) and Eq.(21) as:

$$m_{uf}\ddot{z}_{uf} = k_f\big(z_s - z_{uf} - a\emptyset\big) - k_{tf}\big(z_{uf} - z_{rf}\big) + c_f\big(\dot{z}_s - \dot{z}_{uf} - a\dot{\emptyset}\big) \tag{20}$$

$$m_{ur}\ddot{z}_{ur} = k_r(z_s - z_{ur} + b\emptyset) - k_{tr}(z_{ur} - z_{rr}) + c_r(\dot{z}_s - \dot{z}_{ur} + b\dot{\emptyset}) \quad (21)$$

Where m_{uf} and m_{ur} are the front wheel and rear wheel masses while c_f and c_r are the damping coefficients. While z_{rf} and z_{rr} are the road input displacements for the front and the rear wheel respectively.

In the half car model, the moment around the center of gravity must also be considered, such as in (22):

$$I_y\ddot{\emptyset} = ak_f(z_s - z_{uf} - a\emptyset) - bk_r(z_s - z_{ur} + b\emptyset) + ac_f(\dot{z}_s - \dot{z}_{uf} - a\dot{\emptyset}) - bc_r(\dot{z}_s - \dot{z}_{ur} + b\dot{\emptyset}) \quad (22)$$

Where I_y represents the moment of inertia.
The following state matrix is then obtained as in (23):

$$x = [\ z_s \quad \emptyset \quad z_{uf} \quad z_{ur} \quad \dot{z}_s \quad \dot{\emptyset} \quad \dot{z}_{uf} \quad \dot{z}_{ur}\ ]^T \quad (23)$$

The state space represented here after is then obtained as in (24) – (28):

$$\dot{x} = \begin{bmatrix} 0 & 0 & 0 & 0 & 1 & 0 & 0 & 0 \\ 0 & 0 & 0 & 0 & 0 & 1 & 0 & 0 \\ 0 & 0 & 0 & 0 & 0 & 0 & 1 & 0 \\ 0 & 0 & 0 & 0 & 0 & 0 & 0 & 1 \\ & -M^{-1}K & & & & -M^{-1}C & & \end{bmatrix} x + \begin{bmatrix} 0 & 0 \\ 0 & 0 \\ 0 & 0 \\ 0 & 0 \\ & M^{-1}F \end{bmatrix} u \quad (24)$$

Where:

$$C = \begin{bmatrix} c_f + c_r & bc_r - ac_f & -c_f & -c_r \\ bc_r - ac_f & c_f a^2 + c_r b^2 & ac_f & -bc_r \\ -c_f & ac_f & c_f & 0 \\ -c_r & -bc_r & 0 & c_r \end{bmatrix} \quad (25)$$

$$M = \begin{bmatrix} m_s & 0 & 0 & 0 \\ 0 & I_y & 0 & 0 \\ 0 & 0 & m_{uf} & 0 \\ 0 & 0 & 0 & m_{ur} \end{bmatrix} \quad (26)$$

K=

$$\begin{bmatrix} k_f + k_r & bk_r - ak_f & -k_f & -k_r \\ bk_r - ak_f & k_f a^2 + k_r b^2 & ak_f & -bk_r \\ -k_f & ak_f & k_f + k_{tf} & 0 \\ -k_r & -bk_r & 0 & k_r + k_{tr} \end{bmatrix} \quad (27)$$

$$F = \begin{bmatrix} 0 & 0 \\ 0 & 0 \\ k_{tf} & 0 \\ 0 & k_{tr} \end{bmatrix} \quad (28)$$

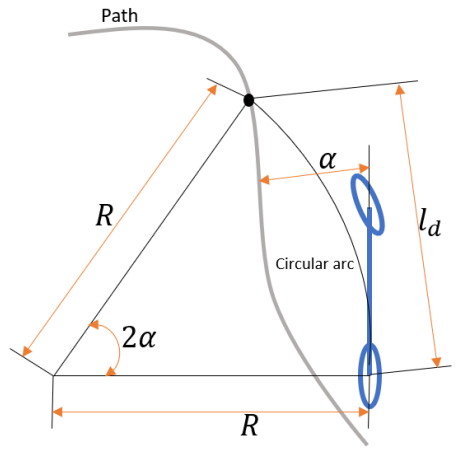

Figure 8. Representation of the principle of the Pure-Pursuit control.

3. Path tracking

A Pure-Pursuit control algorithm for lateral control was implemented with the developed dynamics of the vehicle in order to validate the model. In this section, a brief explanation of this controller is presented.

The pure pursuit technique [23,24] involves a geometric computation of the curvature of a circular arc, linking the position of the rear axle to a target point situated along the path ahead of the vehicle. This objective point is established based on a look-ahead distance l_d extending from the present rear axle position towards the intended path. The target point (g_x, g_y) is illustrated in Figure 8.

The steering angle δ of the vehicle can be found using solely the coordinates of the target point and the angle α formed between the vehicle's heading vector and the look-ahead vector, leading to the following equation:

$$\delta = arctan\left(\frac{2L\,sin(\alpha)}{l_d}\right) \quad (29)$$

4. Simulation results and discussion

The vehicle models for both longitudinal and lateral dynamic are implemented in MATLAB/ Simulink as shown in Figure 9. Longitudinal model of the vehicle computed through (11)-(15) is implemented in 'longitudinal vehicle dynamics' block while lateral model represented by (10) is realized in 'lateral vehicle dynamics' block. For the simulation purpose, the parameters of a Tesla Model S were considered. By incorporating these specific parameters, the objective is to conduct comprehensive simulations that closely mimic the real-world scenarios.

A half-car suspension model is also simulated in MATLAB/Simulink. The results are illustrated in Figure 10 (a-b). The suspension system is subjected to two different disturbance signals for the front and rear wheels. These results demonstrate the evolution of body displacement. An examination of the graphs reveals a key principle of this system's operation: the maximum body displacement is half that of the wheel's maximum displacement, highlighting an essential characteristic of the system's behavior.

Vehicle longitudinal and lateral dynamics are tested with various inputs. The initial states of the vehicle are set as $X_0 = 0$, $Y_0 = 0$, $\psi_0 = pi/4$ and $V_{x_0} = 0m/s$. First, the steering angle is fixed as 0 with a lateral speed of $20km/h$. A Proportional-Integral-Derivative (PID) controller is used to achieve desired lateral speed. The tunning proportion, integral and derivative tunning gains are chosen as 20, 4 and 3 respectively. Figure 11 shows the obtained results for this case. Figure 11-a depicts the longitudinal speed while Figure 11-b illustrates the position of the vehicle. Since the steering angle is fixed, the vehicle moved in a straight line. In the second case, the steering angle of the vehicle is kept constant at the value of $\pi/16\ rad$ while keeping the same longitudinal speed profile and initial conditions. The obtained result is shown in Figure 12. As anticipated, the vehicle executed a precise circular motion, showcasing the accuracy of the model.

The path tracking task involved following a predefined path represented by a series of waypoints. The pure-pursuit controller is used to control the lateral motion of the vehicle through appropriate steering commands. The lookahead distance was dynamically adjusted to ensure a smooth tracking. Figure 13 shows the path tracking results along with the trajectory error. One can see that the maximum tracking error is always less than 0.025 meter which indicates that the d esired trajectory is followed quite accurately. Moreover, the simulation results also signify the accuracy of the developed mathematical models and controller.

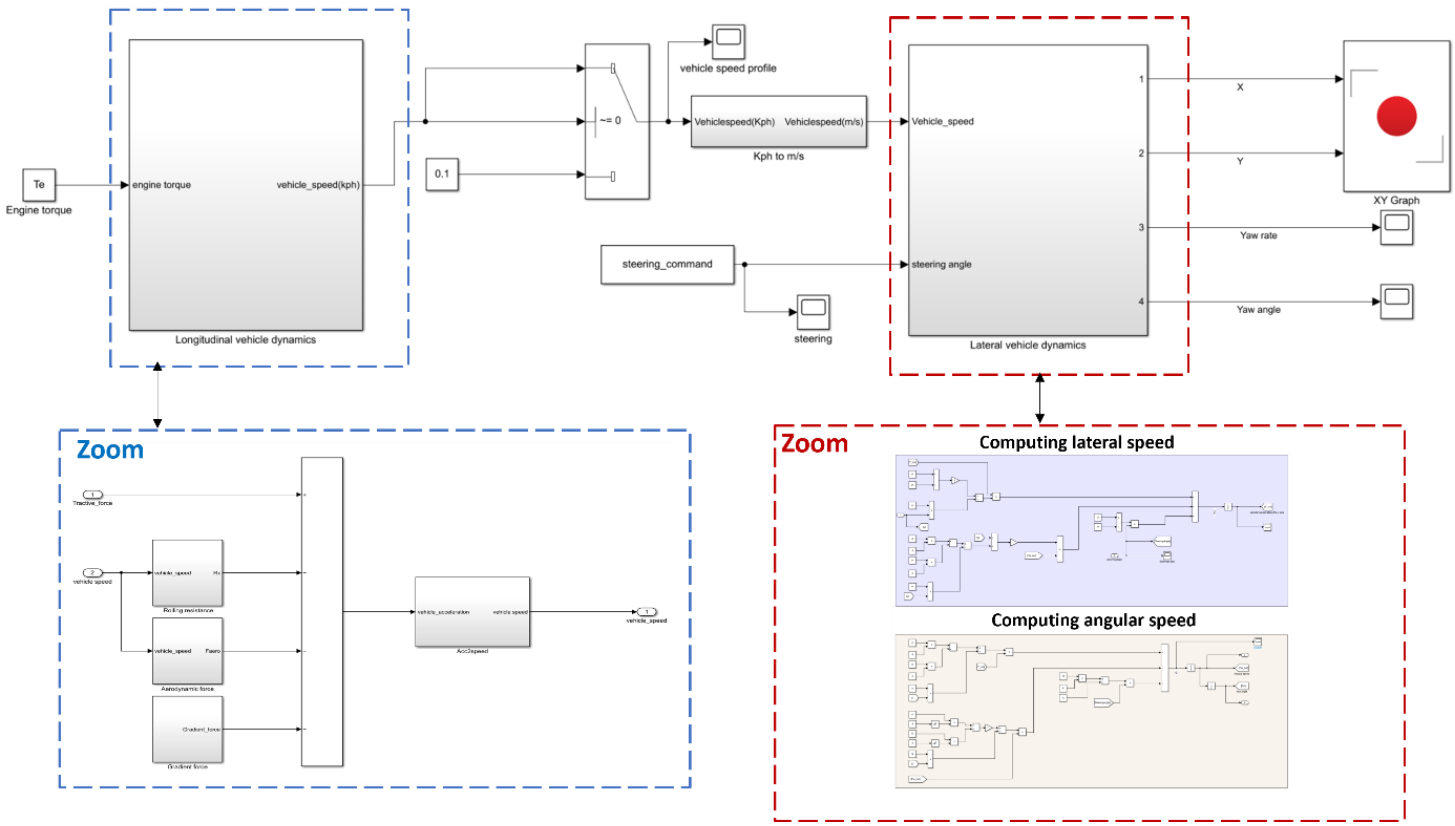

Figure 9. Detailed Simulink model for longitudinal and lateral dynamics.

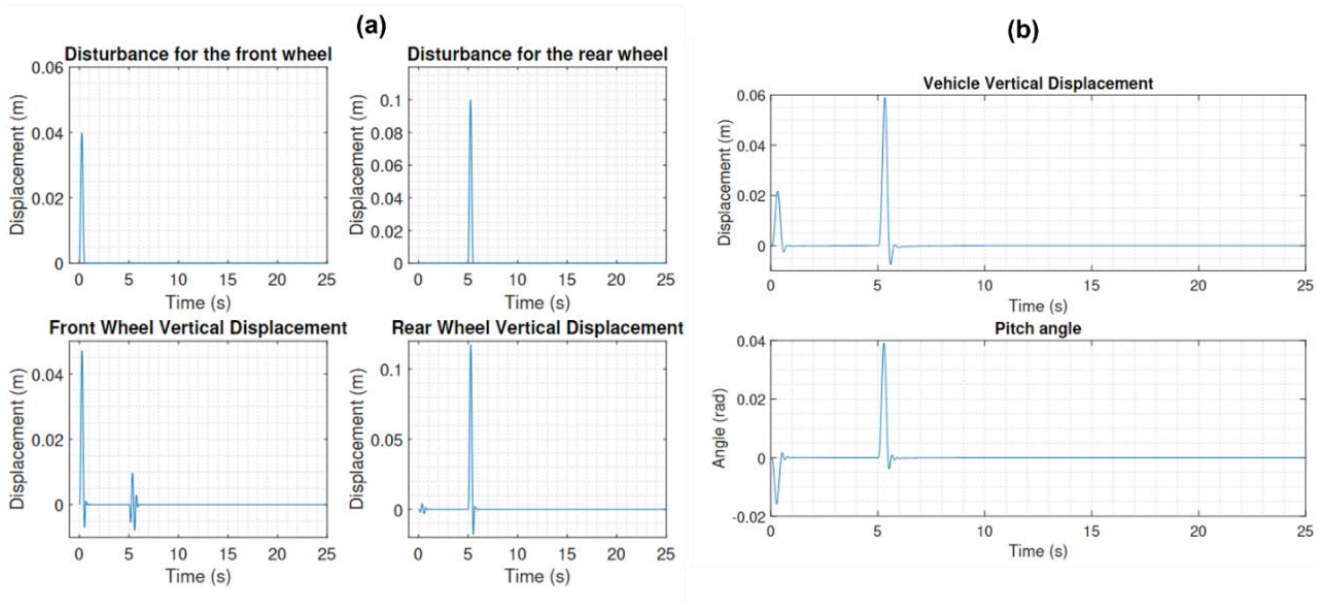

Figure 10. Half-car suspension model results.

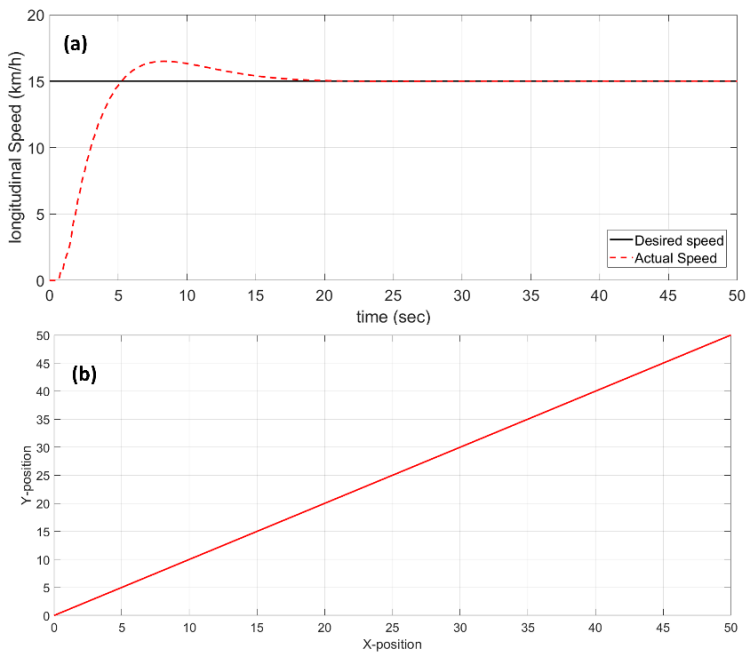

Figure 11. Longitudinal speed (a) and position of the vehicle (b) with a steering angle of zero.

5. Conclusions

In this paper, a mathematical model of vehicle dynamics is developed to describe a vehicle's motion in lateral, longitudinal and vertical directions. These dynamics models are vital for developing and validating algorithms for the vehicles. The models are implemented in MATLAB/Simulink and simulation are carried out with various input signals. The simulation results clearly validate the precision of the developed models, as they consistently mirror the expected vehicle motion. For instance, execution of motion by the vehicle in a straight line or in a circular pattern according to the longitudinal speed and steering angle inputs, the simulation outcomes align seamlessly with the anticipated behaviour. These results underscore the reliability and accuracy of the meticulously developed models, affirming their efficacy in capturing and replicating the dynamic responses of the vehicle in various scenarios. Moreover, a path tracking controller is also integrated to demonstrate the efficiency of the model and verify the accuracy of its derived parameters. Integrating a powertrain model with the vehicle dynamics is anticipated as a future work.

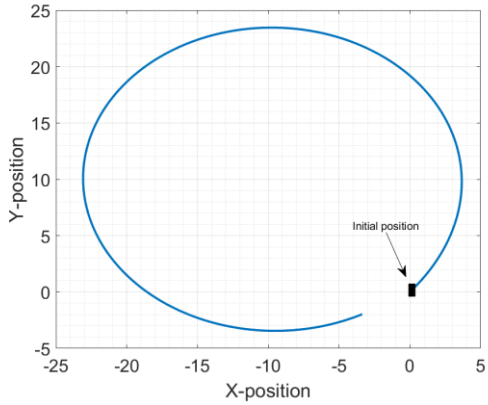

Figure 12. Position of the vehicle with a steering angle of $\boldsymbol{\pi/16}$.

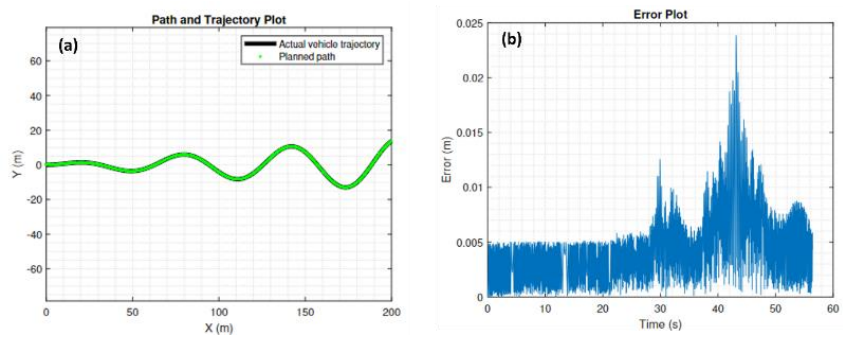

Figure 13. Vehicle motion control (a) path tracking (b) tracking error

Acknowledgment

This work was carried out at Altran Prototypes Automobiles (APA) as a part of the *Intelligence & Innovation Powertrain* project within the Capgemini Engineering Research and Innovation Department.

Conflict of Interest Statement

F.H, A.L and A.S. contributed equally. All authors have given approval to the final version of the manuscript. The authors declare that there is no conflict of interest in the study.

CRediT Author Statement

Fatima Haidar: Writing- review & editing, supervision, project administration & validation. **Abderaouf Laib:** Writing original draft & formal analysis. **Ajwad Syed Ali**: Writing-original draft, methodology, formal analysis, review & validation. **Guillaume Guilbert:** Conceptualization & Validation.

References

1. Hu, C., Wang, Z., Qin, Y., Huang, Y., Wang, J., & Wang, R. (2019). Lane keeping control of autonomous vehicles with prescribed performance considering the rollover prevention and input saturation. IEEE transactions on intelligent transportation systems, 21(7), 3091-3103.
2. Junejo, A. K., Xu, W., Mu, C., Ismail, M. M., & Liu, Y. (2020). Adaptive speed control of PMSM drive system based a new sliding-mode reaching law. IEEE Transactions on Power Electronics, 35(11), 12110-12121.
3. Hasenjäger, M., Heckmann, M., & Wersing, H. (2019). A survey of personalization for advanced driver assistance systems. IEEE Transactions on Intelligent Vehicles, 5(2), 335-344.
4. Zulhilmi, I. M., Peeie, M. H., Eiman, R. I. M., Izhar, I. M., & Asyraf, S. M. (2019). Investigation on vehicle dynamic behaviour during emergency braking at different speed. International Journal of Automotive and Mechanical Engineering, 16(1), 6161-6172.
5. Wada, M., Yoon, K. S., & Hashimoto, H. (2003). Development of advanced parking assistance system. IEEE Transactions on Industrial Electronics, 50(1), 4-17.
6. Liu, L., Lu, S., Zhong, R., Wu, B., Yao, Y., Zhang, Q., & Shi, W. (2020). Computing systems for autonomous driving: State of the art and challenges. IEEE Internet of Things Journal, 8(8), 6469-6486.
7. Yang, S., Lu, Y., & Li, S. (2013). An overview on vehicle dynamics. International Journal of Dynamics and Control, 1, 385-395.
8. Widner, A., Tihanyi, V., & Tettamanti, T. (2022). Framework for vehicle dynamics model validation. IEEE Access, 10, 35422-35436.
9. Farroni, F., Genovese, A., & Sakhnevych, A. (2022). Performance and safety enhancement strategies in vehicle dynamics and ground contact. Applied Sciences, 12(4), 2034.
10. Spiryagin, M., Edelmann, J., Klinger, F., & Cole, C. (2023). Vehicle system dynamics in digital twin studies in rail and road domains. Vehicle System Dynamics, 61(7), 1735-1784.
11. 13. Abe M. (2009) Vehicle Handling Dynamics: theory and application. Vehicle Handling Dynamics: Theory and Application: First Edition. Butterworth-Heinemann.
12. Remirez, C. A. (2015). Active Variable Geometry Suspension for Cars (Doctoral dissertation, Imperial College London).
13. Abe M. (2015) Vehicle Handling Dynamics: theory and application. Vehicle Handling Dynamics: Theory and Application: Second Edition. Butterworth-Heinemann.
14. Karaman, M., & Korucu, S. A. L. İ. H. (2023). Modeling the vehicle movement and braking effect of the hydrostatic regenerative braking system. Engineering Perspective, 3(2), 18-26.
15. Rajamani, R. (2011). Vehicle dynamics and control. Springer Science & Business Media.
16. Alp Arslan T, Aysal FE, Çelik İ, Bayrakçeken H, Öztürk TN. (2022) Quarter Car Active Suspension System Control Using Fuzzy Controller. Engineering Perspective. 4:33–9.
17. Karakaş, O., Şeker, U. B., & Solmaz, H. (2021). Modeling of an electric bus Using MATLAB/Simulink and determining cost saving for a realistic city bus line driving cycle. Engineering Perspective, 1(2), 52-62.
18. Fonseca, L., Olmeda, P., Novella, R., & Valle, R. M. (2020). Internal combustion engine heat transfer and wall temperature modeling: an overview. Archives of Computational Methods in Engineering, 27(5), 1661-1679.
19. Setiawan, Y. D., Roozegar, M., Zou, T., & Angeles, J. (2017). A mathematical model of multispeed transmissions in electric vehicles in the presence of gear shifting. IEEE Transactions on Vehicular Technology, 67(1), 397-408.
20. Min, H., Wu, X., Cheng, C., & Zhao, X. (2019). Kinematic and dynamic vehicle model-assisted global positioning method for autonomous vehicles with low-cost GPS/camera/in-vehicle sensors. Sensors, 19(24), 5430.
21. Da Silva, E. S., Kram, R., & Hoogkamer, W. (2022). The metabolic cost of emulated aerodynamic drag forces in marathon running. Journal of Applied Physiology, 133(3), 766-776.

22. Josee, M., Kazima, S., & Turabimana, P. (2021). Review of semi-active suspension based on Magneto-rheological damper. Engineering Perspective, 2(2), 38-51.
23. Samuel, M., Maziah, M., Hussien, M., & Godi, N. Y. (2018). Control of autonomous vehicle using path tracking: A review. Advanced Science Letters, 24(6), 3877-3879.
24. Samuel, M., Hussein, M., & Mohamad, M. B. (2016). A review of some pure-pursuit based path tracking techniques for control of autonomous vehicle. International Journal of Computer Applications, 135(1), 35-38.

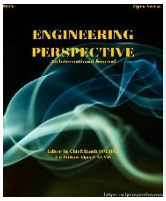

e-ISSN:2757-9077

ENGINEERING PERSPECTIVE

https://sciperspective.com/ Research Paper

Stress-Strain Deformation Analysis of Conventional Vehicle Shock Absorber Materials Under In-Service Multi-Translated Non-Proportional Loading Conditions

Aniekan Essienubong Ikpe[1*], Imoh Ime Ekanem[2]

[1, 2]*Department of Mechanical Engineering Technology, Akwa Ibom State Polytechnic, Ikot Osurua, PMB 1200, Nigeria*

ABSTRACT

The in-service condition of a vehicle eventually subject the shock absorber to unforeseen deformations due to external forces such as damping, friction, resistance forces and other factors such as poor road condition characterized by potholes and speed bumps. In this study, a vehicle shock absorber was analysed, considering the in-service condition. Using SOLIDWORKS software, 2020 version the shock absorber component was modelled with three different materials which were simulated with ANSYS software. From the simulated results, maximum total deformations of 54.286, 49.26 and 47.603 mm as well as maximum directional deformations of 53.303, 48.762 and 47.569 mm were obtained for hard drawn spring wire (A227), alloy steel (A213) and stainless steel (A313) selected as the shock absorber materials. On the other hand, maximum equivalent von-mises stresses of 1205.8, 1204.7 and 1084.6 MPa as well as maximum equivalent strain values of 0.0065269, 0.0061912, 0.0060882. From the simulated results obtained, stainless steel (A313) out of the three shock absorber material exhibited the least deformations, von-mises stress and equivalent strain. However, the three materials had satisfy the failure distortion-energy theory, and may be feasible for shock absorber application in actual scenario because the Von-mises stress obtained had not exceeded any of the material's yield strength. This was evidence in the low equivalent strain values and the colour distribution across the shock absorber models which was dominated by royal blue colour, indicating that the shock absorber models can still accommodate multiple translated non-proportional loading or still had significant load bearing capacity. The stress-strain deformation analysis in this study can help predict and prevent premature failure, ensuring the longevity of vehicle shock absorbers.

Keywords: Deformations, External forces, Loading conditions, Materials, Shock absorber

History
Received: 18.10.2023
Accepted: 13.02.2024

Author Contacts
**Corresponding Author*
e-mail addresses : aniekan.ikpe@akwaibompoly.edu.ng, imoh.ekanem@akwaibompoly.edu.ng

How to cite this paper: Ikpe, A.E., Ekanem I.I., (2024). Stress-Strain Deformation Analysis of Conventional Vehicle Shock Absorber Materials Under In-Service Multi-Translated Non-Proportional Loading Conditions. Engineering Perspective, 4(1), 17-31. http://dx.doi.org/10.29228/eng.pers.74770

1. Introduction

The automotive industry is constantly evolving, with manufacturers striving to enhance vehicle performance, safety, and comfort. One critical component that plays a significant role in achieving these objectives is the shock absorber. The shock absorber is responsible for dampening the vibrations and impacts experienced by a vehicle, ensuring a smooth and controlled ride [1, 2]. Their primary function is to dampen the oscillations and vibrations caused by uneven road surfaces, bumps, and other disturbances. By absorbing and dissipating the kinetic energy generated during these movements, shock absorbers help maintain tire contact with the road, ensuring better traction and handling [3, 4]. These components are subjected to various loads and forces including compression, extension, and torsion during operation, which can significantly result in deformation failure, thereby, affecting their performance and longevity [5, 6]. In other words, these forces can cause significant stress and strain on the shock absorber components, leading to potential failure. Analysing the stress-strain deformation helps in understanding the behaviour of these components under different operating conditions. Over the years, failure deformations, stress-strain deformation characteristics, continuous improvement and optimization of shock absorbers have evolved through various academic research cited in this study.

The dynamic behaviour of a vehicle shock absorber system was investigated by Sani et al. [7]. An interchangeable shock absorber

test rig integrated with computer systems was designed and fabricated to record the signals. An experiment was conducted to identify the stiffness and damping parameter for 850 cc and 1600 cc shock absorber. The stiffness and damping conditions were simulated using COSMOS Motion software. Findings obtained indicated discrepancy of 10%. Optimum range of stiffness for the shock absorber was between 20 N/mm and 60 N/mm while optimum damping range was between 1 Ns/mm and 6 Ns/mm.

Zhang [8] studied a vehicle regenerative shock absorber by developing a 2 degrees of freedom oscillating system resembling the quarter vehicle suspension system with electromagnetic harvester and validated the model using ANSYS Maxwell software simulation. The peak power output was observed to occur at a natural frequency. A novel indirect drive regenerative shock absorber with the arm-teeth system was also modelled and fabricated. Findings obtained revealed that power output can be increased compared to the traditional direct drive regenerative shock absorber. A full vehicle suspension system model was also modelled as an extension of the half vehicle suspension system. It was observed that at high frequency range, the peak power output ratio of full vehicle suspension system was the same with the half and quarter vehicle suspension system.

Natural frequencies of the shock absorber in a 2 degree-of-freedom system were investigated by Tan et al. [9] using Wolfram Mathematica 11, CATIA, and ANSYS. Both theoretical and simulation were employed in the study to determine the resonance effects on the vehicle shock absorber. Failure was found to occur on coil spring of the shock absorber earlier before proceeding to the body of the shock absorber. Two natural frequencies had been obtained as 1.0 Hz and 9.1 Hz for sprung mass and un-sprung mass which where the frequencies that acceleration was recorded as maximum.

SelvaKumar et al. [10] modelled a vehicle shock absorber system with CATIA software and analysed the same model using ANSYS software. The analysis was to determine the equivalent stresses and principal elastic strains on the shock absorber system using two engineering materials including carbon fibre and beryllium copper. Using different diameters of 10.9, 11.2, 11.4, 11.6, 11.8, maximum equivalent stress and principal elastic strain of 3.2768e5, 5.2883e5, 4.7892e5, 4.5751e5 and 4.328e5 as well as 6.9334e-5, 0.00010763, 9.794e-5, 9.4869e-5 and 8.7578e-5 were obtained for carbon fibre. However, using the same diameter for beryllium copper, maximum stress and strain of 3.2709e5, 5.3297e5, 4.8135e5, 4.584e5 and 4.3532e5 as well as 2.7096e-6, 4.2369e-6, 3.8459e-6, 3.7097e-6 and 3.4421e-6 were obtained.

A 3D model of a vehicle suspension system was developed by Bhasha et al. [11] using CATIA V5 R21. Structural analysis and modal analysis was carried out on the shock absorber system using different materials. The materials were titanium alloy, phosphor bronze, beryllium copper, and spring steel, and maximum stress intensity of 36.102, 36.5865, 36.4637 and 36.4265 N/mm^2 were obtained while maximum displacements vectors of 2.6326, 4.9247, 4.8582 and 3.0123 mm were obtained. It was observed that the stress intensity and displacement vectors were less for titanium alloy than other materials.

The stress-strain deformation analysis of vehicle shock absorber models is essential for several reasons. Firstly, it allows engineers and researchers to evaluate the structural integrity and durability of shock absorbers under various loading conditions [12, 13]. By subjecting shock absorber models to different stress levels, it becomes possible to identify potential failure points and design flaws, thereby improving their overall performance and reliability. Secondly, understanding the stress-strain deformation behaviour of shock absorber models aids in optimizing their design and material selection [14]. By analysing the stress distribution and strain patterns, engineers can identify areas of high stress concentration and modify the design accordingly. This optimization process ensures that shock absorbers can withstand the forces they encounter during vehicle operation, leading to improved safety and longevity.

Furthermore, stress-strain deformation analysis provides valuable insights into the performance characteristics of shock absorbers. By simulating real-world conditions, researchers can evaluate the damping capabilities of different shock absorber models. This information is crucial for selecting the most suitable shock absorber for specific vehicle applications, ensuring optimal ride comfort and stability [15]. Moreover, stress-strain deformation analysis can aid in the development of advanced shock absorber technologies. By studying the behaviour of shock absorber models under extreme conditions, such as high-speed impacts or off-road terrain, engineers can identify opportunities for innovation. This study can lead to the development of shock absorbers with enhanced performance, such as adjustable damping systems or adaptive control mechanisms.

Stress-strain deformation analysis on vehicle shock absorber models is a critical aspect of understanding their behaviour and performance. By evaluating the structural integrity, optimizing the design, and assessing the damping capabilities, the safety, comfort, and durability of shock absorbers can be enhanced. The evaluation was adopted in this study for stress-strain deformation analysis of conventional vehicle shock absorber materials under in-service multi-translated non-proportional loading conditions. This can provide a foundation for the development of advanced shock absorber technologies, contributing to the continuous improvement of vehicle suspension systems. Therefore, stress-strain deformation analysis carried out in this study is crucial for understanding the behaviour of vehicle shock absorbers under different operating conditions. By identifying potential problems, material limitations, and areas of high stress concentration, engineers can optimize the design, enhance performance, and ensure the reliability and longevity of shock absorbers. This analysis also aids in validating the design and manufacturing processes, leading to improved overall vehicle dynamics and customer satisfaction.

2. Research Methodology

2.1 Theoretical Background

In static structural deformation analysis, mathematical equations are used to calculate total and directional deformations, as well as equivalent Von-Mises and elastic strain. These equations are derived based on principles of mechanics and material behaviour, and are essential for understanding the behaviour of shock absorbers under applied loads. To calculate directional deformations, the material's properties and the direction of the applied load were considered. To obtain mathematical equations for total and directional deformations on vehicle shock absorber system, the basic principles of elasticity was considered. In addition to deformations, it is also important to

calculate the equivalent Von-Mises stress and elastic strain. These calculations are essential for predicting the performance and failure of structures and components. These equations form the underlying principles behind the operation of vehicle shock absorbers, and are essential for analysing their behaviour under applied loads and ensuring their safety and reliability. Shock absorbers operate based on the principle of converting kinetic energy into heat energy. They consist of a piston, cylinder, and hydraulic fluid. When a vehicle encounters a bump or uneven surface, the suspension system compresses the shock absorber [16]. This compression forces the piston to move inside the cylinder, displacing the hydraulic fluid. The hydraulic fluid, usually oil, flows through small orifices or valves within the shock absorber, creating resistance against the piston's movement. This resistance slows down the compression and extension of the suspension system, controlling the rate at which the vehicle's weight shifts during these movements. The damping force generated by the shock absorber is determined by various factors, including the design, size, and viscosity of the hydraulic fluid, as well as the orifice size and valve characteristics. If these components are not carefully engineer, it becomes difficult to achieve the desired damping characteristics for different vehicle types and driving conditions. Performance efficiency of the shock in the vehicle's suspension must be evaluated by taking into account the vibrating system being a linear single-mass single-support mechanism with fixed elastic and damping characteristics at a harmonic frequency as seen on Figure 1.

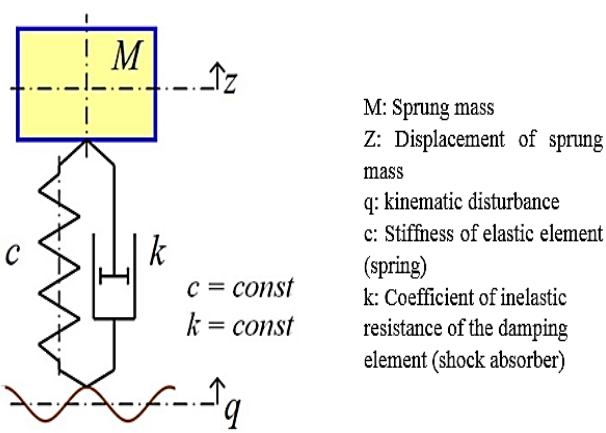

Figure 1. Linear vibrating system with damping characteristics

The linear vibrating system is based on the following differential equation presented in Eq.(1) and Eq. (2):

$$M\dot{z} + k\ (\dot{z} - \dot{q}) + c(z - q) = 0 \tag{1}$$

or

$$\dot{z} + 2h\ (\dot{z} - \dot{q}) + \omega_0^2\ (z - q) = 0 \tag{2}$$

To compute the absolute and relative oscillations, it is important to rewrite Eq. (2) in the following forms:

$$\dot{z} + 2h\dot{z} + \omega_0^2\ z = 2h\dot{q} + \omega_0^2\ q = Q_Z \tag{3}$$

$$\dot{x} + 2h\dot{x} + \omega_0^2\ x = \dot{q} = Q_x \tag{4}$$

prepared Where $x = q - z$ is the suspension deformation, $\dot{x} = \dot{q} - \dot{z}$ represents velocity of suspension deformation, $\ddot{x} = \dot{q} - \dot{z}$ is the suspension deformation due to acceleration, $\dot{q}$ denotes disturbing kinematic effect, Q_x and Q_Z denotes disturbing functions for steady state forced oscillations on x and z coordinates. Eqs.(5-9) was obtained based on the principles of linear vibrating system, in which the damping effect of the suspension system induces stress-strain deformations on the shock absorber. In this case, the amplitude of perturbing function causing forced absolute oscillations of the sprung mass is given by Eq. (5).

$$Q_{Z0} = q_0\sqrt{\omega_0^4 + 4h^2\omega_0^2} \tag{5}$$

The amplitude of perturbing function causing forced relative oscillations of the sprung mass is given by Eq. (6).

$$Q_{X0} = \ q_0\omega^2 \tag{6}$$

In cases where resistance force versus deformation velocity is linear, the total work on the shock absorber over oscillation cycle is given by Eq. (7):

$$A = \frac{2\pi}{\int_0^W k\dot{x}x\dot{d}t} = kx_0^2\omega\pi \tag{7}$$

Where $\dot{x} = x_0\ \ \omega\cos(\omega t + \beta_x)$ represents deformation velocity of vehicle suspension. Suspension force acting partially on the linear shock absorber over oscillation cycle is expressed in Eq. (8).

$$P_f = \frac{\frac{\left(\frac{\pi}{2}\beta_x\right)}{\omega}}{2\int k\dot{x}\dot{x}dt = kx_0^2\omega(sin\beta * cos\beta - \beta),\ \ \frac{\left(\frac{\pi}{2}\beta z\right)}{\omega}} \tag{8}$$

Suspension force acting fully on the linear shock absorber system over oscillation cycle is expressed in Eq. (9).

$$F_f = f - P_f = kx_0^2\omega\pi - kx_0^2\omega\ \ (sin\beta * cos\beta - \beta) = kx_0^2\omega\ \ (\pi + \beta - sin\beta * cos\beta) \tag{9}$$

Thus, Effective Work Ratio (EWR) of the shock absorber with linear characteristic can be determined using Eq. (10).

$$\eta = \frac{P_f}{f} = \frac{kx_0^2\omega\ \ (\pi + \beta - sin\beta * cos\beta)}{kx_0^2\omega\pi} = \frac{\pi + \beta - sin\beta * cos\beta}{\pi} \tag{10}$$

Under isothermal conditions, the pressure variations in the rebound chamber and the compression chamber are expressed in Eq. (11) and Eq. (12).

$$\frac{dp_1}{dt} = \frac{E}{V_{10} + S_1x_1}\left((Q_1 + Q_2 + Q_3 + Q_4) - (S_1\dot{x}_1)\right) \tag{11}$$

$$\frac{dp_2}{dt} = \frac{E}{V_{20}+S_3x_2-S_2x_1}\begin{pmatrix}(Q_1 - Q_2 - Q_3 - Q_4) \\ -(S_3\dot{x}_2 - S_2\dot{x}_1)\end{pmatrix} \quad (12)$$

where E is Oil Bulk modulus, V_{10} and V_{20} are the initial volumes of the rebound and compression chambers, Q is the oil flow rate of corresponding orifices, S_i is the cross-section area of the relevant chamber, $\dot{x}_1$ is the velocity of the main piston, $\dot{x}_2$ is the velocity of floating piston, x_1 is the displacement of the main piston, x_2 is the displacement of the floating piston. The opened area for variable orifice with a blunt needle for oil flow during compression and rebound strokes is given by Eq. (11).

$$A_3 = \frac{\pi}{4}d_b^2\left(1 - \left(1 - \frac{\eta_c}{2M_c}\right)^2\right) \quad (13)$$

where d_b is the diameter of the additional orifice, n_c is the click number of the variable diameter needle, M_c is the maximum possible number of the needle clicks. For total forces on the floating piston, the equation of motion for the floating piston is given by Eq. (14). In addition, equation of motion for the main piston is given by Eq. (13).

$$m_2\ddot{x}_2 = S_3P_2 - S_3P_3 - F_f 2\ sign(\dot{x}_2 - \dot{x}_1) - m_2 g \quad (14)$$

$$m_1\ddot{x}_1 = S_1P_1 - S_2P_2 - F_f 1\ sign(\dot{x}_1) - m_1 g + F \quad (15)$$

where m_1 is the mass of the main piston, x_1 is the acceleration of the piston motion, S_1 is the area of the rebound chamber cross section, S_2 is the area of the compression chamber cross-section, F_f1 is the friction force appearing between the piston and the body of the shock absorber, and F is the damping force caused by the shock absorber. The damping force caused by the shock absorber due to its motion is expressed in Eq. (16).

$$F = m_1\ddot{x}_1 - S_1P_1 + S_2P_2 + F_f 1\ sign(\ddot{x}_1) + m_1 g \quad (16)$$

2.2 Analytical Background

The shock absorber assembly is presented in Figure 2. The CAD model was done on SolidWorks 2018 while all analysis was done on ANSYS 2023 R1. The CAD model was imported to ANSYS workbench for Finite Element Analysis (FEA). The Finite Element method was used to study the maximum shear stress, the Von-mises stress and the displacement due to the force. The model was simplified for to enable us obtain quality meshing and reduce the analysis time and computational resources required. It can be observed that the spring base support was rid of any complex curves. Furthermore, the contact between the rod and the cylinder was ignored and the model was adjusted to ignore such contact. This is because we are only interested in the spring's behaviour under load and not the entire strut assembly. The other parts were assigned the default structural steel material found in the applications database.

The procedure for geometry and mesh generation in FEA plays a critical role in obtaining accurate and reliable analysis results. It involved creating an accurate geometric model, simplifying the geometry, generating a suitable mesh, selecting appropriate element types and sizes, defining boundary conditions, and performing a quality check. Following this procedure ensures that the FEA analysis is based on a sound foundation, leading to more accurate predictions and better engineering decisions. Step-by-step procedure for conducting FE simulation of shock absorber model in this study are enumerated as follows:

i. Geometry Generation: The first step in Finite Element (FE) modelling process was to create a geometric CAD model of the shock absorbing structure or component being analysed. This was done using computer-aided design (CAD) software known as SOLIDWORKS. The geometry included all relevant components, such as the piston, cylinder, coil spring and strut mount.
ii. Clean-up and Simplification: Once the CAD geometry was created, it was important to clean-up and simplify the model. Some unnecessary details, such as small fillets or chamfers were removed, and the geometry was simplified to reduce the computational effort required for mesh generation and analysis.
iii. Mesh Generation: Once the geometry was created, clean-up and simplification done, a mesh was generated to discretize the model into smaller elements. The mesh generation process involved division of the geometry into a finite number of smaller, interconnection of 8 nodded tetrahedral brick element. The mesh was fine enough to capture the important features of the shock absorber geometry and ensure accurate results with less computational time. The selection of element size depends on the complexity of the geometry and the desired level of accuracy. Smaller elements provide more accurate results but require more computational resources.
iv. Material Properties: Accurate material properties are essential for realistic simulations. The material properties of the shock absorber components, such as the piston, cylinder, coil spring and strut mount, needed to be determined. In the outline window on the ANSYS material library, the Geometry tab was expanded while the Solid Body 1 was highlighted. The shock absorber model was then highlighted in green, indicating it is selected. Right below the outline window was "Details of Solid Body 1". The material was expanded, the material properties desired or defined for the model was then assigned to the shock absorber model.
v. Boundary Conditions and Constraints: Boundary conditions and constraints which defined constraints and loading conditions applied to the shock absorber model were specified. These included fixed supports, applied loads, damping and stiffness coefficients and constraints on displacements or rotations. Boundary condition represented the physical connection between the shock absorber and the structure it is mounted on. The fixed constraints were applied to simulate the mounting points of shock absorbers. These constraints restricted the translational and rotational degrees of freedom, ensuring that the shock absorber remained fixed at its mounting locations. Shock absorbers are subjected to various loads during their operation, such as compression, extension, and torsion. For example, a compressive load can be applied to simulate the impact of

a vehicle hitting a bump. In this case, a load of 4300N representing the cars sprung weight and luggage loads was applied in the positive y direction. This force was constrained to simulate the forces on an actual shock absorber. A fixed support was placed on a strut mount. The magnitude, direction, and distribution of these loads were properly represented in order to obtain reliable results. Shock absorbers are designed to provide damping and stiffness to control the motion of a system. These characteristics were incorporated into the FE model by defining appropriate damping and stiffness coefficients.

vi. Quality Check: After generating the mesh, it was important to perform a quality check to ensure the mesh is suitable for analysis, as mesh quality directly affects the accuracy of the analysis results. This involved checking for element distortion, aspect ratio, and element size variation. Mesh quality directly affects the accuracy of the analysis results. Errors found were adequately addressed before proceeding with the FEA analysis.

vii. Finite Element Analysis: Once the geometry, mesh, material properties, and boundary conditions were defined, a finite element analysis (FEA) was performed using the ANSYS software. This involved solving the governing equations of motion using numerical methods. The ANSYS software calculated the total deformation, directional deformation, equivalent Von-mises stresses and equivalent strain, of the shock absorber model. The accuracy of the results depended on the quality of the mesh, material properties, and boundary conditions.

Internal damping and viscous parameters were not considered because the study was static structural deformation analysis. Static structural deformation analysis focuses on the equilibrium state of a structure under applied loads, where the structure is assumed to be in a state of rest. In this scenario, the effects of internal damping and viscous parameters, which are related to dynamic behaviour and energy dissipation of the shock absorber, are not relevant. Internal damping and viscous parameters are typically considered in dynamic structural analysis, where the response of a structure to time-varying loads is of interest. In dynamic analysis, the damping characteristics of a structure play a crucial role in determining its response to dynamic loads, such as vibrations or seismic forces. However, in static analysis, where the focus is on determining the static deformation and stresses on the sock absorber, the consideration of internal damping and viscous parameters is unnecessary. Furthermore, the inclusion of internal damping and viscous parameters in static structural deformation analysis can complicate the analysis and introduce additional uncertainties. These parameters are often difficult to quantify accurately and can vary significantly depending on the material properties, geometry, and boundary conditions of the structure. By neglecting these parameters in static analysis, the analysis becomes more straightforward and the results are more reliable.

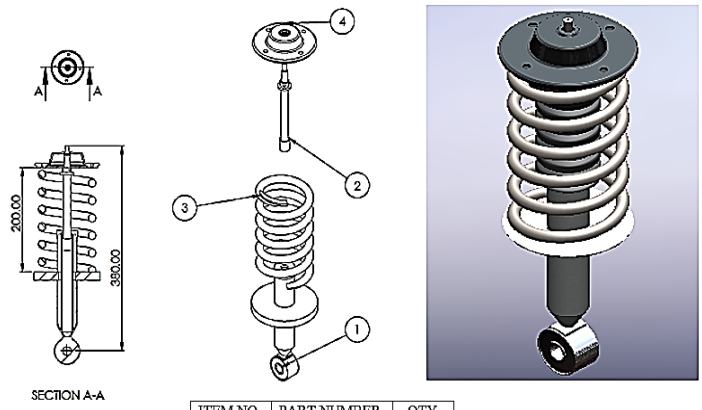

ITEM NO.	PART NUMBER	QTY.
1.	Cylinder	1
2.	Piston Rod	1
3.	Coil Spring	1
4.	Strut Mount	1

Figure 2. Shock absorber assembly

The shock absorber was modelled in SolidWorks 2020. The material properties were selected from conventional spring materials, with design parameters adequately considered. The wire diameter (d), spring diameter and spring height were 15.5 mm, 155.57 mm and 200 mm. The computational analysis was carried in ANSYS 2023 R1. Mesh visualization of the shock absorber model is shown in Figure 3 while the properties of shock absorber materials are presented in Table 1. Modelling details of the shock absorber components are presented in Table 2 while mesh details of the shock absorber model are presented in Table 3.

Table 1. Properties of shock absorber materials

Material Properties	Hard Drawn Spring Wire (A227)	Stainless Steel (A313)	Alloy Steel (A213)
Young's Modulus (MPa)	2.07e+05	1.9305e+05	2.0684e+05
Poisson's Ratio	0.3	0.4	0.30435
Bulk Modulus (MPa)	1.725e+05	3.2176e+05	1.762e+05
Shear Modulus (MPa)	79615	68948	79290
Tensile Yield Strength (MPa)	1591	2240.8	2068.4

In finite element simulations, contact conditions are typically defined using contact algorithms that determine how two surfaces interact when in contact with each other. These algorithms consider factors such as friction, penetration, and separation between the surfaces to accurately model the contact behaviour. For shock absorbers, contact conditions are particularly important as they directly affect the static behaviour and overall performance of the system.

Table 2. Modelling details of the shock absorber components

Shock Absorber Components	Strut Mount	Coil Spring	Piston Rod	Cylinder
Material				
Assignment	Structural Steel	Stainless Steel		Structural Steel
Nonlinear Effects	Yes			
Thermal Strain Effects	Yes			
Bounding Box				
Length X	176.69 mm	122.7 mm	33.803 mm	120. mm
Length Y	29. mm	175.54 mm	200. mm	255. mm
Length Z	176.69 mm	122.7 mm	33.803 mm	120. mm
Properties				
Volume	68533 mm³	2.4589e+005 mm³	27752 mm³	1.5043e+005 mm³
Mass	0.53798 kg	1.9057 kg	0.21507 kg	1.1809 kg
Centroid X	8.8548e-005 mm	6.2259e-002 mm	-4.495e-009 mm	-1.7033e-005 mm
Centroid Y	412.53 mm	319.08 mm	335.22 mm	176.13 mm
Centroid Z	5.6181e-005 mm	0.62281 mm	2.2488e-009 mm	7.2457e-003 mm
Moment of Inertia Ip1	610.93 kg·mm²	7025.3 kg·mm²	6.4163 kg·mm²	7790.7 kg·mm²
Moment of Inertia Ip2	1174.2 kg·mm²	4647.7 kg·mm²	763.84 kg·mm²	554.03 kg·mm²
Moment of Inertia Ip3	610.94 kg·mm²	7016. kg·mm²	763.86 kg·mm²	7830.8 kg·mm²
Statistics				
Nodes	21091	13616	18958	43137
Elements	11115	6549	12322	23032

Table 3. Mesh details of the shock absorber model

Object Name	Mesh	Object Name	Mesh
State	Solved	Quality	
Display		Check Mesh Quality	Mesh Quality Worksheet
Display Style	Use Geometry Setting	Error Limits	Aggressive Mechanical
Defaults		Target Element Quality	5.e-002
Physics Preference	Mechanical	Smoothing	Medium
Element Order	Program Controlled	Mesh Metric	None
Element Size	8.0 mm	Inflation	
Sizing		Use Automatic Inflation	None
Use Adaptive Sizing	Yes	Inflation Option	Smooth Transition
Resolution	Default (2)	Transition Ratio	0.272
Mesh Defeaturing	Yes	Maximum Layers	5
Defeature Size	Default	Growth Rate	1.2
Transition	Slow	Inflation Algorithm	Pre
Span Angle Center	Coarse	View Advanced Options	No
Initial Size Seed	Assembly	Advanced	
Bounding Box Diagonal	462.39 mm	Number of CPUs for Parallel Part Meshing	Program Controlled
Average Surface Area	1799.4 mm²	Straight Sided Elements	No
Minimum Edge Length	1.0472 mm	Rigid Body Behavior	Dimensionally Reduced
Statistics		Triangle Surface Mesher	Program Controlled
Nodes	96802	Topology Checking	Yes
Elements	53018	Pinch Tolerance	Please Define
Show Detailed Statistics	No	Generate Pinch on Refresh	No

In the context of SOLIDWORKS Simulation, defining contact conditions involves specifying how different components interact with each other under loading conditions. This is essential for predicting the performance and durability of the shock absorber assembly. One of the key challenges in defining contact conditions is determining the type of contact between components. There are various types of contact conditions that can be defined in SOLIDWORKS Simulation, including bonded, no penetration, and frictional contact. Each type of contact condition has its own set of parameters that need to be carefully defined to accurately represent the physical behaviour of the components. Defining contact conditions for shock absorbers in SOLIDWORKS Simulation, factors such as material properties, surface roughness, and loading conditions were considered. For example, the coefficient of friction between the piston and cylinder surfaces can have a significant impact on the damping characteristics of the shock absorber.

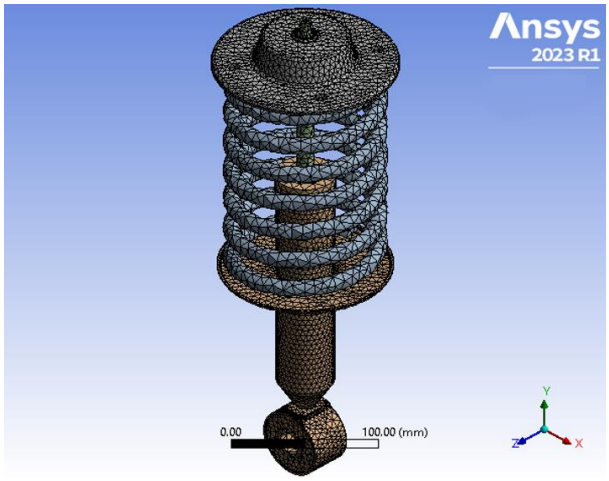

Figure 3. Mesh visualization of the shock absorber model

While analysing the shock absorber system in this study, the following contact conditions were defined:

i. Bonded contact assumed that the two components are perfectly joined together and do not move relative to each other. This was considered suitable for components that are rigidly connected, such as the spring and its seat or piston and cylinder of the shock absorber.
ii. No penetration contact allowed components to move relative to each other, but prevents them from interpenetrating. This was considered useful for simulating the movement of components within a shock absorber, such as the piston sliding within the cylinder.
iii. Frictional contact introduced a frictional force between components, which can be useful for simulating the damping effect of the shock absorber. By adjusting the friction coefficient, the behaviour of the shock absorber under different conditions can be modelled accurately.

One common approach that was used in defining contact conditions in shock absorber simulations in this study was the use of contact elements. These elements are inserted at the interface between the contacting surfaces and allow for more accurate modelling of the contact behaviour. Contact elements can account for factors such as friction, separation, and sliding between the surfaces, providing a more realistic representation of the contact conditions. Boundary conditions (connections and contacts as well as coordinate systems) for the shock absorber stress-strain deformation analysis are presented in Table 4.

Table 4. Boundary conditions for the shock absorber stress-strain deformation analysis

CONNECTIONS AND CONTACTS		COORDINATE SYSTEM	
Object Name	Contacts	Object Name	Global Coordinate System
State	Fully Defined	State	Fully Defined
Definition		Definition	
Connection Type	Contact	Type	Cartesian
Scope		Coordinate System ID	0
Scoping Method	Geometry Selection	Origin	
Geometry	All Bodies	Origin X	0. mm
Auto Detection		Origin Y	0. mm
Tolerance Type	Slider	Origin Z	0. mm
Tolerance Slider	0.	Directional Vectors	
Tolerance Value	1.156 mm	X Axis Data	[1. 0. 0.]
Use Range	No	Y Axis Data	[0. 1. 0.]
Face/Face	Yes	Z Axis Data	[0. 0. 1.]
Face-Face Angle Tolerance	75°	Analysis	
Statistics		Physics Type	Structural
Connections	4	Analysis Type	Static Structural
Active Connections	4	Solver Target	Mechanical APDL

2.3 Background Details on SOLIDWORKS and ANSYS Simulation Software

In the field of engineering, simulation software plays a crucial role in the design and analysis of various products and systems. Two widely used simulation software programs are SOLIDWORKS and ANSYS. Both programs offer powerful tools for engineers to simulate and analyse the behaviour of their designs before they are physically built. The background details of SOLIDWORKS and ANSYS simulation software, and their key features and capabilities are provided as follows:

i. SOLIDWORKS: SOLIDWORKS is a 3D CAD and modelling tool developed by Dassault Systèmes to run on Microsoft Windows. It is widely used in the engineering industry for designing and modelling mechanical components and assemblies [17]. SOLIDWORKS offers a user-friendly interface that allows engineers to create complex 3D models with ease. The software also provides a wide range of tools for simulation and analysis, including finite element analysis (FEA) and computational fluid dynamics (CFD). One of the key features of SOLIDWORKS is its integration with other software programs, such as ANSYS, for more advanced simulation capabilities. This allows engineers to transfer their designs seamlessly between the two programs, enabling them to perform detailed analysis and optimization of their models.
ii. ANSYS: ANSYS is a simulation software developed by

ANSYS Inc. It is known for its advanced capabilities in structural analysis, fluid dynamics, and electromagnetics. ANSYS offers a wide range of tools for engineers to simulate and analyse the behaviour of their designs under various conditions. One of the key features of ANSYS is its ability to perform Multiphysics simulations, where multiple physical phenomena are simulated simultaneously. This allows engineers to study the interactions between different aspects of their designs, leading to more accurate and realistic results.

Both SOLIDWORKS and ANSYS simulation software programs offer unique features and capabilities for engineers to design and analyse their products. While SOLIDWORKS is more focused on 3D modelling and design, ANSYS is known for its advanced simulation capabilities. By integrating these two programs, engineers can take advantage of the strengths of each software to create more efficient and optimized designs. Also, being adequately versed on the background details of these software programs, can enable engineers make informed decisions on which program to use for their specific needs.

3. Results and Discussions

Total deformation refers to the overall change in shape or dimensions of the shock absorber due to external forces such as damping, friction, resistance forces etc. A number of deformations (bending, twisting, compression, and elongation) due to these operating forces acting on the shock absorber results in total deformation of the system. Deformation can occur in various components of the shock absorber, such as the piston rod, cylinder, and mounting brackets. Various factors contribute to the total deformation experienced by shock absorbers, including vehicle weight, road conditions, and driving style. Poor road conditions, such as potholes and speed bumps, can subject shock absorbers to higher levels of deformation. Aggressive driving, such as hard braking and cornering, can increase the forces acting on the shock absorbers, leading to greater deformation.

Figures 4-6 illustrates total deformation profiles for three (3) conventional shock absorber materials including Hard Drawn Spring Wire (A227), Stainless Steel (A313) and Alloy Steel (A213). The total deformation profile in Figures 4-6 are characterised by several colours such as royal blue, sky blue, lemon, yellow and red colours, each representing minimum and maximum total deformation safe values or critical values. These values indicate that the shock absorber material may fail depending on the severity of deformations involved. Therefore, royal blue colour represents the minimum total deformation values, red colour represents maximum total deformation values. However, the colours in between royal blue and red represents the operating range of values that can either be considered high or low depending on their proximity to the said red and royal blue colours. From Figures 4-6, total deformations of 47.603, 54.286 and 49.216 mm were exhibited by hard drawn spring wire (A227), stainless steel (A313) and alloy steel (A213) shock absorber materials. The ability of these shock absorber materials to resist and withstand the loads and forces acting on them during service condition is a function of their tensile yield strength. In this case, hard drawn spring wire (A227) possessed the lowest tensile yield strength of 1591 MPa followed by tensile yield strength of 2068.8 MPa for alloy steel (A213) while stainless steel (A313) had tensile yield strength of 2240.8 MPa. This clearly indicate that shock absorber material with the highest yield tensile strength exhibited the least maximum total deformation among the three materials. This findings are graphically represented in Figure 7, which shows maximum total deformations for the for the three shock absorber materials. Careful observation of the shock absorber total deformation simulated profiles indicate that maximum deformation occurred around the area with concentrated by red colour which is the cylinder. In this case, the design can be altered to distribute the load more evenly, reducing stress concentrations and improving overall performance around this areas.

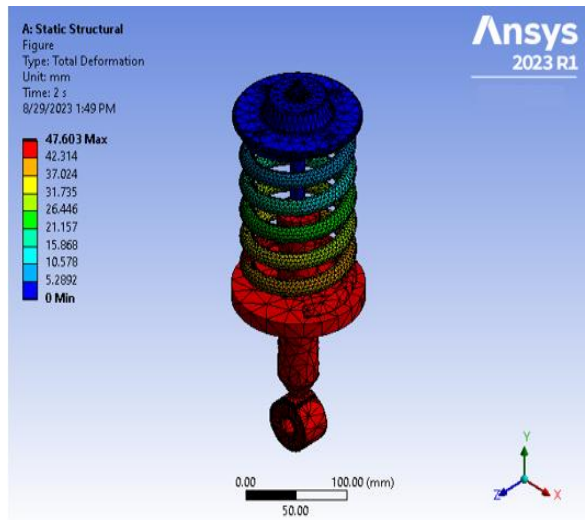

Figure 4. Shock absorber total deformation profile for stainless steel wire (A313)

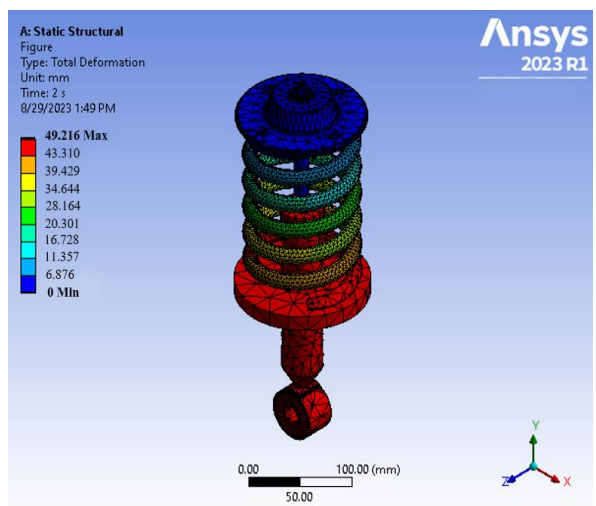

Figure 5. Shock absorber total deformation profile for alloy steel wire (A231)

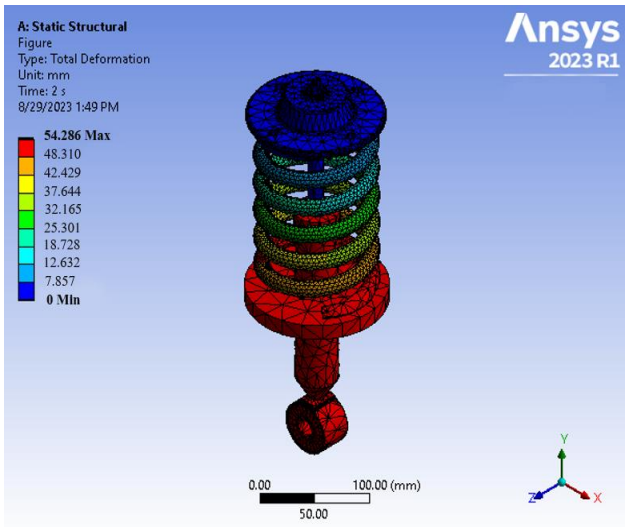

Figure 6. Shock absorber total deformation profile for hard drawn spring wire (A227)

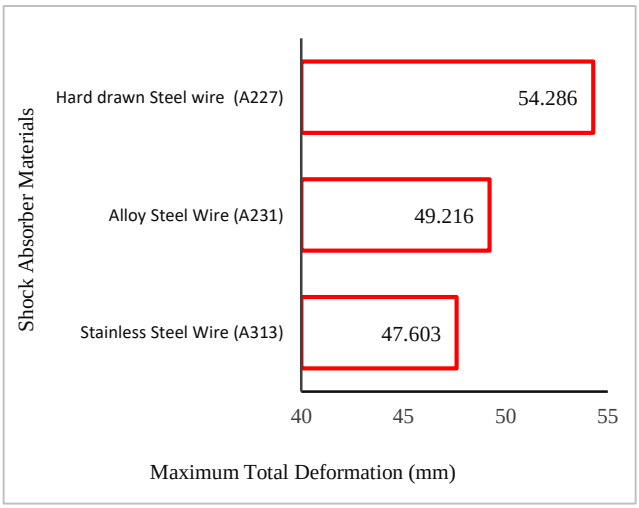

Figure 7. Plot of maximum total deformations for the three shock absorber materials

Similar to the case of total deformation, directional deformation was also analysed statically in this study. The FEA results which illustrates directional deformation profiles for three (3) conventional shock absorber materials including Hard Drawn Spring Wire (A227), Stainless Steel (A313) and Alloy Steel (A213) are presented in Figures 8-10. The same description provided for the significance and characteristics of colour profiles in the case of total deformation also apply to directional deformations.

From Figures 8-10, total deformations of 47.569, 48.762 and 53.303 mm were exhibited by stainless steel (A313), alloy steel (A213) and hard drawn spring wire (A227) shock absorber materials. As mentioned earlier, these shock absorber materials resist and withstand the loads and forces acting on them during service condition due to their tensile yield strength. This is evidence in the yield tensile properties of the materials presented in Table 1. Relationship between the material yield tensile strength property and directional deformation indicates that higher tensile yield strength property is responsible for lower directional strength and vice versa. In this case, it is observed that Hard Drawn Spring Wire (A227) which has the lowest tensile yield strength value of 1591 MPa yielded the highest directional deformation of 53.303 mm. The same findings are applicable to Stainless Steel (A313) and Alloy Steel (A213) shock absorber materials which has tensile yield strength value of 2240.8 as well as 2068.4 MPa, yielded directional deformations of 47.569 and 48.762 mm. Maximum directional deformations for the three shock absorber materials are graphically represented in Figure 11. Like the case of total deformations, the shock absorber directional deformation simulated profiles indicate that maximum directional deformation occurred around the area concentrated by red colour which is the cylinder.

Deformation can lead to changes in the internal hydraulic or mechanical mechanisms of the shock absorber. Increased deformation may result in reduced damping capabilities, leading to a harsher and less controlled ride. Excessive deformation can cause the shock absorber to lose its ability to absorb and dissipate energy effectively. Deformation can also lead to misalignment or binding of components, further compromising performance. Inadequate shock absorber performance due to deformation can negatively impact vehicle stability and handling. Reduced damping capabilities may result in increased braking distances and compromised tire grip on the road. Excessive deformation can lead to premature wear of other suspension components, such as springs and bushings. The overall safety of the vehicle and its occupants can be compromised if shock absorbers are not functioning optimally. Aggressive driving, such as hard braking and cornering, can increase the forces acting on the shock absorbers, leading to greater deformation. In FEA, maximum deformation refers to the highest displacement experienced by a shock absorber model under a given load condition. This parameter provides valuable insights into the structural integrity and potential failure points of the shock absorber. By identifying areas of excessive deformation, engineers can modify the design to ensure that the shock absorber can withstand the expected loads without compromising its performance or safety.

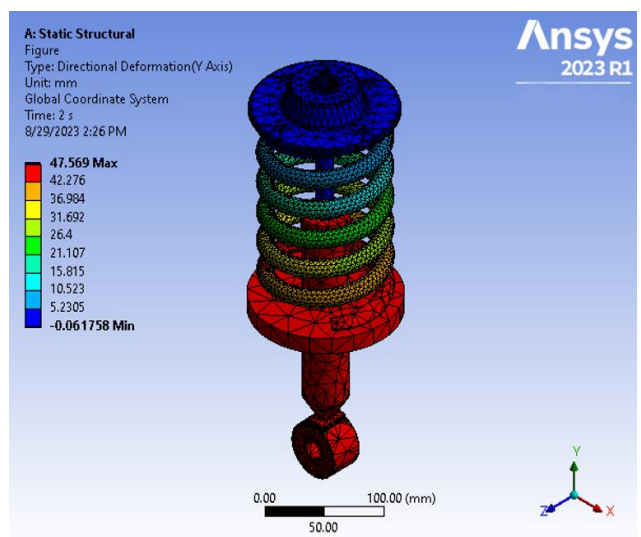

Figure 8. Shock absorber directional deformation profile for stainless steel wire (A313)

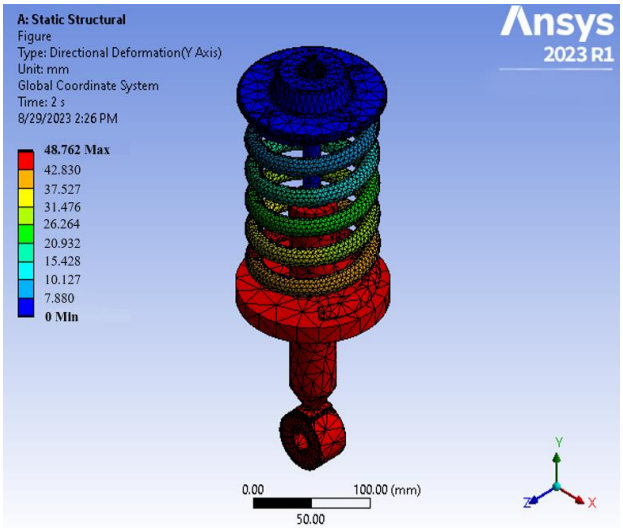

Figure 9. Shock absorber directional deformation profile for alloy steel wire (A231)

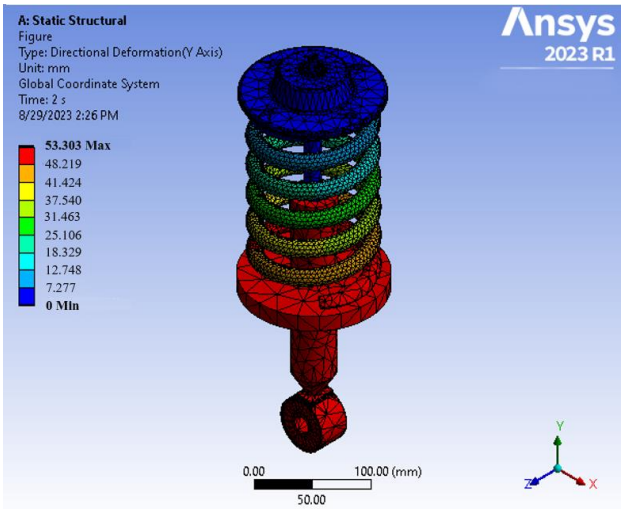

Figure 10. Shock absorber directional deformation profile for hard drawn spring wire (A227)

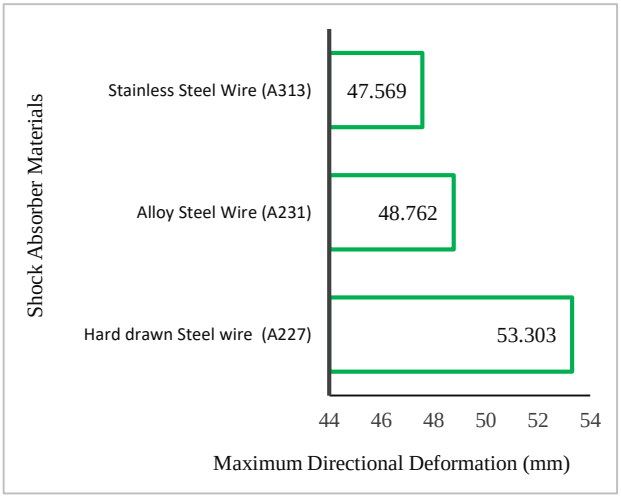

Figure 11. Maximum directional deformations for the three shock absorber materials

The maximum distortion criterion, also known as the von Mises failure criterion, implies that the failure of an elastic material under a constant load commences when the second variable of the deviatoric stress attains a critical stress value. This is governed by plasticity theory which applies primarily to elastic materials such as metals. In this study, the ability of the material to respond to external load conditions prior to deformation is considered visco-elastic, linear elastic, or nonlinear elastic [18, 19]. In this case, von Mises failure was modelled based on von Mises stress theory or equivalent tensile stress after observing that the shock absorber material under intense loading condition began to yield when the von Mises stress of the material attained the yield stress value [20]. In other words, the shock absorber materials are considered to fail if the von mises exceeds the yield strength of the material and vice versa.

The Von-Mises stress failure criterion satisfies the condition where two stress properties with the same distortion energy have the same Von-Mises stress. Von-mises stress profiles were obtained from the shock absorber models which were statically analysed with three different materials namely: Hard Drawn Spring Wire (A227), Stainless Steel (A313) and Alloy Steel (A213). The Von-mises stress profiles consisted of colour bands of royal blue, sky blue, lemon, yellow and red colors, each representing minimum and maximum values. Von-mises stress safe values or critical values at which shock absorber materials can fail depend on whether these Von-mises stress values in question have exceeded the shock absorber material tensile yield strength or not.

From the static analysis shown on the Von-mises stress profile in Figure 12-14, hard drawn spring wire (A227) had maximum equivalent Von-mises stress of 1205.8 MPa with tensile yield strength of 1591 MPa, alloy steel wire (A231) had maximum equivalent Von-mises stress of 1204.7 MPa with yield strength of 2068.4 MPa while stainless steel wire (A313) had maximum equivalent Von-mises stress of 1084.6 MPa with yield strength of 2240.8 MPa. Equivalent Von-mises stress results, seen on Figure 15, obtained from each of the three shock absorber materials indicated that shock absorber material with the highest tensile yield strength value exhibited the lowest equivalent Von-mises stress value under loading condition and vice versa. In this case, stainless steel wire (A313) exhibited the lowest equivalent stress value due to its tensile yield strength which is higher than that of the other two materials.

This findings also applies to the other two materials (hard drawn spring wire (A227) and alloy steel wire (A231)) that were employed in the analysis of this study. Considering the colour distribution across each of the shock absorber, blue and lemon colour dominated the entire profile, indicating that the shock absorbers still had the capacity to accommodate more load, and as well perform optimally under the statically loading conditions. The difference between the tensile yield strength values and maximum equivalent Von-mises stress obtained from each shock absorber material further buttressed that the shock absorber materials can still accommodate more load.

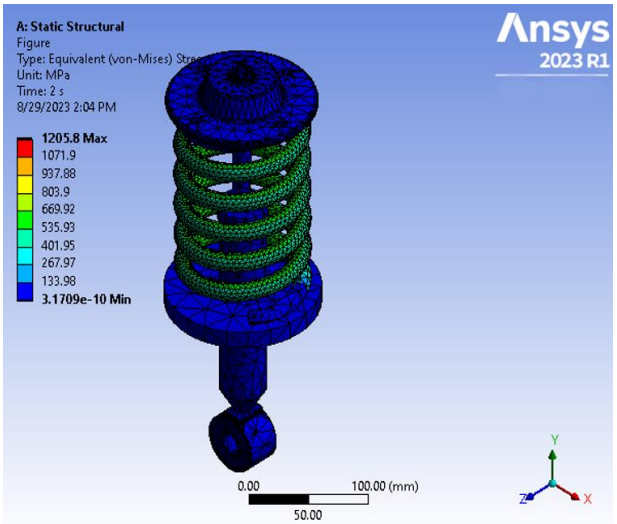

Figure 12. Shock absorber equivalent von-mises stress profile for hard drawn spring wire (A227)

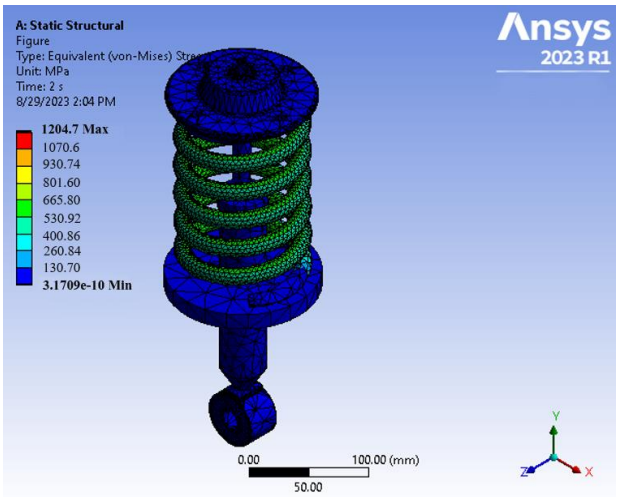

Figure 13. Shock absorber equivalent von-mises stress profile for alloy steel wire (A231)

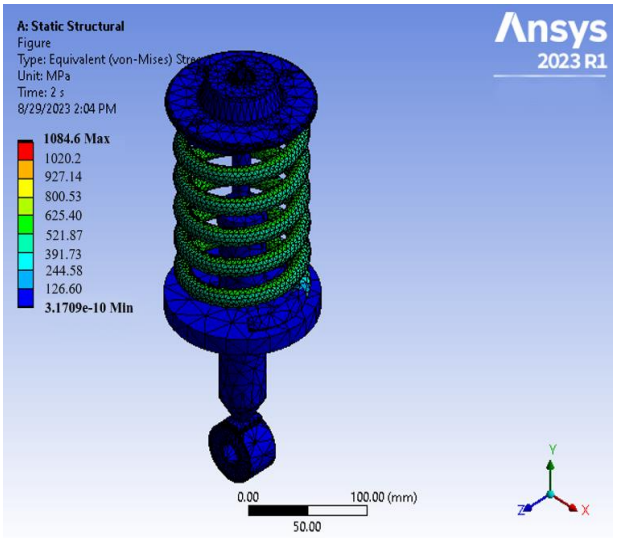

Figure 14. Shock absorber equivalent von-mises stress profile for stainless steel wire (A313)

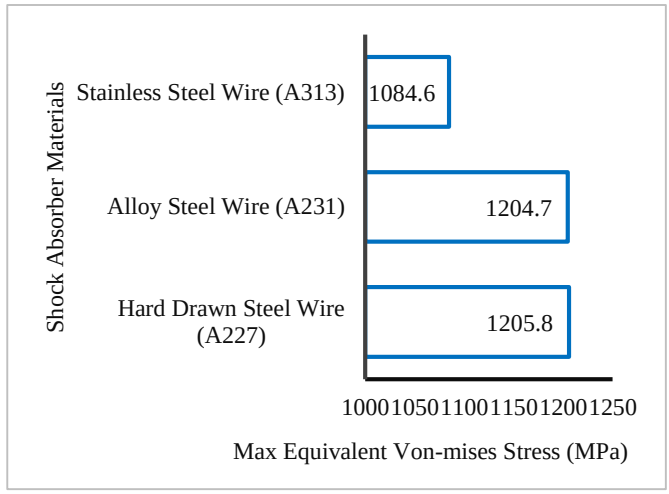

Figure 15. Plot of maximum equivalent von-mises stress for the three shock absorber materials

Static strain deformation is a property that relates to the rate at which a solid body changes or deforms in response to a load or force relative to its length, shape, or geometry. Therefore, if a random deformation mode is used when the normal stress value reaches a critical point, the structure may be exposed to failure, or when the total energy per unit volume exceeds the magnitude of the deformation, the structural unit is vulnerable to failure. From the concept of maximum strain energy, also referred to as octahedral shear stress theory, the absolute strain energy is broken down into static and geometric strain energy. The Static loading can take the form of compression or stretching, which can result in tension of the material, weakening and detaching the atomic bonds in the material's atomic structure and pulling them apart. This phenomenon is called strain elongation [21, 22]. If the loading effect is very intense, atoms in the metallic lattice will slide from their original deformed positions to new equivalent positions in the crystalline structure of the metal, causing permanent plastic deformation. The main reason why atoms slide over each other is related to the theory of dislocations, or defects in the metal crystalline arrangement of atoms [23]. In structural parts such as shock absorber as load-bearing parts, the shock absorber material is also subjected to compression strain elongation under long-term operating conditions, upward as well as the downward motion of the vehicle becomes alternating motion. This can also be caused by thermal expansion when the vehicle is in operating condition, which can be thought of as the equivalent load divided by the temperature change in the shock absorber material. Therefore, as the shock absorber temperatures increase during vehicle operation, this causes increased strain along the bonded areas within the atoms in the metal lattice of the shock absorber material.

Static equivalent strain analysis was carried out on three different materials namely: Hard Drawn Spring Wire (A227), Stainless Steel (A313) and Alloy Steel (A213). Figure 16-18 shows the maximum equivalent elastic strain derived from three shock absorber materials employed in this study, while maximum equivalent elastic strain for the three shock absorber materials are graphically represented in Figure 19. From the static strain profile, Hard Drawn Spring Wire (A227) had maximum equivalent strain of

0.0065269, Stainless Steel (A313) had maximum equivalent strain of 0.0060882 while Alloy Steel (A213) had maximum equivalent strain of 0.0061912. Like the case of Von-mises stress, equivalent strain results obtained from each of the three shock absorber materials showed that shock absorber material with the highest tensile yield strength value produced the lowest equivalent strain value under loading condition and vice versa. None of the three shock absorber materials indicated signs of failure under static loading condition analyzed in this study. This is evidence on the colour profiles (see Figure 16-18) which is predominantly constituted by lemon colour on the coil spring and blue colour on the cylinder, piston rod and strut mount. It should be noted that the blue colour represents minimum equivalent elastic strain value while lemon colour represents values in between minimum and maximum equivalent elastic strain.

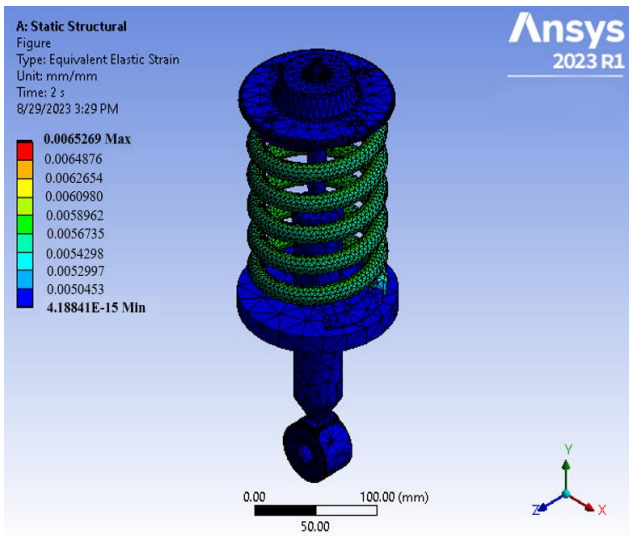

Figure 16. Shock absorber equivalent elastic strain profile for hard drawn spring wire (A227)

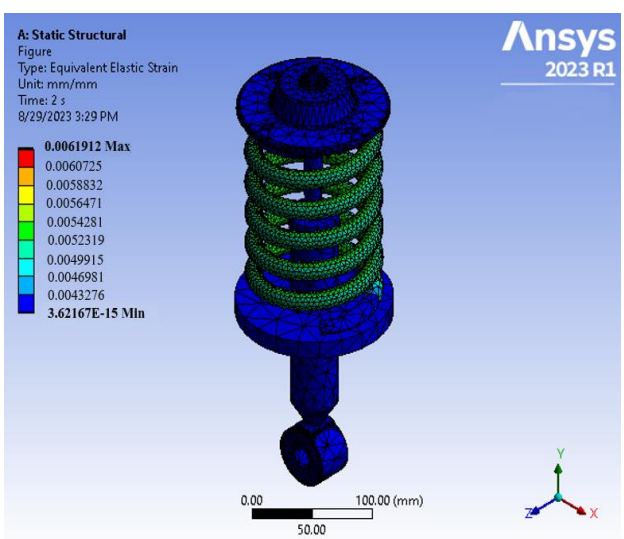

Figure 17. Shock absorber equivalent elastic strain profile for alloy steel wire (A231)

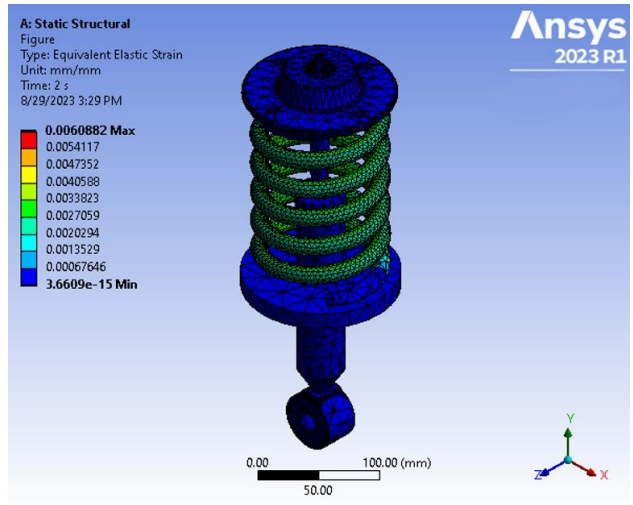

Figure 18. Shock absorber equivalent elastic strain profile for stainless steel wire (A313)

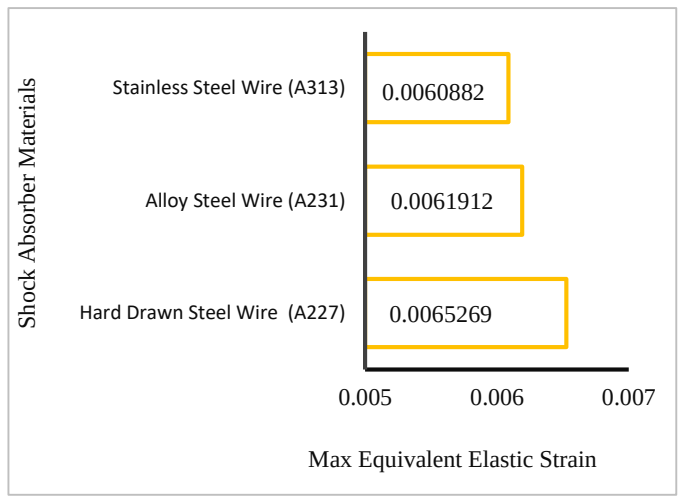

Figure 19. Plot of maximum equivalent strain for the three shock absorber materials

3.1. Preventive Measures for Total and Directional Deformations as well as Equivalent Von-mises stress and Equivalent Elastic Strain on Vehicle Shock Absorbers

Preventive measures for total deformation and directional deformation on vehicle shock absorber are crucial in ensuring the safety and performance of vehicles. Both types of deformation can lead to reduced effectiveness of the shock absorber, resulting in compromised vehicle handling and safety. They can be prevented in the following ways:

i. One preventive measure for total deformation is to regularly inspect the shock absorber for signs of wear and tear. This can include checking for cracks, dents, or other forms of damage that may indicate potential deformation. By identifying and addressing these issues early on, the risk of total deformation can be minimized.

ii. In terms of preventing directional deformation, proper installation and maintenance of the shock absorber and its connecting components is essential. Ensuring that the

components are securely fastened and aligned correctly with one another can help prevent excessive stress and strain that may lead to directional deformation. This includes following manufacturer guidelines for installation and regularly checking and replacing worn-out components. Proper maintenance can help prevent premature wear and deformation of the shock absorbers. Additionally, using high-quality materials and components that are designed to withstand the forces and pressures experienced during vehicle operation can also help prevent deformation.

iii. In addition to preventing directional deformation, it is important to drive carefully and avoid rough terrain or aggressive driving maneuvers that can put excessive stress on the shock absorbers. Additionally, using high-quality shock absorbers that are designed to withstand directional forces and pressures experienced during vehicle operation can also help prevent deformation.

iv. Another preventive measure for both total and directional deformation is to avoid overloading the vehicle beyond its recommended capacity. Excessive weight can put undue stress on the shock absorber components, increasing the likelihood of deformation. By adhering to the manufacturer's guidelines for vehicle weight limits, the risk of deformation can be significantly reduced.

Preventive measures for total deformation and directional deformation on vehicle shock absorber are essential for maintaining the safety and performance of vehicles. By regularly inspecting the components, ensuring proper installation and alignment, and avoiding overloading the vehicle, the risk of deformation can be minimized. Implementing these measures can help prolong the lifespan of the shock absorber components and ensure optimal vehicle performance.

On the other hand, preventive measures for equivalent Von-Mises stress and equivalent elastic strains on vehicle shock absorber components are crucial in ensuring the safety and longevity of these critical. The Von-Mises stress and elastic strains are key indicators of the structural integrity and performance of shock absorbers, and excessive levels of these parameters can lead to premature failure and potential safety hazards. They can be prevented in the following ways:

i. One of the primary preventive measures for managing Von-Mises stress and elastic strains on shock absorbers is proper material selection. The choice of materials with high strength, stiffness, and fatigue resistance properties can help reduce stress concentrations and minimize the risk of failure under dynamic loading conditions. Additionally, the use of advanced manufacturing techniques, such as precision machining and heat treatment processes, can further enhance the structural integrity and durability of shock absorbers.

ii. Another preventive measure for controlling Von-Mises stress and elastic strains on vehicle shock absorbers is proper design. The shock absorber should be designed to withstand the expected loads and operating conditions. Additionally, the design should incorporate features such as reinforcements, fillets, and stress-relieving features to distribute the stress and strains more evenly and reduce the likelihood of failure.

iii. Another important preventive measure is regular inspection and maintenance of shock absorbers. Periodic visual inspections and performance testing of the shock absorber can help identify potential issues, such as corrosion, fatigue cracks, wear, or damage before they escalate into more serious problems. Timely replacement of worn or damaged components can help prevent excessive stress and strain levels from compromising the overall performance and safety of the shock absorber system. Proper maintenance, such as lubrication and adjustment, can also help prolong the life of the shock absorber and prevent excessive stress and strains from developing.

iv. Furthermore, proper design and engineering practices play a critical role in preventing excessive Von-Mises stress and elastic strains on shock absorbers. The use of finite element analysis (FEA) and computer-aided design (CAD) tools can help optimize the design and geometry of shock absorbers to minimize stress concentrations and improve load distribution. Additionally, incorporating safety factors and design margins can help ensure that shock absorbers can withstand the expected operating conditions and potential variations in loading.

Preventive measures for managing equivalent Von-Mises stress and elastic strains on vehicle shock absorbers are essential for ensuring the reliability and safety of the suspension system. By implementing proper material selection, regular inspection and maintenance, and sound design practices, manufacturers and engineers can mitigate the risk of premature failure and enhance the performance and longevity of shock absorber systems. Ultimately, prioritizing preventive measures can help optimize the overall performance and safety of vehicle suspension systems, contributing to a smoother and more comfortable driving experience.

3.2. Augmentation of Vehicle Shock Absorbers

Shock absorbers are an essential component of a vehicle's suspension system, responsible for dampening the impact of bumps and vibrations on the road. The performance of shock absorbers directly affects the comfort, stability, and safety of the vehicle. In recent years, there has been a growing interest in augmenting vehicle shock absorbers to improve their performance and efficiency. The augmentation of vehicle shock absorbers can lead to significant benefits in terms of ride comfort, handling, and overall vehicle performance. These are discussed in the following highlights:

i. Improved Ride Comfort: One of the primary reasons for augmenting vehicle shock absorbers is to improve ride comfort. Traditional shock absorbers are designed to absorb and dissipate energy from bumps and vibrations, but they may not always provide a smooth and comfortable ride. By augmenting shock absorbers with advanced technologies such as adaptive damping systems or electronic control units, vehicle manufacturers can tailor the damping characteristics to suit different driving condi-

tions and road surfaces. This can result in a more comfortable and refined ride for passengers, especially over rough or uneven terrain.

ii. Enhanced Handling and Stability: In addition to improving ride comfort, augmented shock absorbers can also enhance vehicle handling and stability. By adjusting the damping force in real-time based on factors such as vehicle speed, steering input, and road conditions, augmented shock absorbers can help improve cornering performance, reduce body roll, and enhance overall stability. This can lead to a more engaging and dynamic driving experience, as well as improved safety and control in emergency situations.

iii. Increased Performance and Efficiency: Another benefit of augmenting vehicle shock absorbers is the potential for increased performance and efficiency. By optimizing the damping characteristics of the shock absorbers, vehicle manufacturers can improve the overall performance of the suspension system, resulting in better traction, reduced tire wear, and improved fuel efficiency. Additionally, augmented shock absorbers can help reduce the impact of road noise and vibrations on the vehicle, leading to a quieter and more comfortable driving experience.

The augmentation of vehicle shock absorbers can lead to significant benefits in terms of ride comfort, handling, and overall vehicle performance. By incorporating advanced technologies and control systems into shock absorbers, vehicle manufacturers can tailor the damping characteristics to suit different driving conditions and improve the overall driving experience for passengers. As the automotive industry continues to evolve, the augmentation of vehicle shock absorbers will play an increasingly important role in enhancing the comfort, stability, and efficiency of vehicles on the road.

4 Conclusions

The stress-strain deformation of vehicle shock absorbers plays a crucial role in ensuring the safety and performance of vehicles. This study explored the various factors that contribute to stress and strain in shock absorbers, including the material properties, design considerations, and operating conditions. By understanding these factors, manufacturers and engineers can make informed decisions to optimize the performance and durability of shock absorbers. One key finding is that the material properties of shock absorbers significantly influence their stress-strain deformation. The choice of materials, such as steel or alloys, can impact the overall strength and stiffness of the shock absorber. Additionally, the manufacturing process and heat treatment techniques can further enhance the material properties, reducing the risk of failure under extreme conditions. Furthermore, the design considerations of shock absorbers also play a vital role in managing stress and strain. Factors such as the size, shape, and geometry of the shock absorber can affect its ability to withstand external forces and absorb energy. Additionally, the presence of features like grooves, ribs, or reinforcements can enhance the structural integrity and reduce stress concentrations. Operating conditions, including the vehicle's weight, speed, and road conditions, also contribute to stress and strain in shock absorbers. Heavy loads and rough terrains can subject the shock absorbers to higher stress levels, potentially leading to premature failure. Therefore, it is crucial to consider these factors during the design and selection of shock absorbers to ensure their optimal performance and longevity. Based on the findings discussed above, several recommendations can be made to improve the stress-strain deformation of vehicle shock absorbers:

i. Material Selection: Manufacturers should carefully select materials with appropriate strength and stiffness properties for shock absorbers. Conducting thorough material testing and analysis can help identify the most suitable materials for specific applications.

ii. Manufacturing Process: Employing advanced manufacturing techniques, such as precision machining and heat treatment, can enhance the material properties and reduce the risk of stress and strain deformation. Strict quality control measures should be implemented to ensure consistent production.

iii. Design Optimization: Engineers should focus on optimizing the design of shock absorbers to minimize stress concentrations and improve overall structural integrity. Utilizing computer-aided design (CAD) software and conducting finite element analysis (FEA) can aid in identifying potential weak points and optimizing the design accordingly.

iv. Regular Maintenance: Vehicle owners should adhere to regular maintenance schedules, including inspecting and replacing worn-out shock absorbers. This will help prevent excessive stress and strain on the components, ensuring their optimal performance and longevity.

v. Road Infrastructure: Governments and road authorities should invest in improving road infrastructure to minimize the impact of rough terrains and potholes on shock absorbers. Well-maintained roads can significantly reduce stress and strain on vehicles, enhancing their overall safety and performance.

vi. Other failure mechanisms such as fatigue, bending, buckling, corrosion, etc. should also be investigated. This can form a broad body of knowledge on shock absorber failures and prolongment of its duty cycle.

In conclusion, stress-strain deformation in vehicle shock absorbers is a critical aspect that requires careful consideration. By implementing the recommendations mentioned above, manufacturers, engineers, vehicle owners, and road authorities can collectively contribute to the improved performance, durability, and safety of shock absorbers in vehicles.

References

1. Ryabova, I. V., Novikova, V. V & Pozdeev, A. V. (2016). Efficiency of Shock Absorber in Vehicle Suspension. Procedia Engineering, 150, 354-362.
2. Singh, W. S. & Srilatha, N (2018). Design and Analysis of Shock Absorber: A Review. Materialstoday: Proceedings, 5(2-1), 4832-4837.
3. Xu, T., Liang, M., Li, C. & Yang, S. (2015). Design and analysis of a shock absorber with variable moment of inertia for passive vehicle suspensions. Journal of Sound and Vibration, 355, 66-85.
4. Guba, S., Ko, Y., Rizzoni, G., Heydinger, G. J., Guenther, D. A. & Wittman, T. (2006). The Impact of Worn Shocks on Vehicle Handling

and Stability. 115(6), Journal of Passenger Car: Mechanical Systems Journal, 400-408.

5. Paz, O. D. (2004). Design and performance of electric shock absorber. Louisiana State University, USA.
6. Manashkin, L., Myamlin, S. & Prikhodko, V. (2009). Oscillation Dampers and Shock Absorbers in Railway Vehicles (Mathematical Models). Dnipropetrovsk National University of Railway Transport, Ukraine.
7. Sani, M. S., Rahman, M. M., Noor, M. M., Kadirgama, K. & Rejab, M. R. (2008). Study on Dynamic Characteristics of Automotive Shock Absorber System. Malaysian Science and Technology Congress, KLCC, Malaysia, 16-17 December, 2008.
8. Zhang, R. (2019). A Study of Vehicle Regenerative Shock Absorber. School of Engineering, RMIT University, Melbourne, Australia.
9. Tan, W. H., Cheah, J. X., Lam, C. K., Lim, E. A., Chuah, H. G. & Khor, C. Y. (2017). Vibration analysis on compact car shock absorber. IOP Conference Series: Journal of Physics, 908, 1-8.
10. SelvaKumar, A., Kumar, R. S., Kumar, M. S. & Rajan, S. V. (2018). Design and Analysis of Shock Absorber. International Journal of Creative Research Thoughts, 6(1), 1321- 1330.
11. Bhasha, A. C., Reddy, N. V. & Rajnaveen, B. (2017). Design and Analysis of Shock Absorber. International Research Journal of Engineering and Technology, 4(1), 201-207.
12. Olugbade, T. O., Mohammed, T. I. & Ojo, O. T. (2018). Static stress analysis and displacement of a tricycle rear shock absorber using finite element analysis. Leonardo Electronic Journal of Practices and Technologies, 33, 139-158.
13. Santharaguru, N., Abdullah, S., Chin, C. H. & Singh, S. S. (2022). Failure behaviour of strain and acceleration signals using various fatigue life models in time and frequency domains. Engineering Failure Analysis, 139, 106454.
14. Kareem, S. A., Anaele, J. U., Aikulola, E. O., Olanrewaju, O. F., Omiyale, B. O., Bodunrin, M. O. & Alaneme, K. K. (2023). Hot deformation behaviour, constitutive model description, and processing map analysis of superalloys: An overview of nascent developments. Journal of Materials Research and Technology, 26, 8624-8669.
15. Kumhar, V. (2016). Structure Analysis of Shock Absorber Spring Using Finite Element Analysis. International Journal of Mechanical, Civil, Automobile and Production Engineering, 6(1), 1-10.
16. Imoro, I., Nkrumah, J., Ziblim, B. & Mohammed, A. (2023). Analysis of the Material Properties of Vehicle Suspension Coil Spring. World Journal of Engineering and Technology, 11, 827-858.
17. Ogiemudia, O. G., Ikpe, A. E & Chughiefe, L. E. (2020). Design and Fabrication of a Modular Melon Depodding Machine for Optimum Performance in Nigerian Agricultural Sector. European Mechanical Science, 4(3), 103-112.
18. Ikpe, A. E. & Owunna, I. B. (2017). Design of Vehicle Compres-sion Springs for Optimum Performance in their Service Condition. International Journal of Engineering Research in Africa, 33, 22-34.
19. Bai, X., Chen,J., Guan, X., Peng, Z., Li, G., Zhou, H., Shi, X., Sun, L. & Fu, B. (2022). Modeling and analysis of residual stresses of camshaft induced by swing grinding processes. The International Journal of Advanced Manufacturing Technology, 121, 6375-6391.
20. Ikpe, A. E. & Owunna, I. B. (2019). Design of Remotely Controlled Hydraulic Bottle Jack for Automobile Applications. International Journal of Engineering Research and Development, 11(1), 124-134.
21. Boresi, A. P., Schmidt, R. J. & Sidebottom, O. M. (1993). Advance Mechanics of Materials, Fifth Edition. John Wiley & Sons, Inc, USA.
22. Ikpe, A. E., Ikpe, E. O. & Etuk, E. M. (2021). On the Mechanical Behaviour of Distinct Auto Wheel Materials under Static and Dynamic In-service Loading Cycle. International Journal of Computational and Experimental Science and Engineering, 7(2), 61-75.
23. Ikpe, A. E. & Ikpe, E. O. (2022). Optimizing the Welding Input Parameters of AISI 1020 Mild Steel Plate for Desired Output Response Using Tungsten Inert Gas Welding Technique. Al-Farabi 4th International Congress on Applied Sciences, August 19-20, Erzurum, Turkey.

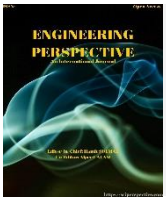

e-ISSN:2757-9077

ENGINEERING PERSPECTIVE

https://sciperspective.com/ Research Paper

Thermal Modeling of Solid Hydrogen Storage in a LaNi5 Metal Hydrid Tank

Mohand-Ouyahia Bousseksou[1*], Yucai Lin[1]

[1]*Capgemini engineering, Ile de France, Division APA, 12 rue de la Verrerie, 92190 Meudon, France*

ABSTRACT

This paper presents a detailed 3D model of a solid hydrogen storage tank based on metal hydride LaNi5 technology, utilizing COMSOL Multiphysics 6.1 software. The model takes into account the coupling of momentum, heat, mass and energy transfer within the LaNi5 metal hydride during hydrogen absorption. The main objective of the study is to analyze the temporal evolution of temperature and pressure within the tank as hydrogen is absorbed. In addition, the paper investigates the effectiveness of a cooling strategy involving the integration of cooling tubes into the tank configuration. This approach aims to enhance the thermal management of the storage system by dissipating excess heat generated during hydrogen absorption.

Simulation results demonstrate the changes in temperature and pressure occurring within the LaNi5 metal during the process of hydrogen absorption. The implementation of an air-based cooling system emerges as an effective means of regulating the temperature of the storage tank, thus creating optimal conditions for hydrogen absorption processes. This understanding is essential to the development of efficient thermal management solutions for solid hydrogen storage technologies. By comprehensively analyzing the thermal behavior of the LaNi5 metal hydride tank, this numerical study suggests that the efficient design of storage system is very important for rapid absorption of hydrogen.

Keywords: COMSOL Multiphysics; Cooling strategy; Hydrogen; LaNi5; Storage tank.

History	**Author Contacts**
Received: 07.01.2024	**Corresponding Author*
Accepted: 14.03.2024	e-mail addresses : mohand-ouyahia.bousseksou@capgemini.com, yucai.lin@capgemini.com
How to cite this paper:	Bousseksou, M.O., Lin, Y., (2024). Thermal Modeling of Solid Hydrogen Storage in a LaNi5 Metal Hydrid Tank. Engineering Perspective, 4(1), 32-39. http://dx.doi.org/10.29228/eng.pers.75265

1. Introduction

Since the beginning of the 21st century, the entire world has shifted its interest towards searching for alternatives to traditional transport technologies due to the consequences of their impact on the climate [1]. All industrial sectors are aiming to overcome their dependence on fossil fuels, which are responsible for a substantial proportion of greenhouse gas emissions [2].

In the environmental context, hydrogen is a promising energy carrier in the face of current challenges. it is a solution that can be used to replace fossil fuels in various fields, notably in the automotive sector [3], where it is used as a fuel to power a hydrogen fuel cell [4, 5] or even internal combustion engines [6]. Thanks to its various production [7] and storage methods [8], it is considered a clean, renewable, and highly powerful energy source.

Currently, there are three main approaches for hydrogen storage. High-pressure hydrogen storage, which is realized by compressing hydrogen gas at pressures ranging from 300 to 700 bars. Low-temperature liquid storage, it involves cooling hydrogen gas to as low as -253 °C to condensate it to a liquid state and solid-state hydrogen storage that requires the use of metal hydrides to absorb hydrogen gas [8].

The use of metal hydride-based hydrogen storage offers a significant volume density (of the order of 120 kg/m^3) compared with the other two storage methods, liquid (71 kg/m^3), and gaseous (42 kg/m^3) [9]. However, the enormous amount of heat emitted during the hydriding process is a major drawback [10]. This poses a challenge to the thermal management of the storage tank [11].

The storage of hydrogen in solid form utilizing metal hydrides necessitates thorough consideration of the thermal challenges. In order to be enable to absorb the hydrogen the tank must be maintained at an appropriate temperature [12].

The main objective of this work is to study the absorption phe-

nomenon of a metal hydride-based solid-state hydrogen storage system for powering a PEMFC (proton exchange membrane fuel cell) fuel cell used in vehicles.

To optimize the performance of metal hydride tanks, research into tank design and configuration is essential for efficient operation of stored hydrogen distribution. The present work implies a numerical study on the comparison of different techniques proposed to improve the thermal management of a solid-state hydrogen storage tank based on a LaNi5 metal hydride. In particular, the evolution of the temperature within hydride bed upon absorption.

2. Numerical model

This study, a numerical model was used to simulate the thermal behavior of a solid-state hydrogen storage tank. The physical model of the metal hydride tank studied is composed of a solide phase (metal: LaNi5) and a pure gaseous phase (hydrogen: H_2), thus forming a porous medium as showed in Figure 1. The choice of tank geometry is based on a 3D type is seen on Figure 2. The tank consists of a cylindrical of radius R = 0.25 m and height H = 1 m. The hydrogen is injected into the tank from the top at P_{H2_in} = 8 bars during the absorption of hydrogen. The lateral surface experiences cooling through natural convection, while the remaining orthogonal surfaces are presumed to exhibit adiabatic behaviour. The temperature is maintained constant at the extremities of the tank and set to the value of T_0 = 293 K.

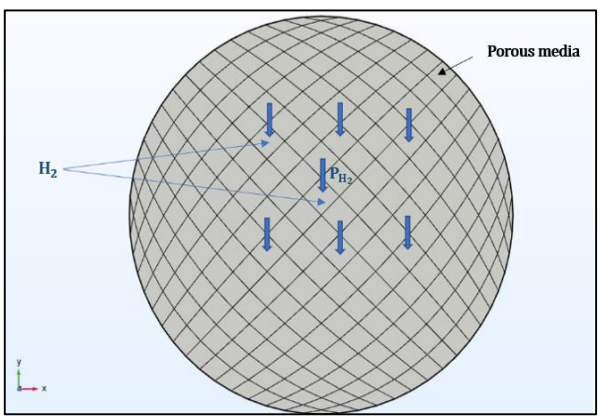

Figure 1. Schematic section view of the hydrogen absorption in a porous media

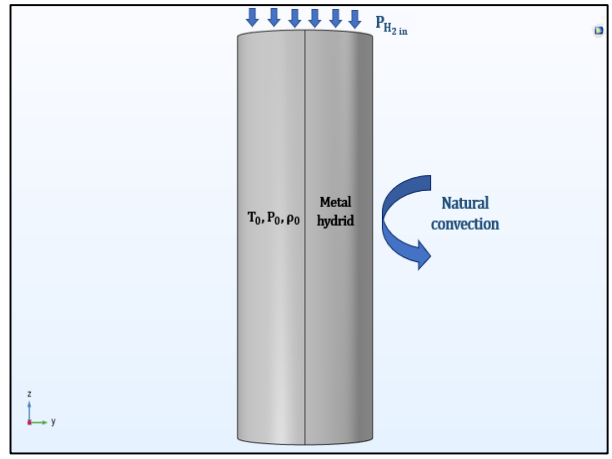

Figure 2. The geometry of the model

To simplify the numerical model, the following assumptions are considered [13, 14, 15, 16, 17]:

i. The gas phase (hydrogen) is pure.
ii. The tank is considered in three dimensions (3D).
iii. The media are in local thermal equilibrium between gas and solid.
iv. The validity of Darcy's law. ²z
v. The radiative transfer in the porous medium is neglected.
vi. The hydrogen inlet temperature and pressure are maintained constant (T_0 and P_0).

The equations governing the hydriding process are discussed in detail below.

2.1 Energy conservation

According to the [14, 18] heat transfer modeling can be simplified by setting a temperature variable for the system (Eq. (1)).

$$(\rho C_p)_{eff}\frac{\partial T}{\partial t} + \rho_g C_{pg} v_g \nabla T = \nabla(\lambda_{eff}\nabla T) + S_m \quad (1)$$

Where the effective heat capacity, $(\rho C_p)_{eff}$, is given by Eq. (2):

$$(\rho C_p)_{eff} = \epsilon\rho_g C_{pg} + (1-\epsilon)\rho_s C_{ps} \quad (2)$$

The effective thermal conductivity can be written as:

$$\lambda_{eff} = \epsilon\lambda_g + (1-\epsilon)\lambda_s \quad (3)$$

The heat source term S_m is equal to:

$$S_m = (1-\epsilon).\parallel \Delta H \parallel.\frac{\partial \rho_s}{\partial t} \quad (4)$$

With, ϵ is the porosity of the medium studied and $\frac{\partial \rho_s}{\partial t}$ is the amount of hydrogen absorbed by the metal as a function of time.

In the case of absorption [19]:

$$\frac{\partial \rho_s}{\partial t} = C_a . e^{\frac{-E_a}{RT}} . ln\left(\frac{P}{P_{eq}}\right)(\rho_{ss} - \rho_s) \quad (5)$$

With P_{eq} is the equilibrium pressure.

2.2 Mass conservation

For gaseous media (hydrogen):

$$\epsilon \frac{\partial \rho_{H2}}{\partial t} + div(\rho_{H2}\overrightarrow{v_{H2}}) = -\dot{m} \quad (6)$$

Where, ρ_{H2} is the density of gas (hydrogen) and υ_{H2} is the velocity field of the gas (hydrogen).

For solid media (metal hydride):

$$(1 - \epsilon)\frac{\partial \rho_s}{\partial t} = -\dot{m} \quad (7)$$

Where, ρ_s the density of solide (bed) and $\dot{m}$ the mass transferred from the gas phase to the solid in function of time.

The gas density ρ_{H2} is described by the equation:

$$(1 - \epsilon)\frac{\partial \rho_s}{\partial t} = -\dot{m} \quad (8)$$

2.3 Momentum conservation

According to Darcy's law the hydrogen gas velocity within the thank is:

$$V_{H2} = \frac{k}{\mu_{H2}}\vec{\nabla}_P \quad (9)$$

Where, k is the intrinsic permeability of the porous medium (m^2), and μ_{H2} is the dynamic viscosity of the fluid (Pa.s).

2.4 Kinetics reaction

The absorption kinetic of a hydride metal is related to the amount of hydrogen absorbed by the metal over time can be expressed as:

$$\frac{\partial \rho_s}{\partial t} = C_a\, exp\left(-\frac{E_a}{RT}\right) ln\left(\frac{P}{P_{eq}}\right)(\rho_{sat} - \rho_s) \quad (10)$$

The equilibrium pressure P_{eq} is calculated using the Van't Hof relation via the following term [19]:

$$ln\left(\frac{P_{eq}}{P_0}\right) = A - \frac{B}{T} \quad (11)$$

With A and B are Van't Hoff constants having the values of 12.95 and 3731.42 respectively [19].

2.5 Initial and boundary conditions

Initially "t = t_0", the temperature, pressure and hydride density are assumed to be constant (Figure 2).

$$T(t_0, r, z) = T_0 \quad (12)$$

$$P(t_0, r, z) = P_0 \quad (13)$$

$$\rho(t_0, r, z) = \rho_0 \quad (14)$$

At the hydrogen inlet (Figure 2):

$$T(x, y, t) = T_0 \quad (15)$$

$$P(x, y, t) = P_0 \quad (16)$$

The lateral cooling wall (Figure 2):

$$h_{conv}(T - T_0) \quad (17)$$

2.6 Modeling parameters

The thermophysical proprieties of the LaNi5 and H_2 used in this study are succinctly presented in Table 1.

Table 1. Thermophysical proprieties of the metal hydride (LaNi5), hydrogen (H_2) and other parameters used in the simulations [13, 14, 16, 17, 20, 21].

P_{in}	8 [bar]
T_{in}	293 [K]
M_{H2}	2.01588 [g/mol]
λ_{H2}	0.24 [W/m. K]
ρ_{H2}	0.0838 [kg/m^3]
Cp_{H2}	14.890 [J/mol. K]
P_0	1 [bar]
T_0	293 [K]
h_{conv}	1650 [W/ (m².K)]
k_{hyd}	2.4 [W/ (m.K]]
ϵ	0.5
Cp_s	419 [J/kg. K]
k	3×10^{-12} [m²]
ρ_{sat}	8520 [kg/m^3]
ρ_s	8400 [kg/m^3]
Cp_{air}	1005 [J/kg. K]
k_{air}	0.025 [W/(m².K)]
Cp_{H2O}	4180 [J/kg. K]
k_{H2O}	0.598 [W/(m². K)]
T_c	293 [K]
R	0.02 [m]
E_a	21170 [J/mol]
C_a	59.187 [1/s]
ΔH	30 [kJ/kg]
R_g	8.314 [J/(mol. K)]

2.7 Cooling strategies

In order to enhance the cooling efficiency of the storage tank, a novel approach was contemplated. This entailed the incorporation of internal cooling tubes withing the metal hydride, as illustrated in Figure 3 (b and c). While maintaining the original geometry of the tank, two cooling tubes with a radius of 0.02 m were integrated.

For this process, two heat transfer fluids were used: air and water. These fluids were chosen because of their specific heat transfer properties, abundance, and their common use in cooling applications. The aim of this study is to evaluate the effectiveness of the aforementioned approach using two distinct fluids, compared with the case of a basic tank which cools solely by natural convection. A schematic of the different configurations is presented in Figure 3. The cooling tubes, which are supposed isotherm (Figure 3):

$$T(t,r,z) = T_0 \tag{18}$$

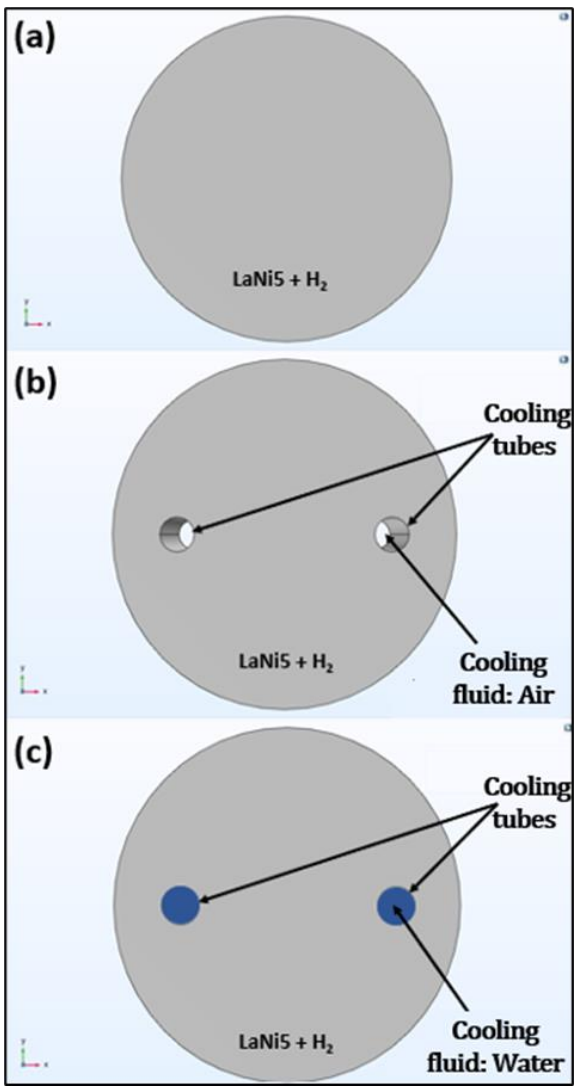

Figure 3. Schematic section view of the tank equipped with two cooling tubes. (a) basic tank, (b) tank with two air-filled cooling tubes and (c) tank with two water-filled cooling tubes

3. Results and discussion

In this section, we determine the variation of temperature and pressure as a function of time during the absorption process in hydrogen storage tanks. Then, we will provide a comparative assessment of the temperature variation in the tank for the various proposed cooling techniques.

3.1 Temperature evolution

Figure 4 shows the temperature variation as a function of time at a specific measuring point within the tank. A rapid increase in temperature can be observed, reaching the maximum value (345 K), attributed to the exothermic nature of as the hydriding reaction of the intermetallic. Then, after this rapid increase, the temperature gradually decreases towards ambient temperature (to 298 K). Our results align with those reported in the literature [12].

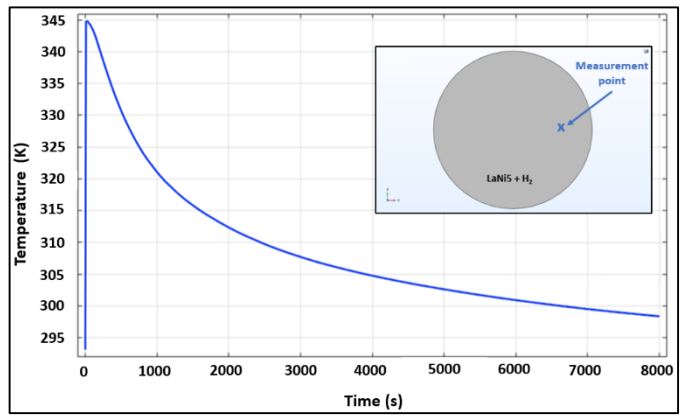

Figure 4. Temperature variation as a function of time during absorption

The spatio-temporal evolution of the temperature inside the thank from 0 to 4000 is shown in the Figure 5. The temperature rises rapidly, reaching a maximum value of 345 K, followed by a gradual descent to reach a peak temperature of 330 K after 4000 s.

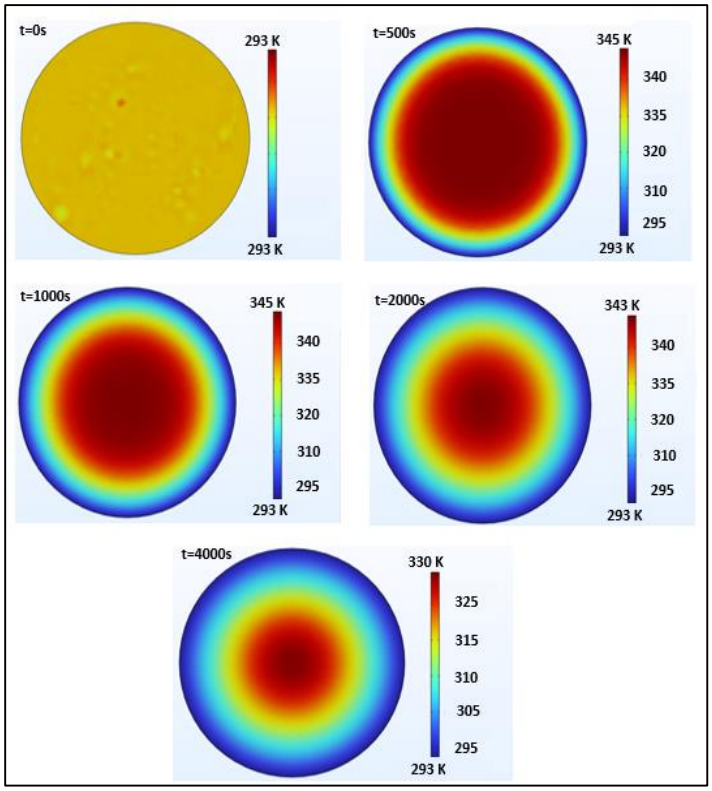

Figure 5. Spatio-temporal temperature variation

3.2 Pressure evolution

Figure 6 illustrates the temporal variation of hydrogen pressure within the hybrid bed. It is observed that the pressure increases rapidly until it reaches a steady state corresponding to the set pressure. This rapid and uniform stabilization of pressure is observed throughout the entire hybrid zone, leading to the conclusion that H_2 percolation times are extremely short [22].

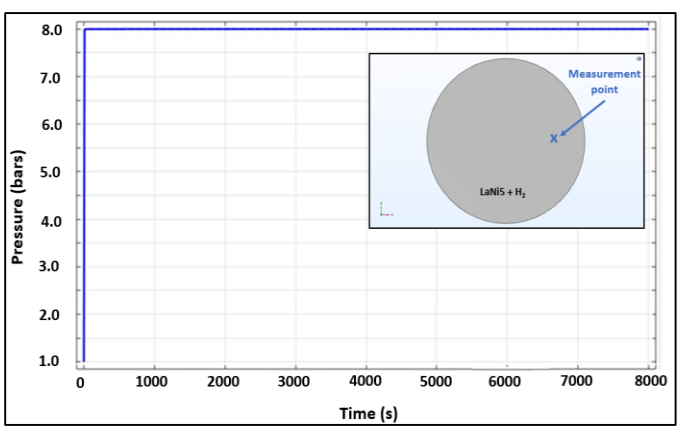

Figure 6. Temperature Pressure variation as a function of time

3.3 Effect of the tubes cooling

Figure 7 illustrated the temperature field reigning inside the tank from 0 s to 4000 s in three different configurations ((a) basic tank, (b) tank with two air-filled cooling tubes and (c) tank with two water-filled cooling tubes). We can observe the rapid growth of the temperature in the hydride bed at the start for all three tank configurations. Then, they decrease progressively as the kinetics of the hydriding reaction slow. However, the rate in which the temperature goes down shows a marked disparity between configurations with cooling tubes and those without, where cooling is based solely on the peripheral wall of the tank. We observe a rapid increase, reaching a maximum value of 345 K for t = 500 s, both for the configuration without cooling tubes and for that with air-filled tubes. However, in the case of the configuration with water-filled tubes, a slightly lower maximum temperature of 344 K is observed. Thereafter, it gradually decreases to reach a temperature of 330 K after 4000 s in the case of the tank without cooling tubes, while for the configurations with cooling tubes filled with air and water, the corresponding temperatures after 4000 s are 319 K and 318 K, respectively.

The presence of cooling tubes in the storage tank reduces the time required to cool the hydride bed, which in turn reduces the hydriding time. This approach considerably increases the heat exchange surface area within the tank. The cooling tubes also enable the heat to be dispersed more efficiently.

The use of water as a coolant is highly effective due to its excellent heat transfer properties, making it an efficient cooling medium. Nonetheless meticulous selection of materials for the design of cooling tubes is imperative to mitigate potential issues such as corrosion and leaks, thereby ensuring the enduring robustness of the envisaged cooling system. However, it's worth noting that in some cases, air may be preferable to water as a cooling medium. While water is highly efficient for heat transfer, it can also present additional challenges in terms of corrosion and maintenance, especially if the construction materials are not compatible with water. Conversely, utilizing air as a coolant offers a more straightforward and potentially more reliable alternative, exhibiting reduced susceptibility to operational issues. This can be particularly advantageous in applications where water-related risks are high or where simplicity and ease of maintenance are priorities.

Therefore, considering that there is only a 1 K temperature difference between air cooling and liquid cooling, opting for air cooling may be more effective compared to the potential issues associated with using water.

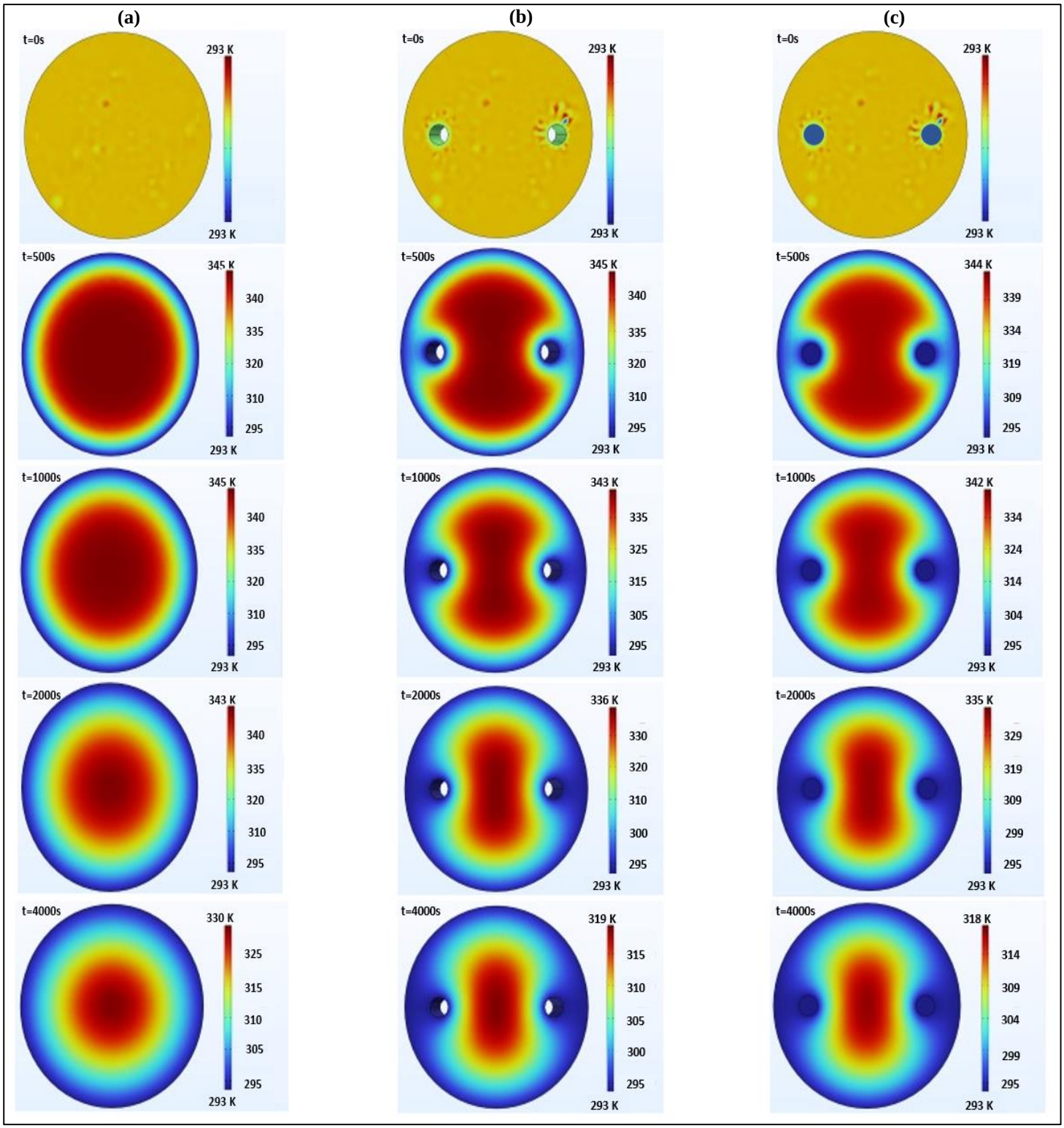

Figure 7. Variation of the temperature in function of time during absorption for different configurations: (a) basic tank, (b) tank with two air-filled cooling tubes and (c) tank with two water-filled cooling tubes

4. Conclusions

This study contributes to a better understanding of hydrogen storage in tanks, in particular the hydrogen absorption process with different designs of the cooling system. A three-dimensional mathematical model describes how heat and mass transfer in metal hydride are carried out. The results showed a substantial and swift generation of heat during the hydrogen absorption. Furthermore, this study compares cooling solutions for solid hydrogen storage tanks. It offers different approaches to controlling the temperature and thus ensuring safe hydrogen storage. Incorporating cooling tubes filled with air significantly enhances heat transfer within the tank.

There are many perspectives and avenues for achieving our study:

i. Desorption phenomenon: In the current work we have studied the phenomenon of hydrogen adsorption. Subsequently, a systematic examination of hydrogen desorption kinetics is envisaged for future research. This will involve examining the influence of key parameters including temperature, pressure, material characteristics and surface morphology on the desorption process (a Model utilizing COMSOL Multiphysics is currently under development).

Incorporating phase-change materials (PCMs) within hydrogen tank facilitates the storage of hydrogen at elevated densities and reduced temperatures when compared to high-pressure and cryogenic tanks. The integration of a PCM is an important part of the thermal management of the tanks and offers several important advantages, such as the recovery of excess heat and the maintenance of temperature at optimum levels. There are many perspectives and avenues for achieving our study.

Acknowledgment

This work was supported by Capgemini engineering-France (Innovative and Intelligent Powertrain Research & Innovation Department). The authors would like to thank the other members of the team, Fatima Haidar, Thierry Bertau, Chayma Mohsni and Fabien Furfaro. The authors would also like to thank the interns of the iPowertrain project.

Nomenclature

P_{in}	Inlet pressure of hydrogen
T_{in}	Inlet temperature of hydrogen
M_{H2}	Molecular mass of hydrogen
λ_{H2}	Heat conductivity of the H_2 gas
ρ_{H2}	Density of the H_2 gas
Cp_{H2}	Specific heat of H_2 gas
P_0	Initial pressure
T_0	Initial temperature
h_{conv}	Heat convection coefficient
k_{hyd}	Specific heat of the solid
ϵ	Permeability of the metal
Cp_s	Specific heat of the solide
k	Permeability of the metal
ρ_{sat}	Saturated metal hydride density
ρ_s	H_2-free metal hydride density
Cp_{air}	Specific heat of air
k_{air}	Heat conductivity of air
Cp_{H2O}	Specific heat of H_2O
k_{H2O}	Heat conductivity of air
T_c	Cooling tubes temperature
R	Annular disc unit radius
E_a	Activation energy for absorption
C_a	Absorption rate constant
ΔH	Reaction heat of formation
R_g	Universal gas constant

Conflict of Interest Statement

The authors declare that they have no known competing financial interests or personal relationships that could have appeared to influence the work reported in this paper.

CRediT Author Statement

Mohand-Ouyahia Bousseksou: Writing- review & editing, supervision, project leader, Methodology & software, **Yucai Lin:** Formal analysis.

References

1. Mazloomi, K., & Gomes, C. (2012). Hydrogen as an energy carrier: Prospects and challenges. Renewable and Sustainable Energy Reviews, 3024-3033.
2. Maestre, V., Ortiz, A., & Ortiz, I. (2021). Challenges and prospects of renewable hydrogen-based strategies for full. Renewable and Sustainable Energy Reviews, 111628.
3. Gurz, M., Ertugru, B., Hames, Y., & Kaya, K. (2017). The meeting of hydrogen and automotive: A review. International Journal of Hydrogen Energy, 23334-23346.
4. Aminudin, M., Kamarudin, S., Lim, B., Majilan, E., Masdar, M., & Shaari, N. (2023). An overview: Current progress on hydrogen fuel cell vehicles. International Journal of Hydrogen Energy, 4371-4388.
5. Haidar, F., Arora, D., Soloy, A., & Bartoli, T. (2024). StudyProton-Exchange Membrane Fuel Cell Degradation and its Counter Strategies: Flooding/drying, Cold Start and Carbon Monoxide Poisoning. International Journal of Automotive Science And Technology, 8(1), 96-109.
6. Falfari, S., Cazzoli, G., Mariani, V., & Bianchi, G.-M. (2023). Hydrogen Application as a Fuel in Internal Combustion Engines. Énergies, 2545.
7. Younas, M., Shafique, S., Hafeez, A., Javed, F., & Rehman, F. (2022). An Overview of Hydrogen Production: Current Status, Potential, and Challenges. Fuel, 123317.
8. Usman, M. (2022). Hydrogen storage methods: Review and current status. Renewable and Sustainable Energy Reviews, 112743.
9. Rathi, B., Agarwal, S., Kumar, M., & Jain, A. (2023). Handbook of Energy Materials. Singapore: Springer Nature Singapore.
10. Isselhorst, A. (1995). Heat and mass transfer in coupled hydride reaction beds. Journal of Alloys and Compounds, 231(1-2), 871-879.
11. Boukhari, A., & Bessaïh, R. (2015). Numerical heat and mass transfer investigation of hydrogen absorption in an annulus-disc reactor. International Journal of Hydrogen Energy, 40(39), 13708-13717.

12. Jemni, A., & Ben Nasrallah, S. (1995). Study of two-dimensional heat and mass transfer during absorption in a metal-hydrogen reactor. International Journal of Hydrogen Energy, 20(1), 43-52.
13. Jemni, A., Ben Nasrallah, S., & Lamloumi, J. (1999). Experimental and theoretical study of ametal–hydrogen reactor. Journal international de l'énergie hydrogène, 24(7), 631-644.
14. Chalet, D., Lesage, M., Cormerais, M., & Marimbordes, T. (2017). Nodal modelling for advanced thermal-management of internal combustion engine. Applied Energy, 190, 99-113.
15. Chabane, D., Harel, F., Djerdir, A., Ibrahim, M., Candusso, D., Elkedim, O., & Feninèche, N. (2017). Influence of the key parameters on the dynamic behavior of the hydrogen absorption by LaNi5. International Journal of Hydrogen Energy, 42(2), 1412-1419.
16. Chaise, A., De Rango, P., Marty, P., & Fruchart, D. (2010). Experimental and numerical study of a magnesium hydride tank. International Journal of Hydrogen Energy, 35(12), 6311-6322.
17. Chandra, S., Sharma, P., Muthukumar, P., & Tatiparti, S. (2020). Modeling and numerical simulation of a 5 kg LaNi5-based hydrogen storage reactor with internal conical fins. International Journal of Hydrogen Energy, 45(15), 8794-8809.
18. Askri, F., Ben Salah, M., & Ben Nasrallah, S. (2009). Heat and mass transfer studies on metal-hydrogen reactor filled with MmNi4.6Fe0.4. International Journal of Hydrogen Energy, 34(16), 6705-6711.
19. Kumar Phate, A., Prakash Maiya, M., & Srinivasa Murthy, S. (2007). Simulation of transient heat and mass transfer during hydrogen sorption in cylindrical metal hydride beds. International Journal of Hydrogen Energy, 32(12), 1969-1981.
20. Ben Nasrallah, S., & Jemni, A. (1997). Heat and mass transfer models in metal-hydrogen reactor. International Journal of Hydrogen Energy, 22(1), 67-76.
21. Sandrock, G., & Thomas , G. (2001). The IEA/DOE/SNL on-line hydride databases. Applied Physics, 72, 153–155.
22. Chabane, D. (2017). Gestion énergétique d'un ensemble réservoir d'hydrogène à hydrure et une pile à combustible PEM. Université de technologie de Belfort-Montbéliard .

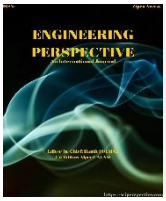

e-ISSN:2757-9077

ENGINEERING PERSPECTIVE

https://sciperspective.com/ Research Paper

Techno-Economic Analysis of a Natural Gas Dehydration System: A Case Study of an "X" Processing Plant in the Niger Delta

Musa Shittu[1*] and Aniefiok Livinus [1]

[1] *Department of Petroleum Engineering, University of Uyo, P.M.B 1017, Uyo, Akwa Ibom State, Nigeria.*

ABSTRACT

The presence of water in the natural gas stream could cause pipeline corrosion, limit pipeline flow capacities, pipeline blockages and possible damage to process filters, valves, and compressors. The absorption gas dehydration system with Triethylene Glycol (TEG) as an inhibitor is the most widely used and reliable gas dehydration system for non-cryogenic pipeline operation. TEG losses have been a serious concern to the operation personnel in "X" dehydration Plant in the Niger Delta region of Nigeria.

This study therefore presents the economic analyses of gas dehydration by the introduction of a stripping (sales) gas to the TEG regenerator-reboiler to enhance the vapor separation and scrub off any gaseous impurities that may still exist in the rich TEG. The existing dehydration units were modeled and process parameters were simulated using Aspen HYSYS® software. An instance from the simulation results shows that, for a TEG flow rate of 0.4543 m^3/h, 97% of TEG was recovered. However, with the introduction of a dry natural gas to the reboiler, 99.98% of the TEG was recovered. This significant improvement, which represents 10.2 kg/h of TEG recovery, translates to a cost saving of approximately $89,352 per year.

Keywords: Gas processing plants; Niger Delta; TEG Absorption units; Gas Dehydration

History
Received: 27.10.2023
Accepted: 12.03.2023

Author Contacts
**Corresponding Author*
e-mail addresses : musashittu@gmail.com

How to cite this paper: Shittu, M., Livinus, A. (2024). Techno-Economic Analysis of a Natural Gas Dehydration System: A Case Study Of an "X" Processing Plant in the Niger Delta. Engineering Perspective, 4(1),40-46. http://dx.doi.org/10.29228/eng.pers.73884

1. Introduction

Natural gas has residential and industrial uses. It is an energy source often used for heating, cooking, electricity generation and fuel for vehicles. Natural gas is also environmentally friendly. For instance, in electricity generation, natural gas burns cleaner than other fossil fuel such as oil and coal due to the fact that it produces less carbon-dioxide per unit energy released. For an equivalent amount of heat, natural gas produces about 30% less carbon dioxide than burning petroleum and about 45% less than burning coal [1].

Natural gases either from natural production or storage reservoirs contain water, which condense and form solid gas hydrates to block pipeline flow and especially control systems. Natural gas in transit to market should be dehydrated to a controlled water content to avoid hydrate as well as to minimize the corrosion problems. Natural gas processing consists of separating all of the various hydrocarbons and fluids from the pure natural gas [2].

Gas dehydration is one of the most prominent unit operations in natural gas processing facility where water is removed from the natural gas stream. The presence of water in the natural gas stream could cause pipeline corrosion, limit pipeline flow capacities, pipeline blockages and possible damage to process filters, valves, and compressors. This therefore can lead to increased maintenance cost and reduced line capacity [3]. As pointed out by Kidnay and Parish[4], to ensure smooth operation in downstream gas facilities: for example, gas pipeline usually requires 4-7 lb/MMSCF water content (87.2 - 152.6 ppm); for cryogenic unit (to produce Liquefied Natural Gas (LNG)), water content in gas shall be less than 1 ppm; for Compressed Natural Gas (CNG) plant, before entering compressor unit, water content shall be reduced to maximum 3 lb/MMSCF to meet product specification. Some of the methods of dehydration are as follows: direct cooling (refrigeration), adsorption, absorption, membrane processes [5].

The Absorption gas dehydration system with Triethylene Glycol (TEG) as the inhibitor is the most widely used and reliable gas dehydration system in upstream operations. With glycol absorption, it

is possible to lower the water contents down to approximately 10 ppmvol, depending on the purity of the lean glycol [6].

Glycol losses are the losses of some glycol content used during dehydration [7]. Glycol losses can occur due to uneven contracting or too high a water content in the glycol mixture composition. The frequent occurrence of glycol losses in the gas dehydration process makes the unit less efficient. The safe limit of glycol losses set by the industry must not exceed is 0.01 – 0.15 gal/mmscf [8].

Several researches on the simulation of TEG dehydration systems considering numerous scenarios have been conducted; for example, the works of Marfo *et al*. [9], Salman *et al*. [10], Kong, *et al*. [11], Anyadiegwu *et al.* [12], Okafor, *et al*. [13], Chidiebere *et al*. [14], Neagu and Cursaru [15].

This work therefore presents techno-economic analyses of the impact of introducing a dry natural gas into regenerator reboiler to enhance the vapor separation to reduce TEG losses in "X" gas processing plant located in the Niger-Delta of Nigeria. Note that, TEG losses have been a concern to the operation personnels in "X" gas dehydration Plant, as 1.5 kg of TEG is lost per day. This translates to approximately 11 kg of TEG losses per week, which calls for action. The field covers an area of 365 x 250 gross m^2 and with a gas processing capacity of 125 MMSCFD. The "X" gas processing plant has three major functions: Process, monitor, control and deliver gases at the required specifications at Gas Transfer Point, recover condensate mixed with reservoir water and send to "X" Flow Station for treatment, and generate utilities like electricity and domestic water for others facilities.

Table 1. Operating conditions for the TEG dehydrating unit of "X" gas processing plant

Parameters	units	Value
Molar Flow	MMSCF/D	10.01
Mass Flow	kg/hr	9463
Pressure	bar	66.67
Temperature	^{0}C	30
Liquid Volume	Barrels/D	4317
Composition	CH_4-CH_{6+}, N_2, H_2O	See Table 2
Lean Glycol (TEG)	TEG	-
Lean TEG purity	wt%	≥ 99.5%
Lean TEG temperature	°C	50
Lean TEG pressure	bara	52.05
Contactor pressure	bara	66.07
Contactor gas temperature	°C	30
Glycol Temperature	°C	29.10

2. Data gathering, process description and methodology

2.1 Data description

Oil and gas field in the Niger-Delta in recent years have high water cut in the excesses of 22% [16]. The dataset used for developing the simulation for this study was obtained from the field operating manuals (describing the facilities - location, description, process data, reference documents, e.t.c) of "X" processing plant in the Niger-Delta region of Nigeria. The field covers an area of 365 x 250 gross m^2 and with a gas processing capacity of 125 MMSCFD. Table 1 and 2 show summaries of the operating conditions of the dehydration unit and the feed gas composition of the "X" Processing Plant.

Table 2. Feed Gas Composition

Component	Formulae	Mole Fraction
Methane	CH_4	0.8785
Ethane	C_2H_4	0.0602
Propane	C_3H_6	0.0256
i-butane	i-C_4H_8	0.0065
n-butane	n-C_4H_8	0.0078
i-pentane	i-C_5H_{10}	0.0026
n-pentane	n-C_5H_{10}	0.0019
C^{6+}		0.0018
Water	H_20	0.008
Nitrogen	N_2	0.0002
Carbon-dioxide	CO_2	0.0141
Total		1.000

2.2 Process description and methodology

Figure 1 shows the modelled, using an industrial software Aspen HYSYS [17], existing natural gas dehydration unit of "X" Processing plant located in the Niger-Delta region of Nigeria.

The feed gas was saturated with water through the feed gas saturator to achieve actual wet process conditions as shown in Table 1. The wet gas is sent to the absorber column (TEG contactor) where it's fed through the bottom at 30°C and 60.67 barg and the lean glycol is fed at 50°C and 62.02 barg at the top. As the glycol moves towards the bottom of the contactor, it comes into contact with and absorbs the water in the wet gas stream. The dry gas moves to the top of the contactor and leave the system for other processes.

Rich TEG, which has absorbed water from the gas stream, flows out of the dehydrator column at 28.44 °C and 62.05 barg, to the let-down valve (pressure control valve) where the pressure is reduced 1.790 barg before it enters the heat exchanger to avoid any safety concerns.

The glycol heat exchanger pre-heat the rich TEG to 106.0 °C and 1.16 barg before it enters the TEG regenerator. The glycol heat exchanger is a tubular heat exchanger using hot lean glycol from the stripping column as heating medium (shell side). Rich glycol (tube side), enters the heat exchanger at 34.6 °C and leaves the glycol/glycol heat exchanger at 106.0 °C.

The glycol regeneration section consists of the main steel column, an overhead condenser, and a reboiler whose function is to regenerate the glycol to a high purity so that it can be recirculated to the absorber to continue its dehydration function. In the reboiler, the rich glycol is heated 198.9°C to near its boiling point enabling it to release virtually all of the absorbed water and any other compounds. The main steel column is packed with random packing to ensure good contact between vapor and liquid phases. The generated vapours pass up the rich glycol steel column along with any volatile material and are contacted with liquid traveling down the column.

The glycol is sent to the surge drum, the glycol surge drum provides a buffer volume for circulating glycol. The lean glycol is cooled again with a trim cooler before being fed back into the absorber. The condenser cools the vapor leaving the main steel column and condenses any glycol vapours to liquid. The water remains as vapours and exits the column at the top.

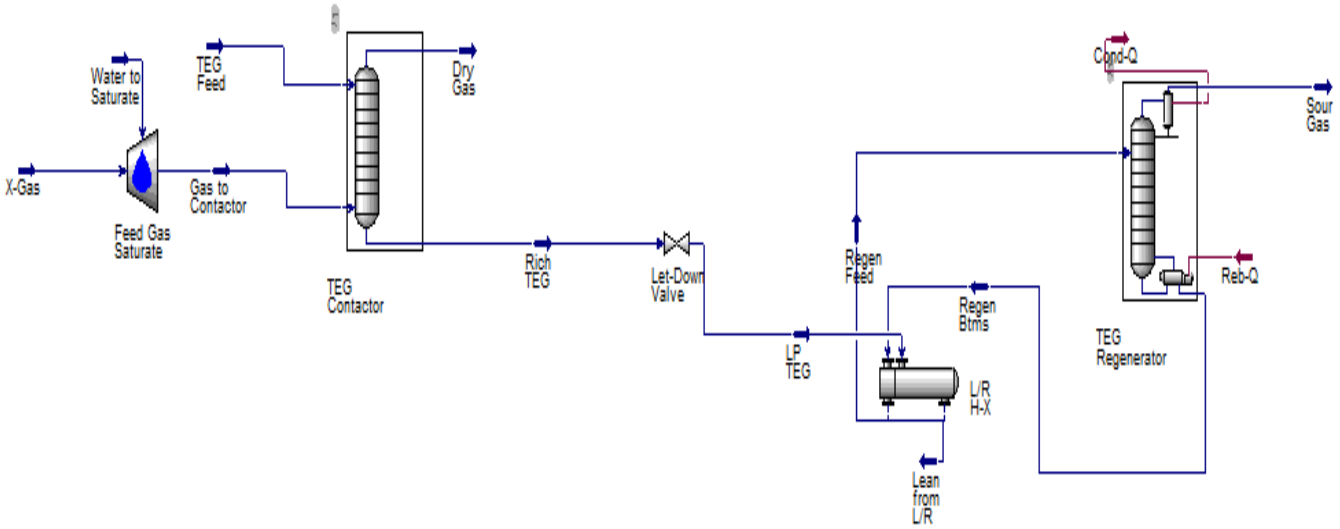

Figure 1. Model of the existing TEG dehydration unit of the "X" gas processing plant.

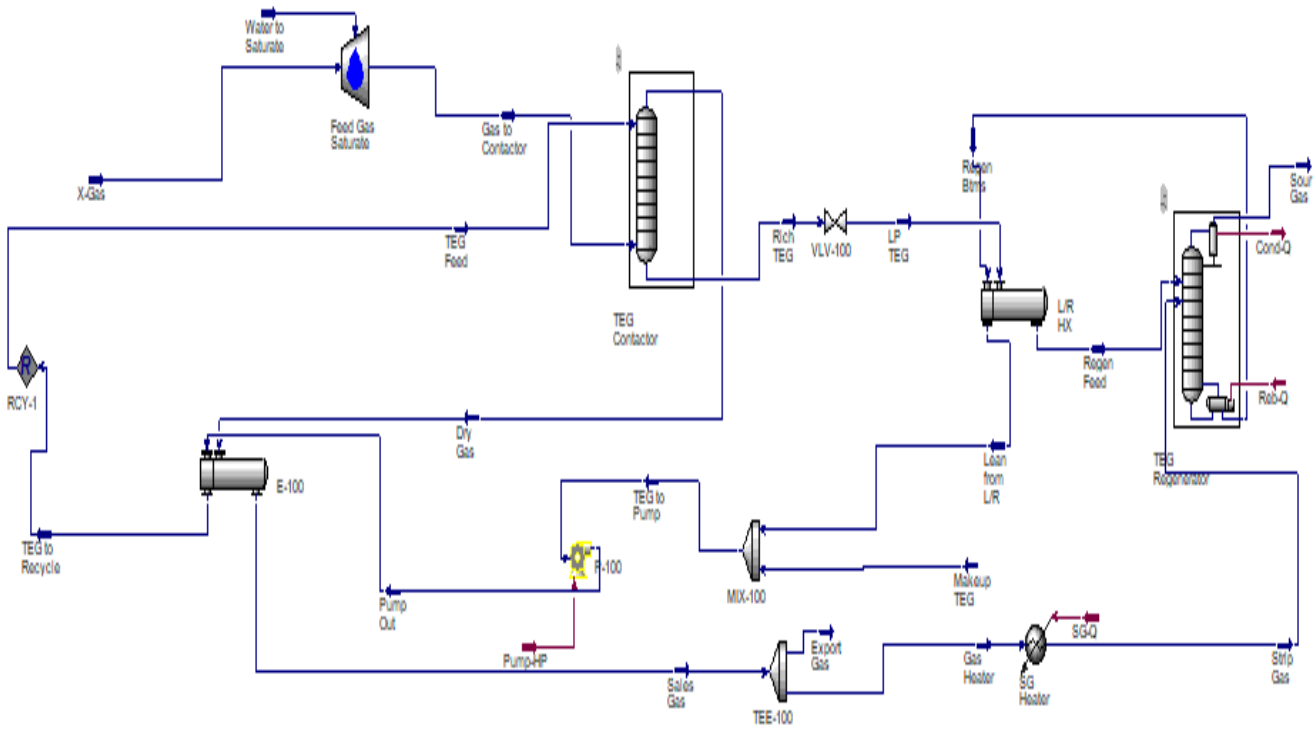

Figure 2. Modified TEG dehydration unit of "X" gas processing plant.

2.2.1 Process modification and analyses

To enhance the performance and maximize the potential benefits of the dehydration unit, the existing (base) model was modified by the introduction of a stripping gas to the TEG regenerator reboiler to enhance the vapor separation and scrub off any gaseous impurities that may still exist in the rich TEG. Figure 2 shows the modified process flow model of the natural gas dehydration unit.

The TEG recovery of both the base and the modified models were then analyzed by comparing the TEG recovery rates. Peter *et al.* [18] maintained that sensitivity analysis can help researchers prioritize research needs and to better understand the tradeoffs associated with achieving higher system efficiencies by increasing operating temperatures or by increasing specific component efficiencies. The effects of some input variables; the feed gas flow rates, TEG flow rates and dry gas flow rates, on the output variable; TEG recovery weight, were therefore analyzed.

2.3 Economic analysis

Natural gas processing facilities are capital projects and would require large commitment of funds. Its impact on the financial wellbeing of an organization extends over a long period. It is therefore necessary that operation and maintenance cost of the dehydration unit does not exceed its value [19]. In this work, break-even analysis (BEA) and the annual cost savings from the glycol recovery to determine the time (years) when the investment decision to modified the process of the dehydration unit of "X" processing plant becomes viable was used.

The costing of the dehydration unit of "X" processing plant considered was primarily the equipment cost, operating cost and installation cost used for the modification of the dehydration unit. The equipment cost comprises: valves, piping, process and instrumentation equipment used for the upgrade of the unit. The prices were verified from Croft Production Systems, a leading company involved in the designing, building and maintenance of dehydration units and oil gas equipment. The installation and operating cost estimates were collected from the Site Manager of "X" processing plant. See Table 3 for the costing summary.

Table 3. Cost summary for the dehydration unit

Cost Item	Amount ($)
Equipment Cost	600,000
Installation Cost	50,000
Operating Cost	10,000
Total	660,000

The economics of the amount of TEG that was recovered yearly from the simulation model of the existing dehydration unit was then compared with the modified model, using Eq. (1) and Eq. (2).

$$SCost = (Vol.\ \ RRTEGwStrippingGas\ x\ CostTEG) - (Vol.RRTEGwoStrippingGas\ x\ CostTEG) \quad (1)$$

$$AScost = 365\ x\ SCost\ for\ mass\ flow\ rate \quad (2)$$

3. Results and discussion

3.1 Technical analysis

The simulation results were based on the following variables; hydrate formation temperature, hydrocarbon dew points, water content, TEG losses and TEG recovery.

The dependent parameters/variables i.e. the water content, dew point and hydrate formation temperature of the saturated and dry gas are presented in Table 4. The effectiveness of the model was validated by comparing the dependent parameters of the saturated inlet feed gas and dehydrated dry gas.

According to Marfo, *et al*. [9], the standard water content requirement for natural gas is 6- 7lb/mmscf. This criterion was also used to validate the effectiveness of the simulation model.

From the dependent parameters presented in Table 4, it can be seen that the water content of the gas was reduced from 39.52 Ib/MMSCF to 4.73 Ib/MMSCF. Based on the simulation results obtained, the composition mass fraction of TEG without stripping gas was 0.9891 compared to 0.9996 obtained when the dry gas was introduced.

Table 4. Results of both the saturated and dry gas of the Model

Dependent variables	Saturated Gas	Dry Gas
Water content (lb/MMSCF)	39.52	4.73
Dew point temperature (^{0}C)	30.00	-66.47
Hydrate formation temperature (^{0}C)	17.4851	-48.6265

The Initial TEG flow rate from the design is 68.56 bbl/d, which translates to 0.4543m^3/h (2 gallons per minutes (GPM)). The density of the TEG is 1100kg/m^3. Therefore, applying Eq. (3), the mass flow rate of TEG is 499.7 kg/h.

$$e = m/v \quad (3)$$

where, e is the density of TEG, m denotes the Mass flow rate, v is the volumetric flow rate.

TEG recovery rate for the existing case= 0.9791 x 499.7 kg/h = 489.3 kg/h.

TEG recovery rate for the modified case= 0.9996 x 499.7 kg/h = 499.5 kg/h.

Therefore, the extent of the improvement in the amount of TEG recovery rate

= 499.5 - 489.3 kg/h = 10.2 kg/h.

The TEG recovery rate of 10.2 kg/h shows the significant improvement in the amount of TEG recovered by introducing a stripping gas to the TEG regenerator reboiler. The physiochemical properties (i.e. hydrate formation temperature, hydrocarbon dew points, water content) of the dry gas were also improved.

Some glycol negligible losses of 0.0004 mass in fraction still exist in the dehydration unit. Therefore, the actual TEG recovery rate for the existing simulation model = 0.0004 x 499.7 kg/h = 0.19988 kg/h = 4.797 kg/d = 1751 kg/Year.

3.1.1 Parametric analysis

This analysis examines the relative importance of the selected process feed (input) parameters to the determination of target (output) variable of TEG recovery. Different case studies were modelled. The summaries of the results are shown in Table 5 and Figure 3, for the effect of TEG rates on TEG recovery; Table 6 and Figure 4, for the effect of stripping gas volume on TEG recovery; Table 7 and Figure 5, for the effect of feed gas rates on TEG recovery.

Table 5. Effect of TEG rates on TEG Recovery

TEG Rate (m^3/h)	TEG Recovery (kg/h)
0.45	0.989070412
0.55	0.989079363
0.65	0.989088029
0.75	0.989088374
0.85	0.989091836
0.95	0.989096694

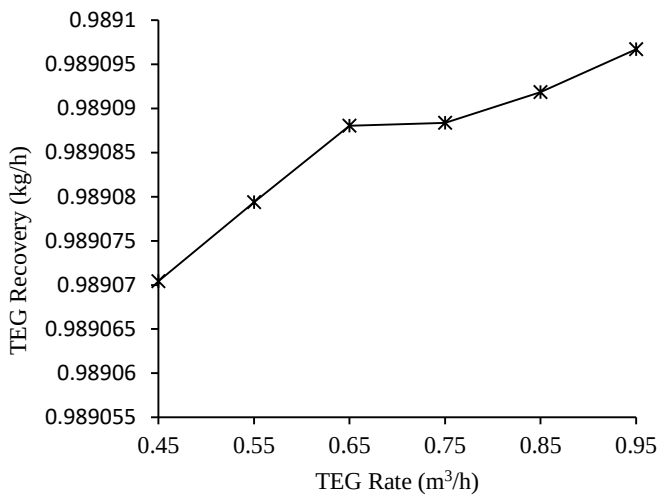

Figure 3. Plot of TEG rates and TEG recovery

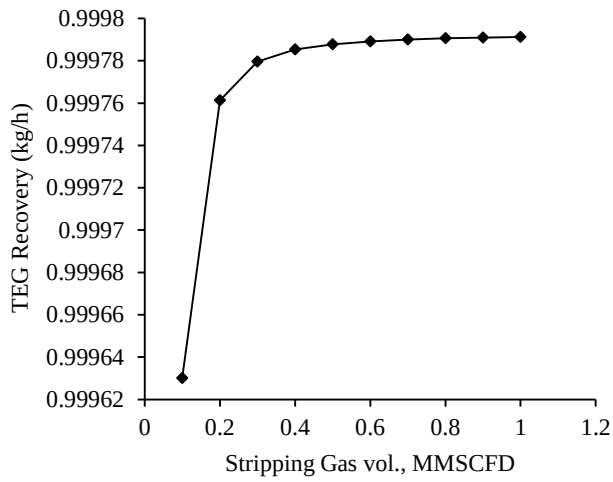

Figure 4. Plot of stripping gas volume and TEG recovery

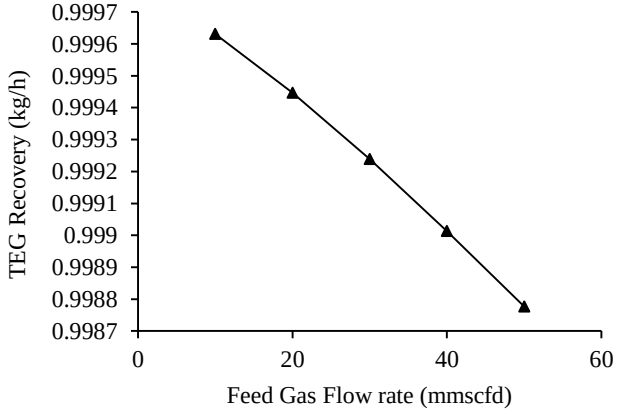

Figure 5. Plot of feed gas rates and TEG recovery

The results of sensitivity analyses indicate that there is a positive relationship between TEG rate and TEG recovery. There is a noticeable increase in the TEG recovery as the TEG rates is increased from 0.45 m^3/h to 0.65 m^3/h and from 0.75m^3/h to 0.95 m^3/h. However, there was a fairly constant TEG recovery between 0.65 m^3/h. and 0.75 m^3/h flow rate, as shown in Figure 3.

Table 6. Effect of stripping volume on TEG Recovery

Stripping Gas Vol. (MMSCFD)	TEG Recovery (kg/h)
0.1	0.999630046
0.2	0.999761265
0.3	0.999779633
0.4	0.999785328
0.5	0.99978785
0.6	0.99978921
0.7	0.999790038
0.8	0.999790586
0.9	0.999790972
1	0.999791256

Looking at the plot of stripping gas volume and TEG recovery in Figure 4, there is a steady increase in TEG recovery as the stripping gas volume is increased from 0.1 to 0.5 MMSCFD with a little or no further TEG recovery was achieved at stripping gas volume between 0.5 and 1 MMSCFD, see Figure 4.

Table 7. Effect of Feed gas rates on TEG Recovery

Feed Gas Rates (MMSCFD)	TEG Recovery (kg/h)
10	0.999631538
20	0.999446588
30	0.99923922
40	0.999013694
50	0.99877634

From the plot of Feed gas rate and TEG recovery in Figure 5, a negative relationship is observed. There is a sharp decrease in the TEG recovery as the feed gas rates is continuously increased between 10 MMSCFD and 50 MMSCFD.

3.2 Economic analysis

According to Adeogun and Iledare [20], various profitability measures have been developed to aid decision makers choose between several investment alternatives; these measures help rank a projects' profitability based on the profitability measures. The economic analysis of the dehydration unit of processing plant was therefore performed using the TEG recovery rate and the annual cost savings. Break-Even Analysis (BEA) was used to determine when viability of the investment decision. The primary concern of the management of "X" processing plant is to reduce the TEG losses and the yearly cost implications. The cost of 1kg of TEG at the international market of approximately $1 has been considered.

Therefore, the cost of TEG recovery rate (489.3 kg/h) of for the existing (base) case = $489.3/hr.

The cost of TEG recovery rate (499.5 kg/h) for the modified case = $499.5/h

Hence, the cost savings = $499.5/hr - $489.3/hr = $10.2/hr =

$244.8/d = $89,352/Y

Cost of glycol losses that still exist in the dehydration unit = 0.19988 kg/h = $0.19988/h = $4.797/d = $1751 /Y.

3.2.1 Break-even analysis

The Break-Even Analysis (BEA) was done by comparing the modification cost and the yearly cost savings from TEG glycol recovery of the improved dehydration unit to determine the break-even time (BET). The modification cost is a one-time capital investment, which is added to the yearly acceptable glycol losses that still exist in the gas dehydration unit, as represented in Table 8. The BET is the time (in years) where the savings from glycol recovery equals the modification cost. The investment decision to upgrade the dehydration unit of "X" processing plant becomes viable after the BET.

Table 8. Break-even analysis of modification cost and glycol cost savings

Break-Even Time(Y)	TEG Glycol Losses (in $)	Modification Cost (in $)	TEG Glycol Cost Savings (in $)
1	1,751	660,000	89,352
2	3,502	663,502	178,704
3	5,253	665,253	268,056
4	7,004	667,004	357,408
5	8,755	668,755	446,760
6	10,506	670,506	536,112
7	12,257	672,257	625,464
8	14,008	**674,008**	**714,816**
9	15,759	675,759	804,168
10	17,510	677,510	892,520

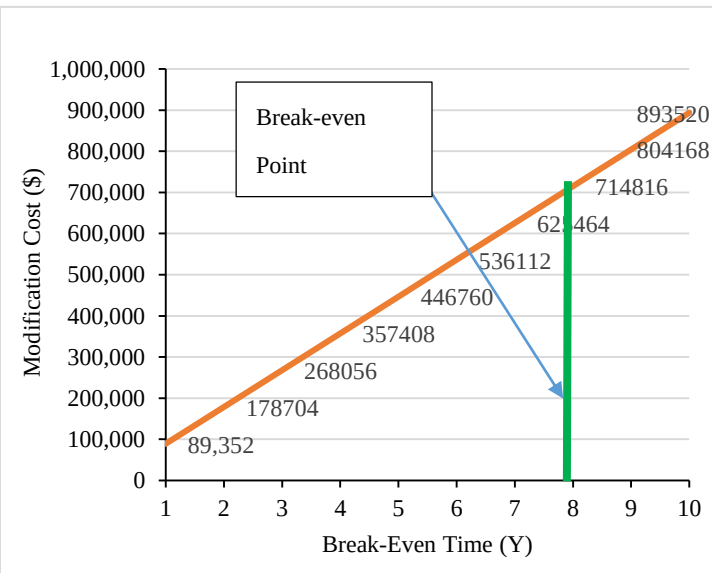

Figure 6. Plot of Modification cost and break-even time

From Figure 6, the break-even point (BEP) is after year 8. This represents the point at which the yearly cost savings from glycol recovery equals the cost of upgrading the dehydration unit by the introduction of a dry gas to the TEG regenerator reboiler to enhance the vapor separation. Beyond the break-even point, the investment decision to upgrade the existing dehydration unit becomes a viable investment decision.

4. Conclusions

A techno-economic analyses of the impact of introducing a dry natural gas into regenerator reboiler to reduce TEG losses in the absorption system of "X" gas processing plant located in the Niger-Delta of Nigeria has been performed. Although, the modification of the existing dehydration unit is capital intensive, the investment decision to upgrade the existing gas dehydration unit becomes viable after the Break-Even Point (BEP). The following conclusion can be drawn from this research;

- the modified model of introducing a dry gas to the reboiler of TEG regenerator has improvement on the glycol recovery of the dehydration unit by 10.2 kg/h, which translate to a cost saving of approximately $89,352 per year.
- the target parameters of the modified model were all improved, and the water content value of 4.73 lb/MMSCFD of the dry gas is within the standard limit of 6-7 lb/MMSCFD for pipeline transport.
- TEG losses still exist in the gas dehydration unit but it is considered negligible.
- the sensitivity analysis of the stripping gas volume and the TEG recovery rate shows that there was a steady increase in TEG recovery as the stripping gas volume was increased from 0.1 to 0.5 MMSCFD and a constant TEG recovery was achieved at stripping gas volume between 0.5 and 1 MMSCFD.

Acknowledgment

Thanks to Allah Almighty for His mercies, blessings and provisions throughout this research work and to my beloved parents for the opportunity of experiencing this world. Special thanks to my wife, Dr. Hafsatu Idenebeme Isah and our lovely children. Finally, to the Department of Petroleum Engineering, University of Uyo and my wonderful friends, I appreciate your support and encouragement throughout this programme.

Nomenclature

e	TEG density (kg/m^3)
m	TEG mass flow rate (kg/h)
v	TEG volumetric flow rate (m^3/h)
$SCost$	Saved cost ($)
$AScost$	Annual saved cost ($)
TEG	Triethylene Glycol
BEP	Break-even point

Conflict of Interest Statement

The authors declare that there is no conflict of interest in the study.

CRediT Author Statement

Musa Shittu: Conceptualization, Data collection, Simulation, Writing-original draft, Writing-revised draft. **Aniefiok Livinus:** Supervision, Writing-revised draft, Editing.

References

1. Marques, M. R. (2014). Modelling the Natural Gas Sweetening and Dehydration Prior to Liquefaction, Masters Dissertation, Istituto Técnico, Lisbon, Portugal.
2. Ahmad Syahrul, M. (2009). Natural Gas Dehydration using Triethylene Glycol (TEG), Masters Dissertation, University of Malaysia Pahang, Malaysia.
3. Faramawy, S., Zaki, T., and Sakr, A. A. E. (2016). Natural gas origin, composition, and processing: A review. Journal of Natural Gas Science and Engineering, 34, 34–54. https://doi.org/10.1016/j.jngse.2016.06.030
4. Kidnay, A. J. and Parish, W. R. (2006). Fundamentals of natural gas processing, Baco Raton: Taylor & Francis Group, 2006.
5. Siti S. B. M. R. (2009). Natural gas dehydration using silica gel: fabrication of dehydration unit. Masters Dissertation, Universiti Malaysia Pahang, Malaysia.
6. Guo, B. G. (2005). Natural gas engineering handbook. 1st Edition, Gulf Publishing Company, Houston, Texas, USA.
7. Haque, M.E. (2012). Ethylene glycol regeneration plan: A systematic approach to troubleshoot the common problems. Journal of Chemical Engineering, 27, 21-26.
8. Indarti, A., Nugroho, N.K.A., Zaini, A.R. (2023). Glycol losses calculation in a gas dehydration unit. Gema Wiralodra, 14(2), 736-741 https://doi.org/10.31943/gw.v14i2.501
9. Marfo, S.A., Opoku A.P., Morkli, C. and Issah, S. (2020). Natural Gas Dehydration Process Simulation and Optimisation - A Case Study of Jubilee Field, Proceedings of 6th UMaT Biennial International Mining and Mineral Conference, Tarkwa, Ghana, 127-136.
10. Salman, M., Zhang, L., and Chen, J. (2020). A computational simulation study for technoeconomic comparison of conventional and stripping gas methods for natural gas dehydration. Chinese Journal of Chemical Engineering, 28(9), 2285–2293. https://doi.org/10.1016/j.cjche.2020.03.013
11. Kong, Z.Y., Ahmed, M., Liu, S., Sunarso, J., (2018). Revamping existing glycol technologies in natural gas dehydration to improve the purity and absorption efficiency: Available methods and recent developments. Journal of Natural Science and Engineering, 56: 486-503. https://doi.org/10.1016/j.jngse.2018.06.008
12. Anyadiegwu, C. I. C., Kerunwa, A. and Oviawele, P. (2014). Natural Gas Dehydration using Triethylene Glycol (TEG), Petroleum & Coal, 56(4), 407-417.
13. Okafor, E., and Evwierhurhoma, A. O. (2020). Improving the performance of a natural gas 54 dehydration plantusing a combination of solvents. 44–54. https://doi.org/10.9790/1813- 0903014454
14. Chidiebere, O.O., Inyang, U.E. and Oboh.I.O (2023). Modelling and Optimization of Natural Gas Dehydration System using TEG Glycol. Journal of Engineering Research and Reports. 24(12), 89-102. https://doi.org/10.9734/jerr/2023/v24i12862
15. Neagu, M. and Cursaru, D. L. (2017). Technical and economic evaluations of the Triethylene glycol regeneration process-es in natural gas dehydration plants. Journal of Natural Gas Science and Engineering, 27(1), 327-340. https://doi.org/10.1016/j.jngse.2016.11.052
16. Appah, D. and Nwachukwu, F. O. (1998). Rapid method for dehydrating crude oil. Journal of Natural Science, 16, 14-23.
17. Csendes, V. F., Egedy, A., Leveneur, S., & Kummer, A. (2023). Application of Multi-Software Engineering: A Review and a Kinetic Parameter Identification Case Study. Processes, 11(5), 1503. https://doi.org/10.3390/pr11051503
18. Peter H. K., Thomas E. D., Alexander 'Sasha' O., Erik K. W., Scott M. Paap and Steven W. (2020). Techno-Economic Analysis: Best Practices and Assessment Tools. Sandia National Labouratories. 13473. https://doi.org/10.2172/1738878
19. Awotiku, I., (2011). Quantification of Risks and Uncertainty for developing Marginal Fields in the Niger Delta. Masters Dissertation, African University of Technology, Abuja, Nigeria
20. Adeogun, O. and Iledare, O. (2015). Developing a Framework for Maximising Marginal Oil and Gas Field Economics. Paper SPE-178347-MS presented at the SPE Nigeria Annual International Conference and Exhibition, Lagos, Nigeria, August.